KTH ROYAL INSTITUTE
OF TECHNOLOGY

Degree Project in Electrical Engineering

Second Cycle, 30 credits

Potential of interference to global-navigation systems from power-line discharges.

A study based on laboratory measurements and plasma simulation.

JOHAN ERIK MAGNI BJÖRKLUND

Stockholm, Sweden, 2024

Potential of interference to global-navigation systems from power-line discharges.

A study based on laboratory measurements and plasma simulation.

JOHAN ERIK MAGNI BJÖRKLUND

Date: October 20, 2024

Supervisors: Hans Edin, Torsten Augustsson
Examiner: Nathaniel Taylor
School of Electrical Engineering and Computer Science, KTH
Host company: Svenska kraftnät
Swedish title: Möjligheten för störningar av globala navigationssystem från kraftledningsurladdningar.
Swedish subtitle: En studie baserad på laborationsmätningar och plasmasimuleringar.

Potential of interference to global-navigation systems from power-line discharges.

A study based on laboratory measurements and plasma simulation.

JOHAN ERIK MAGNI BJÖRKLUND

Author's address: Johan Erik Magni Björklund, erbjorkl@kth.se, KTH Royal Institute of Technology, School of Electrical Engineering and Computer Science, Stockholm, Sweden, SE 100 44.

Document date: October 20, 2024

Swedish title: Möjligheten för störningar av globala navigationssystem från kraftledningsurladdningar.

Swedish subtitle: En studie baserad på laborationsmätningar och plasmasimuleringar.

ABSTRACT

Repeated reports of power lines or power-line equipment interfering with GPS and telecommunications devices require the phenomenon to be investigated further. In this thesis, interferences from a spark are investigated through charge and plasma simulations carried out in COMSOL and with laboratory measurements of electric field levels and signal-to-noise measurements. The charge simulations started with a capacitive model. Then charges were introduced and allowed to accelerate between the two plates. A Fourier spectrum of the radiated electric field from the charges was solved. This was performed to see the effects different geometries will have on an interference source. For the second simulation part of the project, the capacitive and a model of an insulator bell were simulated. The two models were surrounded by a medium meant to represent nitrogen gas, which was allowed to ionize. From these models, a frequency spectrum was calculated. For the final part of the thesis, two lab tests were performed: an SNR measurement of GNSS signals and spectral analysis of the radiation from a spark in the 800 MHz to 6GHz region. The goal of the SNR test was to record the SNR of different GPS signals with and without an interfering spark and compare the difference between the two to see if the spark interfered significantly with the signals. The goal of the spectral analysis measurement was to determine if the spark radiates interferences in the frequency ranges that GPS utilizes. From the charge simulations, the local peak electric field levels during the DC simulation were higher than the AC counterpart. The bandwidth of the local peaks of DC was smaller than its respective AC simulations. The local peaks were shifted upwards or downwards in the frequency spectra when the number of charges increased or decreased respectively. The last phenomenon observed was that the peaks were higher when the gap was shortened than if the gap was wider with increased voltage to achieve the same electric field levels. During the plasma simulations, a small peak in the electric field levels was observed in the ranges of 40-80 MHz, with decaying levels above and below these frequency thresholds. This peak was present in both models simulated but had a higher magnitude in the insulator bell model compared to the capacitor model. During the lab SNR measurements, a small decrease was observed in SNR between the background levels and the levels with the interfering spark present. During the spectral analysis measurements, the highest difference at the frequencies GPS operates at was 15-25 dB between background levels when a spark was present between two insulator bells.

Potential of interference to global-navigation systems from power-line discharges.

SAMMANFATTNING

Återkommande rapporteringar av kraftledningar eller kraftledningsutrutsning som stör GPS eller mobiltelefoni kräver att detta fenomen undersökts vidare. I denna avhandling undersöktes störningar från en gnista, detta gjordes genom laddning och plasma simuleringar i COMSOL samt laborationsmätningar av elektriska fältnivåer samt signal till brus mätningar av inkommande GPS signaler. Laddningssimuleringarna utfördes på en kondensatormodell, till denna modell introducerades laddningar som accelererades. Från laddningarna beräknades elektriska fältnivåerna och utifrån dessa beräknades en fouriertransform. Detta utfördes för att se olika geometriers påverkan en störningskälla. Sedan utfördes plasma simuleringar av kondensatormodellen samt en modell av en isolatorklocka. Dessa två modeller antogs vara omgivna av ett medium som ska representera kvävgas, denna gas kunde joniseras. Utifrån dessa modeller så beräknades ett fourierspektra av det elektriska fältet. För laborationsdelen av avhandlingen så utfördes två mätningar: elektriska fält mätningar samt SNR mätningar av GPS signaler, båda med en störande gnista. Målet med SNR mätningarna att observera skillnaden mellan SNR nivåerna med och utan en störande gnista. Målet med spektrum analysen var att undersöka ifall gnistan utstrålar störningar i frekvensområdena som GPS använder. Från laddningssimuleringarna, observerades lokala toppar som var högre i fallet av likspänning till skilland från växelspänning, dessa lokala toppar var hade mindre bandbredd i fallet av likspänning jämfört med topparna vid växelspänning. De lokala topparna skiftades uppåt eller neråt i frekvensspektrat då fler respektive färre laddningar introducerades till modellen. Högre toppnivåer observerades också när avståndet mellan plattorna var kortare jämfört med längre avstånd med samma fältnivåer. Från plasmasimuleringarna så obserseverades en topp i 40-80 MHz området, med avtagande nivåer på vardera sida av frekvensbandet. Denna top var närvarande i båda modellerna, men var större i modellen med isolatorklockan jämfört med kondensatormodellen. Vid labbmätningarna av SNR så observerades en liten minskning i SNR vid mätning då gnistan var närvarande jämfört med bakgrundsnivåerna. Vid spektrumanalys av en gnista mellan två isolatorklockor så observerades en ökning av 15-25 dB i bandbredderna som GPS använder jämfört med bakgrundsnivåerna.

Keywords: EMC, Electromagnetic Interferences, Charges, Discharges, Power Lines, Insulator bells, GPS, Drone, Radiation.

Nyckelord: EMC, Electromagnetiska Störningar, Laddningar, Urladdningar, Kraftledningar, Isolatorklockor GPS, Drönare, Utstrålning.

ACKNOWLEGEMENTS

I would personally like to give a deep thanks to Nathaniel Taylor for acting as my examiner and providing very valuable help and guidance during the project, and an even deeper thanks to Torsten Augustsson for being my supervisor on the side of SvK, thanks for supporting me throughout the project even though it took longer than expected, thanks for all the knowledge shared as well as helpful thoughts and ideas. I would also like to thank Hans Edin for providing me with the opportunity to perform the work carried out in this thesis and helping me and providing good insights during the project. Lastly i would like to thank all the people I have met throughout the project, both supporting me in terms of knowledge, ideas, and most of all, experience, friendship, and last but not least, laughs.

GLOSSARY

AC Alternating Current. 7, 8, 10, 32, 33, 47–50, 55, 58, 73, 78, 79
ARRL Association For Amateur Radio. 17

COTS Commercial of the shelf. 18
CWI Continuous wave interference. 57

DC Direct Current. 7, 9, 10, 30, 32, 47, 55, 58, 73–77

EM Electromagnetic. 26, 29, 30
EMC Electromagnetic Compatibility. 13, 20
EMI Electromagnetic Interference. 13, 16, 17, 20
ESD Electrostatic Discharges. 20

FFT Fast Fourier Transform. 30, 47–50, 58

GA Ground Antenna. 16
GNSS Global Navigation Satellite System. 13, 16, 18, 35, 37, 51, 54, 56–59
GPS Global Positioning System. 13–18, 20, 26, 56

IEMI Intentional Electromagnetic Interference. 21

MCS Master Control Station. 16
MS Monitoring Station. 16

RFI Radio Frequency Interference. 17
RTVI Radio Television Interference. 17

SNR Signal to Noise Ratio. 8, 14, 35, 37, 38, 51, 52, 56–59

TVI Television Interference. 17

Contents

List of Figures

List of Tables

1 INTRODUCTION

In this chapter, the background to the project, the original problems and definitions needed for the problem, descriptions, the purpose of the project, the goals of the project, delimitations made before and during the project work, and lastly, the structure of the report is covered in this section.

1.1 Background

In electrical systems, whether large-scale power transmission or small-scale integrated circuits, the importance of electromagnetic compatibility (EMC) cannot be understated. The EMC term covers different areas regarding electronics. In the context of this paper, the EMC term will be considered in the context of making sure that a device in question does not emit unnecessarily high levels of electromagnetic interferences that could reduce the functionality or disable itself or parts of its subsystems. The EMC term also covers a device's electromagnetic emission levels that could interfere with or disable other devices in the vicinity of the unit in question. Another part of EMC is interference prevention, since electromagnetic interferences (EMI) at different levels are present everywhere, the design of a device is important to achieve a certain level of immunity to electromagnetic interferences present in the environment or radiated from surrounding devices. This property would be known as the electronic device's susceptibility or immunity.

The emitted radiation levels and immunity of a device are important aspects throughout the designing process of any electronic device. If proper care is taken during the early design stages to reduce a device's emitted EMI and ensure that the device in question retains an acceptable level of immunity. This in turn will significantly reduce the cost as well as time invested if the final product is not EMC compliant due to high emissions or high susceptibility to incoming EMI. If little or no care for EMC were taken, this would most likely result in high electromagnetic emissions from the device while the unit's immunity will likely be low.

For the device to be sold within any modern day market, the device have to be EMC compliant. If a device is not compliant, a redesign to parts or the entirety of the device would be required. This redesigning process will most likely require more work, and thus a higher cost compared to if proper care to EMC was taken during the early and middle parts of the designing process when modifications and redesigns are easier to perform.

A device with low susceptibility, or high immunity to EMI will reduce the number of units that would be returned due to a user experiencing malfunction of the unit when it is exposed to a more noisy environment in terms of electric or magnetic fields. Proper planning in terms of components having the desired characteristics for the usage the component is to be used in, device layout and possibly shielding. If these precautions are made during the early design stages, when component selection, component placements, or other design choices to be included within a product are easily made, both time and money can be saved.

Even though a particular device is working correctly, and has low enough susceptibility so that the environment is not interfering with the device significantly, the signals a wireless device are sending or receiving might be interrupted if the signal is low-powered. One example of this are GNSS devices, these devices are receiving signals from satellites passing above, and due to the long distance between the two, when a signal reaches the device it will be low-powered. When GPS signals are low-powered and there is a source of EMI radiating in the bandwidths of GPS, there is a possibility that the receiver might misinterpret the sent signal, or it might be uninterpretable due to being drowned out by a higher powered interference source. This could result in a loss of precision, or it could render the device non-functional due to the increased noise levels. This results in the GPS device being unable to determine its position. All of these presented scenarios are reasons why good EMC practices are of great importance when designing a device.

1.2 Original purpose and definitions

The purpose of this MSc thesis is to determine if the spectral emissions of a spark can hurt the functionality of GPS devices. This will be investigated by observing the effects different gap geometries might have on the radiated electric field frequency spectrum. The results of this study will be used to demonstrate the importance of proper connection and tightening of power grid devices, mainly devices that could result in generation of a spark if it is not tightened properly.

1.3 Aim

The purposes described under section 1.2 will reached by first performing calculations of the radiated fields from accelerating charges inside a simpler geometry, This will be done to establish a baseline that can be used to verify models that will be simulated in later parts of the project.

The second goal of this project is to create a charge simulation within COMSOL that is similar to the calculated model to verify that the simulated model reaches a similar result to that of the calculated model.

If the results of the simulated models are similar to that of the calculated models, geometry, voltage, and changes of other parameters will be made to the simulated model to observe the effects the parameter changes may have on the characteristics of an interference source.

The third goal of this MSc thesis is to set up a plasma model. This model is assumed to result in electric field levels and frequency spectra that are closer to that if air were to be ionized due to a voltage drop across power line equipment.

To determine the spectral emissions of a spark and its effect on GPS signals, the thesis concludes with laboratory measurements. The laboratory measurements will cover radiated electric field measurements from an open spark to observe if the radiated emissions occupy the frequency ranges reserved for GPS signals. The laboratory test will also cover SNR measurements through a GPS signal analysis phone application. This testing will be carried out to observe if the emissions from a spark are of a magnitude which could interfere with a GPS device in a major way.

1.4 Delimitations

In this section, the delimitations made during the project will be covered

1.4.1 Project. In this thesis, due to time limitations, and coverage of more geometries would increase the time to complete the project and thus be outside the timeline of this work. For this project, two models will be covered: the first is a capacitive model, while the other is an improvised model of an insulator bell.

The capacitive model will consist of two parallel disks. This model is used to reduce the complexity of the fields surrounding the geometry. In the calculations performed at the start of this project, a homogeneous field was assumed. These assumptions will result in the fringing effects close to the edges of the disks being neglected during the calculations. This will reduce the complexity of computing the movement of the charges due to the forces the charges will be experiencing when exposed to the electric field between the plates.

During the calculations, since the charges are assumed to be moving in a perfect line, this resulted in the radiated magnetic field from one charge will not affect the other charges. This assumption is valid if the charges in the model are assumed to be point charges. This allows the effects of the magnetic fields from one charge upon the other charges to be excluded. The effects of the radiated electric fields from the charges will also be ignored. This is because the electric field from the two plates due to the applied voltage will have a significantly larger effect on the charges compared to the radiated electric fields from one charge upon another. The effects of the electric and magnetic fields radiated from one charge upon other charges will be considered during the COMSOL simulations performed during this project.

The second model considered for this project is an insulator bell. This model was made based on different cross-sectional figures of different insulator bells found on the internet. This is because blueprints and more exact dimensions

of a specific insulator bell design are company-owned property and are not available to the public. This model will be surrounded by nitrogen gas, which can undergo plasma reactions. The reason for using nitrogen is that the air in the atmosphere consists mostly of nitrogen.

1.4.2 Practical. One delimitation that was made during the simulation parts of the project and affected all models made during this project, was related to the base frequency. When simulations within COMSOL started, the plan was to have a base frequency of 50 Hz, which is the electrical frequency of the Swedish power grid. While using this base frequency for time-dependent studies and sampling at a rate to create a frequency spectrum up to a frequency of 2.5 GHz, to measure past the frequency bandwidths of GPS signals. This resulted in the simulations requiring more memory than available in the system. This resulted in constant computer crashes due to the computer memory running out. To reduce the file size and the computational time of each scenario, the base frequency used in all models was increased significantly, up to a frequency of 1 MHz. This reduced the amount of samples required to create a frequency spectrum up to a frequency past the bandwidths of GPS.

1.5 Structure of the report

In section 1.1, the background to the project is presented. In section 1.2, the original purpose and definitions used to specify the project will be covered. In section 1.3, the purpose of this paper is presented. In section 1.4, a more detailed description of why certain aspects of the project were not covered can be found. In section 2 a background to previous research can be found. In 3 the procedures for each stage of the project can be found, in section 3.1 the two main models of the project can be found, and in section 3.2 a description of the calculations performed can be found and delimitations made during these calculations can be seen. In section 3.3 how the model within COMSOL can be found, as well as a description of delimitations made during these simulations. In section 3.4 a description of the plasma model, its reactions, setup and delimitations of the simulations is presented. In section 4, the procedures followed during the two laboratory measurements, the test objects from which each measurement were taken are also presented. In section 5 the results of some calculations, simulations, and laboratory measurements are presented, while the remaining results can be found in the appendix. In section 6, a discussion regarding the observed results is conducted. In section 7, a summary of the project is conducted and in 8 possible future work based on the results acquired in this paper is presented.

2 THEORY

In this chapter, necessary background information related to the functioning of the global navigation satellite system (GNSS) to previous EMI tests and interference research related to power line equipment will be covered.

2.1 GNSS

Almost all GNSS satellites orbit the earth at heights of approximately 20,000 km, with the exception of IRNSS, which orbits at a height of 36,000 km. Orbiting at this altitude results in the satellite circling the Earth two times a day, or once a day for IRNSS [1][6][9].

For a GNSS receiver to be able to determine its location, the receiver has to know the location of the satellites orbiting above. In the case if GPS, This is done by having 16 monitoring stations (MS) on the ground, spread out around the world. The positioning of these stations are known very precisely. The signals sent by the satellites will be recorded by each MS receiving the signal. Since the speed of light is known, the distance between a MS and a satellite can be calculated by determining how long it took for the message to arrive at a particular MS. The time of transmission is included in the message sent by a satellite. The data received from all 16 monitoring stations are then sent to the master control station (MCS). The MS data is then used to precisely calculate the positioning and velocity of all satellites. This data makes up the ephemerides of a particular satellite. The data is also used to calculate clock errors. This is done for all 31 satellites making up the GPS constellation. This data is then inserted into an update message structure and then uploaded to each corresponding satellite by transmission through ground antennas (GA). Each satellite message is then re-transmitted from its respective satellite. This message is what a GPS receiver is picking up and uses to calculate its own position. [4]-[6]

In the case of GPS, the Ephemeris data is valid for about 4 hours but is usually updated every two hours. Less often updated is a table which contains information regarding health status, ephemerides for all GPS satellites in the system, ionospheric correction data time error corrections and more. This table is known as almanac. This table is updated at least once every 6-day period but is considered valid for 14 days. [8][32]

Since all GPS satellites are transmitting their signals in the same bandwiths, for each message to still be interpretable, the GNSS satellites are modulating their 50 bit/s signal on top of a pseudo-random noise. This pseudo-random noise is unique to each satellite. The noise modulated on top of each signal is considered to be Gold codes [7]. Meaning that they will strongly auto-correlate when very closely aligned to itself. This noise won't cross-correlate to the noise of other satellites in a significant way. With these characteristics in mind, this allows GPS satellites to send their messages within the same spectral range at the same time, with each signal sent from every satellite still being distinguishable from the signals of other satellites in view of the receiver [8][7].

The frequencies and bandwiths of other GNSS systems differs slightly from that of GPS, but are within the same general bandwith of 1.16-1.61 bandwiths [13].

2.2 Interference research

In "Use of Global Positioning System (GPS) receivers under power-line conductors" by J.M. Silva and R.G. Olsen [33], two causes were suggested to interfere with GPS signals in the presence of power lines. EMI coming from the power lines is greater or equal to the thermal noise of the environment, which they stated could lead to decreased performance, or electromagnetic scattering of the signal due to the overhead cables. This same scattering phenomenon could also be a result of towers or other surrounding objects, resulting in a decrease in received signal, and therefore decreased performance. They also stated that three conditions need to be satisfied for electromagnetic interference from transmission line corona to be a problem. Firstly, Silvia and Olsen stated that "The transmission line voltage is

above 230 kV", secondly, "The frequency of interest is less than 30 MHz", and finally, they stated that "The distance between the transmission line and the receiver is small (i.e., less than a few hundred feet)" [33][29]. With respect to signal frequency, GPS satellites are transmitting at a carrier frequency of 1227.6 MHz and 1575.42 MHz while newer satellites may also broadcast at a third carrier frequency of 1176 MHz [5]. Since all three of these carrier frequencies are far above the stated threshold for frequency, this reference implies that power line corona should not be a significant interfering factor of GPS signals. The GPS signals are transmitted from far away, the received signal is very low-powered. In this paper, J. M. Silva and R. G. Olsen performed GPS reception testings underneath two different 345 kV power lines, measuring the amplitude of the L1 carrier wave from different satellites visible to the GPS receiver, and later use this data to calculate C/N_0, the carrier wave to noise ratio, where N_0 is the noise which they assumed to be constant and purely internal to the device. From the resulting graphs, they concluded there was no change in the signal level received when going from a place far from to directly underneath the transmission line. From these results, they concluded that scattering phenomena from power line conductors did not have an apparent effect on the received carrier wave. They performed a test during humid, or rainy weather, when corona interferences are expected to be 15-25 dB higher compared to fair weather conditions. During the test, the number of satellites the GPS device was locked onto was monitored. They found that the GPS were constantly locked onto 8 of the nine visible satellites during the test, and from this concluded that corona did not constitute a problem during their test case. [33]

In most cases, the sources of either radio frequency interference (RFI) or television interference (TVI) originates from sparks related to distribution power lines, or corona discharges on transmission lines [11][38][19]. While the Association for amateur radio (ARRL) stated that corona is "rarely, if ever" the main source of radio television interference (RTVI). Most of the time, the interference source can be tracked to some worn or broken component, so that power line corona can be ruled out [11]. This might be due to the fact that radio and/or television carrier frequency are above that of the 30 MHz limit which [33] stated as the highest frequency corona discharges usually affect. During rainy weather, at 75 MHz, the tower EMI was stated to be about 6 dB higher than that of the conductors. These values seem to be quite similar to what has been observed at 1 MHz. [19]

In "Electromagnetic interference measurements at 900 MHz on 230-kV and 500-kV transmission lines" Chartier et al [19], stated that humid or rainy weather corona could be detected up to a frequency of about 200 MHz, above that frequency, the interference due to corona is explained to be at a low enough level that it falls below the internal noise level of commercial devices. They stated that "Sparking does occur in lines of 230 kV and above, causing EMI. However, on lines of these voltages, EMI is principally due to corona on the conductors and on the hardware of the towers". They also stated that the individual corona sources from the tower hardware will generally have a larger magnitude compared to the corona of the conductors [19].

In "Frequency Spectrum Analysis of Series Arc and Corona Discharges" [22], they analyzed the electromagnetic emissions coming from two different types of spark gaps and three different setup types of constructions with the intent to create corona discharges. From these tests, the corona discharge emission seemed to be decaying linearly in magnitude up to a frequency of about 1 GHz, which was very close to the background noise of the test setup. While the sparks were emitting interference with at a peak frequency of about 150 MHz, with a decaying magnitude trend with either an increasing or decreasing frequency [22].

A similar to that of "Frequency Spectrum Analysis of Series Arc and Corona Discharges"[22] was seen in "Radiation in the Optical and UHF Range Emitted by Partial Discharges" [26], where they observed about the same decaying trend for the radiation of corona discharges could be observed. With increasing frequencies, the magnitude of possible electromagnetic interference could be seen to decrease [26].

In "Electromagnetic Spectrum of the Corona Discharge and Their Fundamental Frequency" by Luis E, et al [27], electromagnetic interference from a corona discharge setup was investigated. The testing took place in a semi-anechoic

chamber. Before the test, the background chamber was inspected for interferences in the range from 4 to 950 MHz. This spectral range was measured using three different antennas, one loop antenna spanning from 0.3-30 MHz, a bi-conical antenna with a range of 30-300 MHz, and a hybrid bi-conical/log periodic antenna spanning from 300 to 1000 MHz. When the background field levels had been measured, the test was conducted by sending a pulse within a specified frequency range. The spectral range from the corona resulting from the sent pulse was measured. From the low frequency band, 0.3-30 MHz, significant spectral emission in the 8-9, 17-18 and 25 MHz ranges were observed. When testing a pule within the 300 MHz range, they observed peaks in the frequency range of 35, 55 and 65 MHz. One thing to note was that the testing didn't include the lower frequency ranges, so it's unclear if the frequency spectrum has shifted upward or if this range couldn't be recorded in the first test. In the last range, 300-1000 MHz did not find peaks of any significant frequency, they concluded that there are no spectral emissions of significant magnitude and that this would not pose problems for radio, in the frequency ranges that they were testing [27].

In "Analysis of Passive Interference on Radio Station from UHVDC Power Transmission Lines in Short-wave Frequency" [24], it was concluded that the interferences as a result of electromagnetic scattering from an external electromagnetic fields from an 800 kV tower, power line, and overhead ground would be about 1 dBμV/m for what they call short wave frequencies, which they said to be about 1-30 MHz. They also gave guidelines based on their testing on how far away the radio station was supposed to be distanced from a power line for a particular noise level from a power line to be achieved. If an electromagnetic noise level of 0.5 dB compared to if the power line was not present is desired, a distance of 1600 m was recommended, or if 1.0 or 1.5 dB are desired, a distance of 700 or 300 meters respectively is required [24].

When a receiving antenna for either RF or TV is in plain view of a spark from a distribution or transmission line origin, the interference can be seen to have significant interference when compared when a similar spark but the antenna is shielded by a knoll or hill. [38]

Reports have come in to SvK from farmers who state that they have observed malfunctions of their GNSS based navigation systems present in their farm equipment. In the reports, the farmers stated that the observed malfunctions were due to the transmission lines traversing their farmlands. In trying to confirm the reports, the signal strengths and the number of satellites a receiver was locked onto were measured at one of the farmlands the observed malfunctions were reported from. The tests conducted included passing the entire field and recording the number of GPS satellites in view of the receiver. The age of the correction signal was also measured. The age of the signal was observed to be normal throughout the test except at times when the equipment "locked up", they suspected that the "lock up" was software-related, but the cause of the "lock up" was stated as being hard to determine. With this in mind, they concluded that the transmission lines did not have a meaningful impact on the GPSs' ability to locate the device in question. What was also tested was if the towers were interfering. This was done by driving in close proximity to the towers on the field. They concluded that the towers didn't have any significant effect on the GPS tracking in this case but could be a possible source of shadowing of the GPS signals [21].

In "Investigating the Impact of High Voltage Power Lines on GPS Signal." [29], Rabah M and El-Hattab investigated whether or not transmission lines had an effect on GPS signal. This was done by placing their own two base stations for their GPS system underneath a power line highway while having a receiver on a separate location which was not underneath the power lines. They found that the errors in positioning when the receiver was static was about 1 cm both for horizontal and vertical. But when the GPS was in motion the vertical error could increase to about 5 cm [29].

In "Susceptibility of Civilian GPS Receivers to Electromagnetic Radiation" by D. Månsson et al [30], they tested the susceptibility of three commercial of the shelf (COTS) GPS devices available at the time (2008). The tests that these devices were exposed to were a low and medium-level narrow-band fields, high-level narrow-band fields (high-power microwave) as well as high-level ultra-wide-band fields. These field tests were conducted with three different

orientations of the tested devices. From the conducted test the following conclusions were drawn. To interfere with these specific devices, a much lower electric field intensity level compared to the mandated levels was enough to interfere with the device, tenths of volts per meter compared to 3 V/m according to the standard. For the high-level narrow band tests, they observed that the electric fields required to crash or permanently damage the device was significantly higher than the mandated levels. Lastly, the orientation of the device being tested greatly influenced the threshold levels of the electric fields required to interfere with the device [30].

When it comes to radiated field strengths, according to the inverse square law, if the fields have been measured. If nothing else is influencing these fields, and the measurement distance from the source is doubled, the field strengths measured will be reduced to a fourth of the measured value at the initial distance [39].

In "Electromagnetic Interference (EMI) Produced by High Voltage Transmission Lines" [28], Alameri Ban M looked at the electric and magnetic fields from a power line setup with all three phases in a horizontal plane, with a single neutral placed above the phases. Depending on the position underneath the power lines, the fields will amplify or act destructively towards each other [28], and when beyond the outermost phase, the electric and the magnetic fields will be reduced with respect to distance [28][39].

In "Study on Reradiation Interference Characteristics of Steel Towers in Transmission Lines" [23], L Huang et al investigated reradiation from transmission power line towers for a particular tower design with respect to different incident angles of a 100 MHz signal. For the tower design in question, they found out that the tower was reflecting the incoming wave at the highest magnitudes at incident angles of 35°, 45°, 55° and 90° with respect to the direction of the power lines. They also suspected that the towers would behave as vertically grounded rods, due to the assumption that the ground the towers were standing on and that the towers were made from a superconducting material. Another assumption was also made, that the holes in the tower were small compared to the tower's height, and short compared to the wavelength of the incoming wave. With this in mind, they suspected that the maximum reradiation would occur at a wavelength of $\lambda/4 = h$, where the wavelength λ is equal to four times the tower's height, in accordance to the half-wave antenna theory [23][35][2]. Firstly, they simulated with a 100 MHz incoming radio wave, the amount of reradiation with respect to different incoming angles to the direction of the power lines. For this particular tower design, it could be seen to have peak reradiation at a 45° angle, with smaller peaks at 7.5° and at 82.5°. Then, with a set of predetermined angles, they looked at the frequency response of the tower, where they found resonance peaks, with respect to both the applied frequencies. They also observed that reradiation was not changed significantly below 6.3 MHz, this results in an incoming wave with a wavelength that is equal to the tower's height ($\lambda = h$). In the later parts of the paper, they tested the effects of changing the tower height 2 m in either direction, which they said might happen during the construction of these towers. In these tests, they observed that the resonance frequency changed, with a smaller tower came a higher reradiation peak frequency, while higher towers had lower peak reradiation frequencies. To conclude their paper, the height at which the cross-arm of the tower was changed. In this test, it was observed that the amount of reradiation with respect to different frequencies would change when the height of the cross-arm was changed [23].

Another study of reradiation was performed by Tang et al, where a scaled-down model of a V1S type power line tower was made. This model was placed in an anechoic chamber and the reradiation of incoming vertically polarized waves with a frequency of 0.6 - 2 MHz was measured. The expected reradiation from the scaled-down model was also calculated based on the generalized resonance theory. It was observed that the measurements from the scaled-down model were similar to the calculated values based on the generalized resonance theory [36].

In the IEEE standard on "Prediction, Measurement, and analysis of AM Broadcast Reradiation by power lines", [2]. They stated that the electrical height of a particular tower design is usually about 15% higher than the actual height of the tower. This height difference is due to the the towers are considered top-loaded due to the cross-arms the tower

uses to hold the sky wires. They also stated that depending on what kind of material the pole/tower is made from the effective radius of the tower when it comes to radiation resistance, can be from 3 to 4 meters while the ground wire can have an effective radius which can go all the way down to 1 cm [2].

In "Computation Model of the Reradiation Interference Protecting Distance Between Radio Station and UHV Power Lines" by Tang B et al [17], they investigated the influence of an 800 kV HVDC tower and its associated power line pair connected to it. In their simulation, it was observed that the HVDC tower is used in the proximity of a radio station radiating a signal with a frequency of 16.7 MHz or below, the tower was observed to act as a poor antenna for higher frequency compared to lower-frequency signals [17].

In "Numerical computation of the reradiation from power lines at MF frequencies" by C. W. Trueman and S. J. Kubina [37], an investigation on the attenuation of an array of power lines on radio signals with respect to different incoming angles of radiowaves compared to the direction the power lines are propagation. The simulation was performed on two different setups. The first model is one with all power lines set up in a straight line. The second model has a 90-degree angle in the middle of the power line setup, this means that the first half of the towers are placed on one straight line while the second half of the towers are lined up on a second straight line perpendicular to the first power line segment. With this simulation, they observed significant attenuation in 40, 140 220 and 320 perpendicular to the angle of the power lines. In the levels of -10 dB compared to what is assumed if the power lines were not present. The attenuation of the second model had attenuation points but was not as significant as for the straight-line configuration. In this paper, they concluded that this could have an impact on the functionality of radio stations [37].

In "Transient electromagnetic interferences between a power line and a pipeline due to a lightning discharge: An EMTP-based approach" [14]. The induced voltage on a nearby gas pipeline with respect to three different lightning strike characteristics. In this paper, a couple of power lines with accompanying towers were simulated with different current characteristics, during these simulations, they observed that with higher resistance earthing, the induced voltage in the gas pipeline increased as well [14].

2.3 Drone and UAV interference

Besides the correct operation of GPS or other positioning systems to provide positioning to the drone, there are other questions about the correctly controlled operation of drones near power lines. A loss of control of drones due to lowered or total loss of function in the proximity of power lines has been reported. Skiver et al, mentioned in "Experimental Investigation of EMC Weaknesses in UAVs During Overhead Power Line Inspection" [34] that there are four different classification states when it comes to drone operation. First being "normal functionality", second being "temporary loss of function that recovers without intervention", third being temporary loss of function that requires intervention" and the fourth and final being "non-recoverable damage"[34]. In this paper, they recorded the number of data errors occurring in different data streams present in the drone when flying at different distances to a power line. The drone in question was a custom-built drone with commercial off-the-shelf parts. Vital parts of the drone had been shielded by different types of foil or conducting tapes. The foil and the conductive tape were applied to enhance the EMC capabilities of the drone. The goal was to divert electrostatic discharges (ESD) away from the vital electrical components of the drone. The drone was flown towards the power line and touched the line several times, while simultaneously recording the amount of bit errors the drone encountered during its flight. From this testing, they observed that the error rate of the drone's systems were experiencing was close to zero, measured at some unstated distances away from the power line. When the drone was close to or touching the power line, in the data stream most susceptible to either ESD or EMI from the lines, they observed an error rate of up to about 3%. They reported that this was nothing that they could experience during the flight of the drone, because the manoeuvrability of the drone was not impacted significantly, nor did the

drone perform any unwanted movements. During the peak of fault errors, the drone continued to be responsive to the inputs made on the controller [34].

In "Review of Intentional Electromagnetic Interference on UAV Sensor Modules and Experimental Study" by S. G. Kim, et al [25], tests were made of how different drone components are being affected by intentional electromagnetic interference (IEMI). The first test conducted was an electric field measurement of the PCB when it was exposed to electromagnetic waves in a certain frequency band. From these tests, they observed that the induced voltage levels in parts of the drone's systems were changed significantly due to the resonant frequency of the drone's circuitry. Later they exposed the drone's gyroscope and accelerometer to the resonant frequencies that could be observed in the PCB, during this test, they observed no change in the functionality of either the gyroscope or the accelerometer. From these tests, it was expected that there would be some kind of malfunction of these components. The lack of interference to these units was explained by the small size of the gyroscope and accelerometer and that insufficient coupling of the electric field was achieved for it to affect the components. They explained that even higher power interference with broadband characteristics would be needed [15]. For the last test done, they were exposing an analog and digital camera, that could be found on the drone setup, to a 1 mW laser. From these tests, they observed disturbances in the video, it was also observed that it was affecting the optical flow sensor. During the performed attacks, the drone was sending a compensation signal to compensate for the incorrectly sensed instability that was transmitted from the gyro and the optical flow sensor. This could result in malfunction and potentially crash of the drone if the interference is strong enough [25].

3 METHOD

In this chapter, the first section overviews the simulated models. The second section covers the steps taken to solve for the electric field levels radiated from an accelerating charge (in model 1). The third section covers the charge simulation procedures. The fourth section covers the necessary components of the plasma simulations.

3.1 Models

The first model used during the calculation stage of the project can be considered purely capacitive. This model was used to calculate the radiated electric field levels from accelerating charges introduced to the geometry. The dimensions of the simple capacitive geometry can be seen in Table 2.

Part	Variable	Dimension (cm)
Gap / Distance between the two plates	x_{gap}	10

Table 1: Dimensions of the reference geometry used for calculation.

The capacitive geometry considered for the calculations can be seen in Figure 2.

This model will be considered purely capacitive under the assumption that a total vacuum is occupying the space between the two plates. For this model, the electric field levels resulting from an applied voltage to one of the plates while keeping the other plate grounded, will be considered homogeneous between the plates and while being far away from the edges. This will allow the resulting fringing effects close to the edges of the plates shown in Figure 1 to be ignored during the manual calculations of the emitted electric interferences.

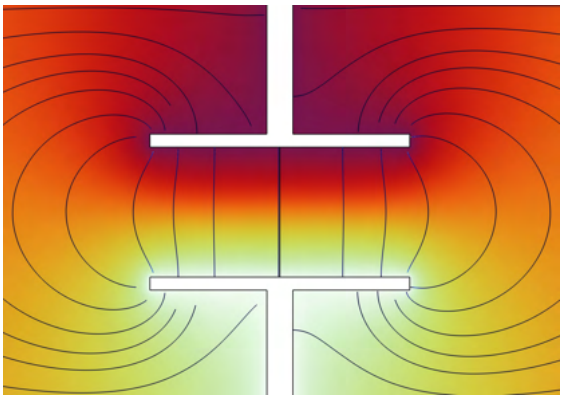

Figure 1: Close to the edges the fringing effects can be seen, while the electric fields are close to homogeneous in the middle of the plates.

With these assumptions, will result in less complex fields. With the assumption to ignore the fringing effects, the movement of the introduced particles between the plates can be reduced to acceleration, velocity and positioning along one axis, movement from the top plate towards the bottom plate or vice versa. These simplification will be helpful to establish a baseline for the characteristics of the radio-frequency interferences to be expected from a determinable interference source. It will also allow for some comparison between the calculated emissions and the simulated emissions of the later stages of the thesis.

A very similar model will be used for simulation within COMSOL. This model will be made up of two parallel discs, to get as close to a homogeneous electric field situation in the region between the discs, or when far away from the edges. Each disc will be held in place by one pin. This geometry is selected to keep the fields in between the two plates close to homogeneous, allowing for a fair comparison between the results of the simulated section to that of the calculated model that was considered during the manual calculation segment of the report. This Model can be seen in Figure 2.

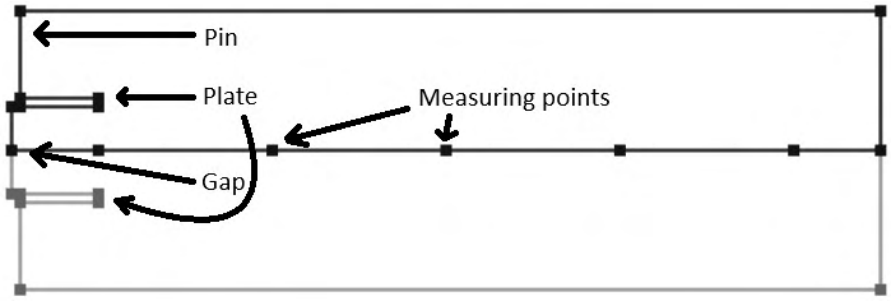

Figure 2: Picture of the simple geometry, this is made in 2 dimensions as well as the figure being axis symmetrical. In 3d, this will be two horizontal discs if the geometry is revolved around the left hand most axis line.

The dimensions used as a reference for the simple simulated geometry can be found in Table 2.

Part	Variable	Dimension (cm)
Gap height	x_{gap}	10
Plate thickness	x_{plate}	1
Pin height	x_{pin}	10
Plate radius	r_{plate}	10
Pin radius	r_{pin}	1
Box radius	r_{box}	100
Current stream radius	r_{steam}	1

Table 2: Dimensions of the simple geometry that was simulated within COMSOL

From Table (2), gap height is the distance between the two discs, plate thickness is the thickness of the top and bottom disc. Pin height represents the height of the part holding each one of the discs to the top and bottom of the geometry respectively. disc radius is the radius of the two plates, pin radius is the radius of the pin above and below the top and bottom disc respectively and box radius is the radius of the geometry surrounding the disc and pins.

For testing of different scenarios, one of the parameters will be changed at a time while the remaining ones will remain at reference values. This will be the case for all testing except if there is a special case scenario in which two or more variables might be changed at a time to keep another parameter the same. An example of this could be an increase in the applied voltage to one plate and increasing the distance between the plates to keep the electric field levels the same as the reference and the modified scenario.

The capacitive COMSOL model simulated was also based on the geometry shown in Figure 2.

In the two cases presented, during the calculations as well as during the COMSOL simulation, the material considered in between the plates is vacuum. The material characteristics used during the calculation and simulations can be seen

in Table 3. The values are not based on specific details for the materials of a commerial insulator bell, but represent insulator vs conductor and magnetic vs non-magnetic

Property	Variable	Value
Relative permittivity	ϵ_r	1
Relative permeability	μ_r	1
Conductivity	σ_v	0 S/m

Table 3: Material Characteristics of vacuum.

In the last parts of the reports, a simplified model of an insulator bell was investigated. The simulated model of this insulator bell was inspired by several cross-sectional figures of different types of insulator bells found on the internet. The geometry of a single insulator bell used in an insulator chain can be seen in Figure 3. This figure, as was the case for the simple geometry presented earlier, is axis-symmetric, along the left-handmost line.

Figure 3: Geometry of insulator bell that was investigated, the free floating squares seen beside the insulator bell is measurement points were the electric field levels will be recorded.

The insulator bell consists of a cap and a pin to chain a desired amount of bells together. The cap and pin in this case is considered to be made out of steel. In between the cap and the pin, is a skirt. The skirt is considered to be made out of glass. The skirt, cap and pin are held together by cement. The characteristics of the materials used during the simulation within COMSOL can be seen in Table 4.

Property	Material	Variable	Value
Relative permittivity	Steel	ϵ_{rs}	1+4000i
	Cement	ϵ_{rc}	2.1
	Glass	ϵ_{rg}	5
Relative permeability	Steel	μ_{rs}	100
	Cement	μ_{rc}	1
	Glass	μ_{rg}	1
Conductivity (S/m)	Steel	σ_s	$1.45 \cdot 10^6$
	Cement	σ_c	10^{-15}
	Glass	σ_g	10^{-13}

Table 4: Characteristics of materials the insulator bell is assumed to be made from.

3.2 Calculation procedure

When an electric charge is at rest or if it is moving at a constant speed, the electric field radiating from the charge is given by Equation 1.

$$E_r = \frac{q}{4\pi\epsilon_0}\frac{1}{r^2} \tag{1}$$

In Equation (1), q is the charge of the particle, ϵ_0 is the permittivity of free space, r is the radial distance from the charge, and E_r is the electric field strength at this particular radial distance [18].

The radiation pattern from a charge at rest or a charge that is moving with constant speed can be seen in Figure 4.

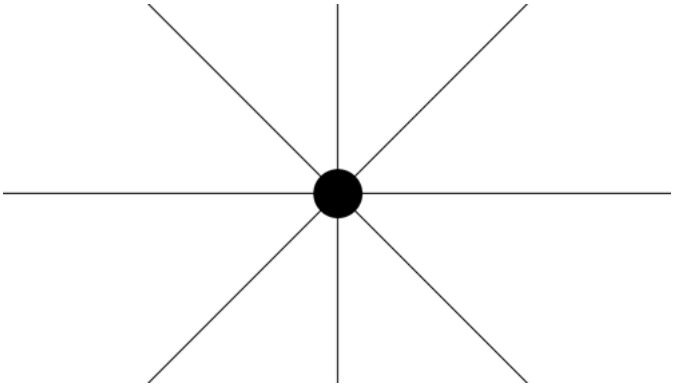

Figure 4: Radiation pattern of electrically charged particle at rest or moving at constant velocity, radially radiating outward away from the particle if positively charged, inwards towards the particle if negatively charged. For a velocities much less than if light, the field id close to uniformly spread around the charge.

When the electron is accelerating, either from rest up to a certain speed or from a constant speed to a lower or no speed, the field lines around the charge will no longer radiate radially towards or away from the particle. Instead of radiating radially from the charge, the field line before the acceleration will have to coincide with the field lines after the acceleration, a simplified view of this phenomenon can be seen in Figure 5.

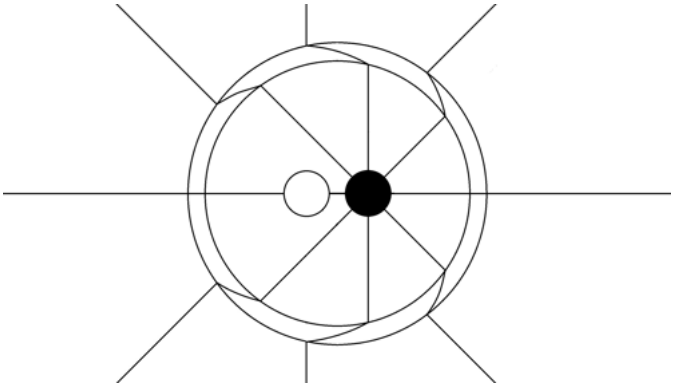

Figure 5: Electric field lines from an accelerating charge: white circle is the position of the charge at rest, black circle is the position of the charge after the acceleration and after some time to give the fields some time to propagate.

In Figure 5, the field lines no longer connect linearly between the two circles surrounding the starting position and the current position of the particle. These two circles represent the distance a wave would propagate during the time the charge is accelerating.

This non-linearity and amplification is what is considered to be an an emitted electric wave. Due to the acceleration of the charge, the charge will have a speed. This will result in the charge radiating a magnetic wave during the acceleration. After the acceleration, the charge will be radiating a magnetic field due to its velocity, but this field will no longer be changing in relation to the charge. It is the change in the electric and magnetic field around the charge that will result in an electromagnetic wave being emitted. Depending on the frequency of this wave, this wave may be referred to by different names, one example is radio waves. Depending on the frequency components of the wave, and the magnitude of the frequency components, there is a possibility of the wave interfering with GPS or other devices using EM waves as means of communication. To drown out the intended signal or by the device in question having high enough susceptibility to either the emitted electric or magnetic fields. The phenomena of accelerating charges is constantly occurring in antennas but at a far greater scale compared to the one electric charge described here.

To determine the electric radiation from an accelerating charge, some assumptions were made. For this derivation to be valid, the following assumptions will be made. Firstly, the acceleration that the charge will be experiencing when placed in the electric field will result in an electron velocity which much less than the speed of light. When low speeds are considered, adjustments due to relativistic effects can be ignored. Otherwise, effects such as "squeezing" of the field lines would have to be considered. With the assumption that the charges will be moving at a speed much less than the speed of light, traditional mechanics for the movement of the charge may be used. A formula of the radiated electric fields surrounding the accelerating charge can now be derived.

If it is assumed that the electron is accelerated during a time Δt to a velocity Δv, which is much less than the speed of light c. If a measuring point is placed at a distance r away from the charge, the distance to the measuring point can be expressed as the time it takes for an EM wave to propagate the distance r to the measuring point. The expression of this is shown in Equation (2).

$$r = ct \tag{2}$$

If the assumption is made that the distance that the charge will travel during its acceleration is short compared to the radius ct. The two circles surrounding the charge, shown in Figure 5. The distance between circles represents the distance an EM wave will propagate during the acceleration. For the field lines before and after the acceleration to coincide, the field lines will have to pass through a strip perpendicular to a line connecting the two circles. The angle between the electric field lines from the black circle and the field lines radiated before the charge was accelerated, can be calculated from a triangle with sides ct and vt, where vt represents the distance the particle has travelled during its acceleration. The amplification of the wave resulting from the acceleration may be calculated by the sine law [18]. With the appropriate angles, Equation (3) will be the result.

$$\frac{\sin(\alpha)}{v\,\Delta t} = \frac{\sin(\theta + \alpha)}{c\,\Delta t} \tag{3}$$

As mentioned earlier, the particles are traveling at speeds far lower than the speed of light. With the aforementioned assumption that the distance the particle is travelling during the acceleration is short compared to the radius to the calculation or measuring point, Equation (3) may be reduced to the equation shown in Equation (4).

$$\alpha = \frac{v}{c}\sin(\theta) \tag{4}$$

With this expression in mind, all field lines that are radiating radially from a charge at rest would normally pass through a linear distance of $r\alpha$. Now that the charge has accelerated during the time Δt, all field lines will now be passing through perpendicular to a distance of $c\Delta t$. This will result in the fields around the charge being amplified by a factor of $r\alpha/c\Delta t$. If α in the amplification factor is substituted by the α solved for earlier and this expression is then multiplied by the electric field radiated by a stationary charge, the expression shown in Equation (5) will be the result for the radiated electric field during a charge's acceleration.

$$E_{\perp}(r,t) = \frac{q}{4\pi\epsilon_0}\frac{v\,\sin\theta}{c^2\,\Delta t}\frac{1}{r} \tag{5}$$

Equation (5) can be simplified further, if $(v/\Delta t)sin\theta$ is considered, $v/\Delta t$ is a simple case of the time derivative of the velocity, or in other words, the acceleration of the charge. $\sin\theta$ is the perpendicular component of the acceleration vector in relation to the radial vector pointing from the charge towards the point of measurement. With these two simplifications in mind, this will result in the following equation for the radiated electric field from an accelerating charge.

$$E_{\perp}(r,t) = \frac{q}{4\pi\epsilon}\frac{1}{c^2 r}a_{\perp}(t - r/c) \tag{6}$$

In Equation (6), r/c is the time it takes for the radiated wave to propagate out from the position of the accelerated charge to a radius of r.

With an expression for the radiated electric field strength from an accelerating charge. The movement of a change present in an electric field will now be derived. Let's consider a simple capacitive model presented in Figure 2. The electric field strength a charge will be exposed to when the two plates in the geometry are set to two different voltage levels is given by expression shown in Equation (7) if the fields are assumed to be homogeneous

$$E(t) = \frac{V_1(t) - V_0(t)}{x_{\text{gap}}} \tag{7}$$

In Equation (7), $E(t)$ is the electric field strength as a function of time, the voltages $V_1(t)$ and $V_0(t)$ is the voltages as a function of time of each one of the co-responding plates. And x_{gap} is the distance between the two plates [18].

This formula for the electric field intensity is valid under the assumption that the charge is far away from the fringing effects that would take place close to and around the corners of the plates. The electric field strength in the case of the calculations is assumed to be homogeneous.

With the assumption that the plates are placed in a vacuum and an electron is present in between these two plates, the force that the electric field will exert on the electron is given by the expression shown in Equation (8).

$$F = Eq \tag{8}$$

In Equation (8), q is the charge of the particle and F is the force the particle will experience due to the electric field at the position of the electron [18].

Equation (7) can be substituted into the expression for the electric field strength in Equation (8), to calculate the force the particle will be affected by when exposed to the electric fields. Equation (9) is an expression for the force the charged particle will experience due to the applied voltage.

$$F(t) = \frac{(V_1(t) - V_0(t))q}{x_{\text{gap}}} \tag{9}$$

If both sides of Equation (9) are divided by the mass of the charge, this will result in a function which describes the acceleration the charge will experience due to the field that is present in between the two plates.

$$a(t) = \frac{(V_1(t) - V_0(t))q}{x_{\text{gap}} m_e} \tag{10}$$

Now that an expression for the electron's acceleration has been solved, since the acceleration is the time derivative of the velocity, the velocity of the particle can be calculated by using Equation (11).

$$a(t) = \frac{dv}{dt} \leftrightarrow dv = a(t)dt \tag{11}$$

If this expression is integrated with respect to time. This will result in an expression for the velocity of the electron whilst inside the geometry boundaries.

$$\int_{v_0}^{v} dv = \frac{q}{x_{\text{gap}} m_e} \int_{t_0}^{t} (V_1(t) - V_0(t))dt \tag{12}$$

If this equation is simplified, The velocity of the electron can be expressed by the following formula.

$$v(t) = \frac{q}{x_{\text{gap}} m_e} \int_{t_0}^{t} (V_1(t) - V_0(t))dt + v_0 \tag{13}$$

In Equation (16), t_0 is the time at which the charge is leaving the top plate, v_0 is the velocity initial velocity of the charge when it is released from the plate.

Now that an expression for the velocity of the particle has been determined. Integrating the velocity with respect to time will result in an expression describing the position of the charges as a function of time. This can be seen in the following equation.

$$v = \frac{ds}{dt} \leftrightarrow ds = v(t)dt \tag{14}$$

If the velocity is integrated with respect to time, the position of the charge will be given by the following formula. But only while the electron is present in between the two plates, and thus in the presence of the electric field.

$$\int_{s_0}^{s} ds = \frac{q}{x_{\text{gap}} m_e} \int_{t0}^{t} (\int_{t_0}^{t} (V_1(t) - V_0(t))dt + v_0)dt \tag{15}$$

As earlier, if this equation is simplified, the following equation gives the position of the charge.

$$s(t) = \frac{q}{x_{\text{gap}} m_e} \int_{t0}^{t} (\int_{t_0}^{t} (V_1(t) - V_0(t))dt + v_0)dt + s_0 \tag{16}$$

In Equation (16), s_0 is the initial positioning of the charge. This initial position of the charge will be at either the upper plate, at a height of x_{gap}, or the lower plate, at an initial position of 0, depending on which one is at a lower potential. Since an electron will accelerate against the direction of the electric field.

With an expressions for the acceleration, velocity, and positioning of the particle have been derived. These equations may be used in Equation (6) to get an expression for the radiated electric field from the accelerating electron. In Equation (6), the distance in this formula is given in a radius r away from the accelerated particle. If an assumption is made that the distance between the two plates is x_{gap}, and a measuring point located is at a height of $x_{\text{gap}}/2$ (in the middle of the plates), at a horizontal distance d away from the current/particle stream, the distance between the particle and the measurement point is given by the Equation (17).

$$r(t) = \sqrt{(s(t) - x_{\text{gap}}/2)^2 + d^2} \tag{17}$$

If r of Equation (17) is substituted into Equation (6). the time it takes for the wave to propagate from the charge to the measuring point will be given by Equation (18)

$$t_d = r(t)/c \tag{18}$$

In Equation (18), t_d is the time delay or time retardation it takes for the radiated wave to travel from the charge to the calculation/measurement point.

With the last variable needed to complete the expression for the radiated electric field level has been solved for, the electric field strength from an accelerating charge is shown in Equation (19)

$$E_\perp(t) = \frac{q}{4\pi\epsilon}\frac{1}{c^2\sqrt{(s(t) - x_{\text{gap}}/2)^2 + d^2}} a_\perp(t - \frac{\sqrt{(s(t) - x_{\text{gap}}/2)^2 + d^2}}{c}) \tag{19}$$

In Equation (19), the distances of d and x_{gap} are short, these two distances will in turn make $r(t)$ short. This will result in the retardation time of the emitted EM wave being very short, which allows for another simplification. Since the distances considered in this model, and thus the time it takes for the EM wave to propagate the short distance between the charge and the measuring point is very small, the delay is short. Since the delay is short, the assumption can be made that the radiated wave will appear at the measuring point instantaneously. This will simplify Equation (19) to Equation (20).

$$E_\perp(t) = \frac{q}{4\pi\epsilon}\frac{1}{c^2\sqrt{(s(t) - h/2)^2 + d^2}} a_\perp(t) \tag{20}$$

If more than one particle were to influence the electric field at this particular measuring point, a summation of the x, y, and z electric field components radiated from the charges present in the homogeneous field are required. This can be done by multiplying the total electric field component coming from one charge with $\cos(\alpha)$ and $\sin(\alpha)$ to get the x and y components respectively. Where α is the angle between the particle and the line d that the measuring point is placed on. This will allow for the inclusion of more than one particle in between the plates.

When the electric field components from each one of the included particles have been summed up, the total electric field experienced at the measuring point can be calculated by the following equation.

$$E_{\text{tot}} = \sqrt{E_x^2 + E_y^2 + E_z^2} \tag{21}$$

In Equation (21), E_x, E_y and E_z is the electric field components along the x, y, and z axes respectively.

By using the calculated field levels, a frequency spectrum can be created by applying the fast fourier transform to the sampled values. From this frequency spectrum, data regarding frequency, magnitude and phase shift for each frequency components experienced at the measuring point can be calculated from the results of said transform.

If the electric field at the measuring point is considered, and the electric field levels are calculated at the measuring point starting at time 0, up until the time t_{duration}. The number of samples n_{sample} necessary to generate a frequency spectrum up to a certain frequency f_{max} can be calculated by the following equation.

$$n_{\text{sample}} = 2f_{\text{max}}t_{\text{duration}} \quad \text{or} \quad n_{\text{sample}} = \frac{2f_{\text{max}}}{f_{\text{base}}} \tag{22}$$

In Equation (23), f_{base} is the base frequency of the sampled time.

When sampling the time duration in question, with this amount of samples, this would correspond to a sampling frequency which can be calculated by the following formula.

$$f_{\text{sample}} = f_{\text{base}}n_{\text{sample}} \tag{23}$$

In Equation (23), f_{sample} is the rate at which the electric field will have to be sampled to create a frequency spectrum up to the desired max frequency, following the Nyquist sampling theorem [12].

In all cases related to sampling, one has to be careful that there are no significant levels of harmonics above half the sampling frequency. If this is not the case, the frequency spectra resulting from the fast Fourier transform will experience aliasing. This will result in misleading magnitudes for the sampled frequencies.

Firstly, a purely DC case was considered, where a constant negative voltage was applied to the top plate. This will result in electrons accelerating from the top to the bottom plate, which in this case was considered to be grounded. When an electron reached the bottom plate, the particle's velocity was reset to zero and the charge was moved to the top plate. This was done during the entire duration of 1 µs, with a sampling frequency of 5 GHz, following Equation (23) to ensure that the FFT determines a frequency spectrum up to a frequency of 2.5 GHz.

3.2.1 Deliminations, simple geometry, calculation stage.

In the following list, the simplifications that were made for the model that was calculated using Matlab can be seen.

- Particle-particle interaction has not been considered, meaning the EM fields originating from one particle and interacting with other particles in between the two plates have not been considered. This will result in the particle's movement would change if these forces were to be considered. However, the significance of these forces can be argued to be small. The electric field a charge emits will be at much lower levels compared to the electric fields due to the applied voltage. Therefore the forces from one charge exerted upon another charge will be small compared to the much greater force due to the voltage applied to the geometry. With respect to the magnetic field, all charges are accelerating in a perfect line. The magnetic fields due to the movement of these particles will not affect the other charges.
- In between the two disks of the simple geometry, it is assumed that there are no other particles. It is considered to be a total vacuum in between the two plates, resulting in the particles in the beam to not experiencing friction, collisions, or the potential of being absorbed by other particles or molecules.
- When a particle hits one of the two plates, either the upper or the lower one, the particle is transported to the plate which is at a lower potential, and the velocity of the particle is reset to zero in all directions.
- Relativistic effects have not been considered. However, it could be argued that it is not necessary when the speed the particle reaches during the acceleration is low compared to the speed of light.
- Due to long processing times and memory limitations, the duration that the electrons were allowed to be moving in between the two plates had to be kept fairly short. With a baseline frequency of 1 MHz, or measuring the electric fields from the particles in between the two plates during a time window of 1 µs with a sampling frequency of 5 GHz, to determine a frequency spectrum up to a frequency of 2.5 GHz, according to the formulas explained earlier. This was done to measure past the bandwidths that the three different GPS signals are occupying.

At the start of the project, the base frequency of the calculations and simulations was 50 Hz. However, due to the amount of memory the COMSOL simulations required, the computer crashed repeatedly when the simulation was run. This is why the simulation base frequency was changed to 1 MHz.

During the calculation stage of the project, a few different scenarios were tested for the capacitive model. Three different scenarios of the voltage levels were kept constant and the distance between the two plates was varied. In three different scenarios, the distance was kept constant and the voltage levels the plates were exposed to were changed. Four more scenarios were also tested, low and high voltage at a short distance between the two plates, and low and high voltage at a long distance between the two plates. The parameters of the different scenarios can be seen in Table (5).

Scenario:	Voltage (kV)	Gap height (m)	Charges
Base Scenario	10	0.1	10
1	10	0.1	1
2	10	0.1	100
3	10	0.2	10
4	10	0.05	10
5	20	0.1	10
6	5	0.1	10
7	20	0.2	10
8	20	0.05	10
9	5	0.2	10
10	5	0.05	10

Table 5: Testing conditions for different scenarios for the simple capacitive model during the Calculations in Matlab

For all tested scenarios, in the calculations and the simulated models, the electric field radiated from the charges in between the two plates was measured at certain predetermined distances, which can be seen in Table (6).

Point	distance (m)
1	0.1
2	0.3

Table 6: Horizontal distance from the particle stream. Positioned in the middle of the plates, a height of $x_{\text{gap}}/2$.

The results from the calculations of the simple capacitive model with accelerating charges can be found under section 5.1.

3.3 Charge Simulation

In this section, the setups used within COMSOL will be described, the deliminations made during the simulations will also be covered in this section.

3.3.1 Capacitive geometry. The first step was to create the simple capacitive model, which is shown in Figure 2 in section 3.1. The reference dimensions of the capacitive model can be found in Table (2). The pins and the disks of this model were considered to be made out of metal.

According to Henri Benisty et al [16], within the radio frequency spectra and the infrared spectra, in between 3 kHz and 400 THz [3][10], the permittivity of metals can be split up into real and imaginary components. The real permittivity of the metal can be approximated to 1 while the complex permittivity is a very large number. The permittivity can be approximated as shown in Equation (24) [16].

$$\epsilon(\omega) \approx \epsilon'(\omega) - i\epsilon''(\omega) = \epsilon_0 + i\frac{\epsilon_0 \omega_p^2 \tau}{\omega} \tag{24}$$

In Equation (24), ϵ' and ϵ" is the real and imaginary parts of the permittivity respectively. ϵ_0 is the permittivity of vacuum, ω is the angular frequency of the applied field, ω_p is the plasma frequency of the metal, and τ is the damping time, which according to [16], is usually in the magnitude of 10^{-14} s.

This complex permittivity in turn will result in any metal the structure is considered to be made out from having a complex relative permittivity which is approximately equal to the expression shown in Equation 25.

$$\epsilon_r(\omega) \approx 1 - i\frac{\omega_p^2 \tau}{\omega} \tag{25}$$

The high permittivity will result in the electric field inside the disks and pins being approximately the same, and the potential of each respective pin to be close or equal throughout the entire pin-disk geometry.

The top pin is set to a negative potential V_{in}, while the lower plate is considered to be grounded. This geometry is used to keep the electric field close to homogeneous. This will result in the electrons accelerating from the upper plate towards the lower disk because electrons will be accelerating in the opposite direction of the electric field. In the case for DC voltage, a single electron inlet was considered. The inlet at the top plate is considered to be in the middle of the top disk since the geometry shown in Figure 2 is axis-symmetrical around the left-hand most vertical line. In the case of AC voltage, 2 different electron inlets were considered, one on the top plate and one on the bottom plate. The two electron inlets will inject electrons into the geometry when each respective plate is at a lower potential than than that of the other plate. This results in a specific inlet only emitting electrons in the case that the electrons emitted would be accelerating away from the inlet itself. The electrical as well as sampling properties of the reference model can be seen in Table (7).

Parameter	Value
Voltage	10 kV
Current	1 A
Base frequency	1 MHz
Sampling Frequency	5 GHz
Charge releases	6240
Charges per release	10
Charge Multiplication factor	$0.1 \cdot 10^9$

Table 7: Values of parameters that were used in the simulation model that is considered to be reference values of COMSOL simulation.

3.3.2 Charge simulation delimitation. In this section, all deliminations made in the charge simulations in COMSOL are presented.

- In this model, particle-particle interaction was considered, this results in three types of forces acting on a charge during the simulation. The first is the force from the electric fields resulting from voltages applied to the geometry. The second force comes from the electric field radiated from one charge and will act upon the other charges in the model. The third force acting on the introduced charges comes from the radiated magnetic fields from charges due to their velocities.
- The charges will be multiplied with a multiplication factor, whose reference value can be seen in Table (7). This means that both the mass and the charge of a single simulated charge will be multiplied by this value instead of simulating that many individual charges.
- It is assumed that a total vacuum is present between the two plates of the geometry. The characteristics of the considered vacuum can be seen in Table (3). This will result in the electrons moving between the two disks not experiencing collisions, absorption, or interactions with other particles except for the interactions with other electrons in the surrounding geometry.

- When one electron collides with either the top or bottom disk, or other parts of the geometry, the charge will disappear. The exception is when a charge collides with the axis-symmetry line. In this case, the particle bounces instead of being stuck or disappearing on an interaction which is a result of the geometry being axis symmetric.
- Electrons are injected into the geometry at constant intervals, throughout the duration of the test. This was done following the old definition of current. The number of released charges during the sampling window can be calculated with the expression shown in Equation (26).
- In the case that an AC voltage is applied to the top plate, the release times are not altered, the charge multiplication factor is instead changing sinusoidally. This will result in a very small current running when the voltage magnitude is close to zero and a higher current running when the voltage magnitude is high.
- The base frequency of the simulations will be increased from a planned 50 Hz, to 1 MHz. The decrease in simulation time was due to memory limitations and long processing times.

$$n_{Qs} = \frac{It_{\text{duration}}C_0}{nQ_r} \tag{26}$$

In Equation (26), n_{Qs} is the number of times electrons will be injected into the geometry, I is the current that will be running through the geometry, C_0 is the number of charges in a coulomb, $6.24 \cdot 10^{18}$, n is the charge multiplication factor, and Q_r is the number of charges that will be released per injection.

3.4 Plasma simulation

This section will cover two different simulation setups, the first being the capacitive model described up until now. The geometry of this model is shown in Figure 2. The dimension of the model is shown in Table (2). The second model is an approximated design of an insulator bell which is used within insulator chains for power grid applications. The geometry of the insulator chain can be seen in Figure 3.

3.4.1 Plasma simulation, capacitive model. This model is set up in a similar way as the models used before this. A negative alternating voltage is applied to the entirety of the top pin, while the entire bottom pin is grounded. The material in between the two plates is considered to be purely nitrogen gas, which will constitute the plasma. It was considered to be purely nitrogen gas since that makes up about 78 % of the molecules in air [31].

3.4.2 Plasma simulation, Insulator Bell. This model is different compared to the capacitive model. In this model, the pin at the bottom om the insulator bell, the part used to chain multiple bells together has an alternating voltage source applied to it, as is the case in AC grids. The cap of the insulator bell is considered to be grounded. In between the cap and the pin will be two layers of cement, holding an insulating glass. The properties of the materials discussed here are shown in Table (8).

Material	Relative permittivity ϵ_r	Conductivity σ	Relative Permeability μ_r
Cement	2.1	10^{-15}	1
Glass	5	10^{-13}	1
Steel	1+4000i	$1.45 \cdot 10^6$	100

Table 8: Material Characteristics of materials used in insulator bell plasma model.

The characteristics of the materials used in the insulator chain are considered to be constant, under the assumption that the materials used in the insulator bell are exposed to electric field levels low enough to keep them from ionizing.

The remaining part of the geometry, surrounding the insulator bell, is considered to be nitrogen gas, which will be able to ionize and be a part of the plasma.

3.4.3 Plasma properties. The plasma considered in the capacitive and the insulator bell models is considered to be made out of nitrogen gas. This plasma will be constituted by four different species. The species included within the plasma is shown in Table (9).

Species	Charge	Molar mass(kg/mol)	Initial number density
N_2	0	0.02801	-
N_2^+	+1	0.02801	10^6
N_2^-	-1	0.02801	10^6
e	-1	$5.485 \cdot 10^{-7}$	10^{10}

Table 9: Plasma species making up the plasma, specified with charge, molar mass, and initial number density. N_2 being unionized nitrogen gas, N_2^- and N_2^+ being the anion and ion respectively of nitrogen gas and e being the electron.

The remaining parts of the plasma will be constituted by non-ionized nitrogen gas to bring the gas pressure up to a pressure of 1 atmosphere.

In the capacitive model and the insulator bell model, there will be four different reactions that these four nitrogen species can undergo during the simulation.

$$N_2 + e \rightarrow N_2^+ + 2e \tag{27}$$

$$N_2 + e \rightarrow N_2^- \tag{28}$$

$$N_2^+ + e \rightarrow N_2 \tag{29}$$

$$N_2^+ + N_2^- \rightarrow 2N_2 \tag{30}$$

The forward rate for each respective reaction in plasma can be seen in Table 10.

Reaction	Forward rate constant
$N_2 + e \rightarrow N_2^+ + 2e$	$1.4 \cdot 10^2 e^{(-660/E_{rd})} N_n \cdot 3.74 \cdot (E_{rd}^{-0.25}) E_{rd}/c_{w_{N_2}}$
$N_2 + e \rightarrow N_2^-$	$6 \cdot 10^{-1} e^{-100/E_{rd}} N_n \cdot (3.74 E_{rd}^{-0.25} E_{rd})/c_{w_{N_2}} + 1.6 \cdot 10^{-15} E_{rd}^{-1.1} N_n^2 \cdot 3.74 E_{rd}^{-0.25} E_{rd}/c_{w_{N_2}}$
$N_2^+ + e \rightarrow N_2$	$5 \cdot 10^{-8} \cdot N_{A_{const}}$
$N_2^+ + N_2^- \rightarrow 2N_2$	$2 \cdot 10^{-6} \cdot N_{A_{const}}$

Table 10: Plasma reaction rates for each respective reaction

In Table 10, E_rd is the reduced electric field, N_n is the density of neutrally charged particles, $c_{w_{N_2}}$ is the molar concentration of unionized nitrogen gas atoms and N_A is the Avogadro constant which is equal to $6.02214076 \cdot 10^{23}$

Another attribute that the anions and the ions have is that whenever either of the two interacts with a surface which is grounded or set to the voltage applied to the geometry, the positively or negatively charged nitrogen molecules will turn back to uncharged nitrogen molecules.

4 LABORATORY MEASUREMENTS

In this chapter of the paper, the procedures of experimental setups are described, equipment used for test setup, how measurements were taken, descriptions of why measurements were taken in a certain way, and the software used to process measured values, are all presented in their own sections under this chapter.

4.1 Phone GPS app analysis

This section describes the procedures of the measurements taken when performing GNSS signal-to-noise ratio (SNR) measurements by using a cell phone close to a spark between two insulator bells or a gap between two crocodile clips, to see whether these could interfere with GNSS signals received by a mobile phone.

4.1.1 Test objects. In this section, the test objects used during the first and second tests respectively are presented.

During the first test, four capacitors in series were used. Two crocodile clips were connected across one of the capacitors. The voltage across one capacitor would allow for the generation of an arc between the crocodile clips when a voltage of high enough magnitude was applied across the capacitors. The capacitors are shown in Figure 6, the clip on the bottom connects to the high voltage side of the transformer, while the top wire connects the capacitors chain to ground. This setup was chosen for its similarity to a crack in the skirt of an insulator bell, although the capacitances and distance are not chosen to match this perfectly.

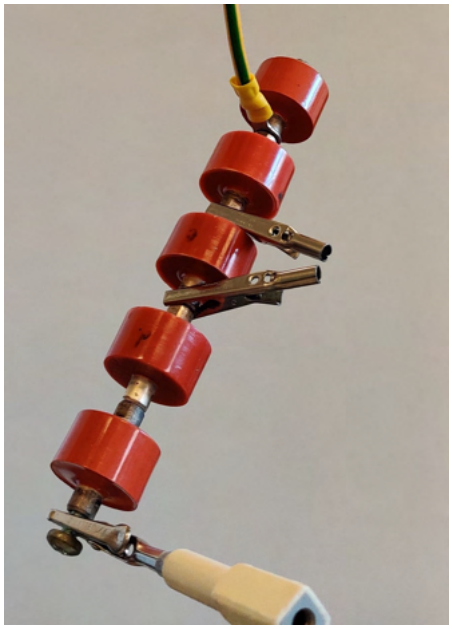

Figure 6: Series capacitors with two crocodile clips cross one of the capacitors.

Each capacitor of the divider shown in Figure 6 has a rated value of a 100 pF.

During the second SNR recording test, two insulator bells connected in a chain were used. To create a gap contact between the two insulator bells, a piece of silicone rubber was inserted between the iron cap of the bottom bell and the pin of the top bell. Since the two bells are no longer connected, a spark occurred between the bottom bell's cap and the top bell's pin when a voltage of high enough magnitude was applied to the chain. This happens when the capacitive

field distribution between the solid insulation parts and the gap causes the gap voltage to reach its breakdown level; a breakdown causes a breif spark, which reduces the gap voltage and increases the voltage across the solid insulation parts in the insulator string. The second test object is shown in Figure 3. The pin holding the two bells at the top is grounded, and the high-voltage side of the transformer would be connected to the pin of the bottom bell.

Figure 7: Insulator chain with two bells.

The dimensions of the silicone rubber piece used to separate the pin of the top insulator bell from the cap of the bottom bell is shown in Figure 8.

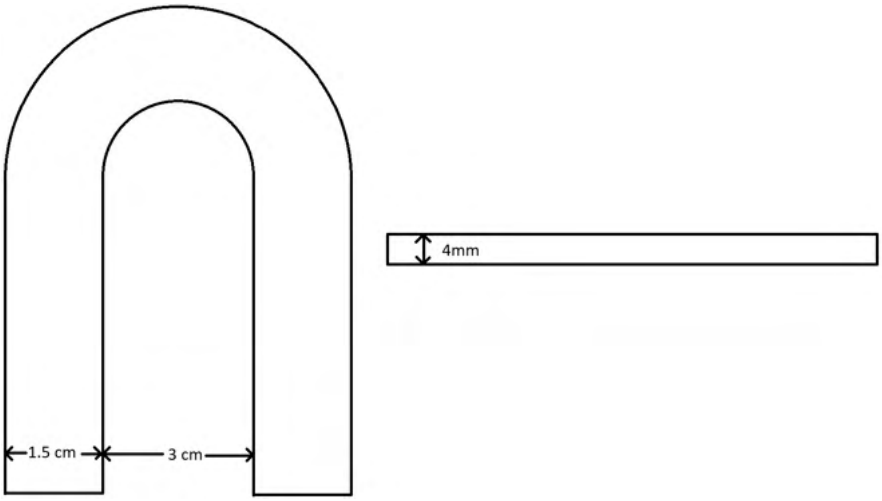

Figure 8: Dimensions of the silicone rubber piece used to create the desired gap between the two insulator bells.

This silicone rubber piece was about 4mm thick, and each leg of the silicone piece was about 1.5cm wide. This piece could be strung around the top insulator's pin, which allowed the second insulator bell to be connected to the top one without making metal-to-metal contact. This would create the desired sparking situation that was desired.

4.1.2 Procedure. The first step of the testing procedure is to procure background measurements ahead of the measurements with the spark present. This was done by placing the phone at a distance of 4 meters away from the spark setup. This was very close to one of the windows to the outside of the testing lab. When the phone was in place, the ambient SNR of each incoming satellite signal was recorded. Background measurements were recorded for 1 minute.

When the background test had been recorded, a new recording session was started. Then as fast as safely possible, the test area was left and a voltage of 22 kV was applied to the test setup. The need to perform the background testing and the measurements with the spark present as close to one another in time as possible is so that the signal strength from one satellite is not significantly changed due to the movement of the satellite during the duration of the two tests.

The applied voltage was chosen so that a regular spark would be generated across the intentional gap of the test object. The test objects used during the cell phone tests are discussed in more detail in section 4.1.1. The first object to be tested was the set of series capacitances with crocodile clips applied across one of the capacitances. The test object was exposed to the voltage for close to 2 minutes to allow the phone app to report stable SNRs in the presence of the sparking.

After this time had expired, the necessary grounding procedures were carried out. These were mainly the grounding of the transformer used to apply the voltage to the test setup and the grounding of the test setup to ensure the safety of the test personnel. After the necessary groundings had been carried out, the recording was finally stopped.

The procedure described above was repeated during the testing of the insulator chain with an intentionally introduced loose contact by utilizing a piece of silicone rubber between the two insulator bells.

When all measurements had been carried out, the SNR values recorded in the app were imported to MATLAB, where the mean and standard deviation of the SNR values were calculated. An overall SNR difference between the background measurements and the measurements in the presence of the sparking situation was also calculated.

By performing these tests and performing the calculations explained above, it would be possible to determine if the spark could have a negative impact on the signal-to-noise ratio of the received GNSS signals.

4.1.3 Equipment. The following equipment was used during the cell phone SNR testing.

- Phone: OnePlus 7T HD1903. This phone had the associated GPS monitoring app, NMEA Tools, version v2.8.05, that was used to conduct the tests.
- HV test set with a step-up transforming giving a variable 0–100 kV output, measuring on a peak meter through a capacitive divider
- One of the two test objects described in section 4.1.1.

4.1.4 Software. The main software used to record the signal-to-noise ratio measurements was an app called NMEA Tools, version v2.8.05. This app allows for logging of the device's location. At the time of the measurements, the app did not allow one to record the signal-to-noise ratios of each one of the received satellite signals. To record the SNR of the incoming signals, the cell phone could be set to record its screen. In this way, the signals with the highest SNR values could be recorded still. All received signals could not be recorded due to the layout of the app.

MATLAB was used to store all recorded values, it was also used to calculate the mean values, standard deviations, and the total mean difference.

4.1.5 Signal analysis delimitations. The app used for SNR measurements allowed tracking of the device recording. This data could be saved to a file, but this tracking only included the position of the device. This was solved by recording the screen of the phone while the SNR of the GPS signals were present on the screen. This limited the number of signals whose SNR values could be recorded, this in turn limited the the selection of satellites whose data are to be saved since the satellite had to be recorded both during the background tests as well as during live spark tests.

During the two conducted tests, 8 different satellites were tracked whose SNR values were recorded. These satellites varied in initial signal strength, to not only record the satellites that were directly overhead. During the two conducted tests, one of the picked satellites at the lower ends of the recorded SNR levels usually dropped low enough to leave the recorded screen. When this occured, the satellite was left out of the calculated mean and standard deviation. The SNR values of the satellite were still recorded. This was done to keep the calculated mean and standard deviation representative of the values that were recorded. In the end, this resulted in the SNR of 7 satellite signals being recorded in full during the two test scenarios and these values were used to calculate the mean, standard deviation, difference, and mean total difference of the SNR values measured.

4.2 Spectral Analysis

In this section, a description of the procedures followed during the spectral measurements during the sparking situations that were created will be presented, the equipment that was used to perform the spectral analysis will be covered, and the software used and calculations made to arrive at the results are also presented. To conclude this section, the delimitations made during the tests will be covered.

4.2.1 Equipment. The following equipment was used to measure the frequency spectrums of the electric field levels.

- Spectrum analyzer: Rohde & Schwarz ZNLE6 Vector Network Analyzer 1MHz - 6GHz.
- Antenna: Satimo Quad Ridge QH800 800 MHz - 12 GHz Horn.
- HV test set with a step-up transforming giving a variable 0–100 kV output, measuring on a peak meter through a capacitive divider
- Test objects presented in section 4.2.4.
- Computer with MATLAB.

The spectrum analyzer, the mounting solution, and the antenna used during the spectral measurements can be seen in Figure 9.

Figure 9: Setup used to perform spectrum analysis

In Figure 9, the antenna can be seen pointing towards the bottom left side of the picture. The antenna used has a frequency bandwidth ranging from 800 MHz up to 12 GHz. The spectrum analyzer has a bandwidth ranging from 1 MHz to 6 GHz. To ensure that the measurements are taken in the bandwidths of the two devices, all measurements will be performed within the 800 MHz to 6 GHz region.

4.2.2 Software. To determine the peak values for each frequency component in the frequency spectra captured during all spectrum measurements, MATLAB was used to process the images, calculate each frequency level, and plot the resulting frequency spectrum for each test object.

4.2.3 Procedure. The purpose of this test is to determine if there is a difference in the spectral emissions radiated from a spark compared to if there is no spark present. To do this comparison, the background spectrum has to be compared to the spectrum when a live spark is present at the test setup.

Each test was started with a recording of the background levels in the frequency range of interest. The background peak levels were recorded by pointing the antenna directly at the test object and starting a new recording. This was performed before all tests except when the wires were shorted. In this case, no antenna was connected to the wires, and therefore no need to point it in a certain direction since the wires were shorted. The background levels were recorded for 1 minute. For each object tested, a new set of background levels was recorded for 1 minute shortly before each recording of the peak field levels with a voltage applied to the test object. To measure the background levels for 1 minute before each active test was done so that if there is an error with no clear explanation during a single background measurement, it will not affect all measurements that will be recorded. It will also be helpful to observe the frequencies that are to be expected in the background, to ensure that a detected frequency peak is written off as it was coming from the spark. The peak levels were recorded during the background tests and during the tests with the spark present due to the applied voltage at the test object. A screenshot of the recorded background peak levels was saved and in the processing stage, the field levels of each frequency component.

When the background peak levels had been recorded, a new recording was started. The new recording will store the peak frequency levels observed when the voltage is applied. With a new recording started, the testing area was vacated and a voltage of 22 kV was applied to the test object. The voltage level was chosen so that a spark was generated at the test object. The voltage was applied to the test object for 1 minute.

After the 1 minute had passed, the voltage was turned off, and the necessary grounding procedures were followed. These included grounding of the transformer used and grounding of the test object. Then a screenshot of the measured frequency spectrum was saved. This second screenshot also acted as data during the processing stage.

With the two screenshots, one of the background levels, and one with the levels when the spark is present, these two figures were processed using MATLAB. During the processing of these figures, the peak levels measured for each frequency component were determined: this was done for the background measurements and the measurements with the spark present. When a vector containing the recorded peak levels measured at the antenna (dBm) for each frequency component had been obtained from the two screenshots, the frequency-dependent antenna gain was subtracted from the background and the active test values.

The procedure described above was repeated for each one of the tested scenarios. All tested scenarios and settings during each respective scenarios is shown in Table 11, while a more detailed description of each test object can be found under section 4.2.4.

4.2.4 Test objects. In this section, each one of the test objects will be presented from Table 11.

During the first measurement, 4 capacitors in series were used. On each side of one capacitor, two crocodile clips were connected and pointed slightly towards one another. When applying a voltage to this capacitor chain the two applied clips allowed an arc to be generated between the two clips when a voltage of 22 kV, 50 Hz is applied. This model was also used during the GPS signal-to-noise measurements using a mobile app, the capacitor chain can be seen in Figure 6.

During the second, 6th, 7th, 8th, 10th, and 11th tests, two insulator bells that can be connected in a chain were used. These insulator bells were separated by stringing a silicone rubber piece around the pin of the top, thereby creating

Measurement	Object description	Distance (m)	Frequency range (GHz)	Voltage (kV)
1	Series capacitors with crocodile clips	7.15	0.8 - 3	22
2	Insulator chain with silicone rubber piece	7.15	0.8 - 3	22
3	Insulator chain, no spacer between bells	7.15	0.8 - 3	22
4	Insulator chain with insulator tape	7.15	0.8 - 3	22
5	Insulator chain with insulator tape, confirmation	7.15	0.8 - 3	22
6	Insulator chain with silicone rubber piece, confirmation	7.15	0.8 - 3	22
7	Insulator chain with silicone rubber piece, opening away from antenna	7.15	0.8 - 3	22
8	Insulator chain with silicone rubber piece	3.85	0.01 - 6	22
9	Grounded ports on wires connecting to the antenna	3.85	0.01 - 6	22
10	Insulator chain with silicone rubber piece, lower antenna port	3.85	0.01 - 6	22
11	Insulator chain with silicone rubber piece, antenna 90° away from chain	3.85	0.01 - 6	22
12	Insulator chain with warning tape	3.85	0.01 - 6	22
13	Insulator chain with warning tape, antenna 90° away from insulator chain	3.85	0.01 - 6	22
14	Corona board	3.85	0.01 - 6	50
15	Thin vertical wire	3.85	0.01 - 6	50
16	Thin horizontal wire	3.85	0.01 - 6	50
17	Insulator chain with thin cardboard	3.85	0.01 - 6	22
18	Insulator chain with insulator tape	3.85	0.01 - 6	22
19	Insulator chain with insulator tape, re-testing	3.85	0.01 - 6	22
20	Insulator chain with insulator tape, opening away from antenna	3.85	0.01 - 6	22
21	Insulator chain with insulator tape	7.15	0.01 - 6	22
22	Insulator chain with insulator tape, antenna 180° away from insulator chain	7.15	0.01 - 6	22
23	Grounded ports on wires connecting to antenna, insulator tape	7.15	0.01 - 6	22

Table 11: Order of measurement and a short description of the test object, measured distance, and measured frequency range, and voltage applied to the test object during each test

a gap between the pin of the top insulator and the cap of the bottom insulator. When these two bells were separated by the silicone rubber piece, an arc would result when a 20 kV, 50 Hz voltage was applied across the two bells. The insulator chain can be seen in Figure 7 and the dimensions of the rubber piece can be seen in Figure 8.

In the third test, the insulator bells shown in Figure 7 were used as intended; no spacer was placed between the top bell's pin and the bottom pin's cap.

During the 4th, 5th, 18th 19th, 20th, 21th and 22th test, the insulator bells in Figure 7 were used, but the effects of a smaller insulating layer distance were investigated. By separating the bells by two pieces of insulator tape folded in half 2 times, i.e. 4 layers of insulator tape. The two insulator bells separated by insulator tape are shown in Figure 10.

Figure 10: Yellow and green insulator tape separating the top bell from the bottom bell

During the 9th and 23rd tests, no antenna was used, the wire connecting the antenna to the spectrum analyzer was shorted, and the interference the wire or spectrum analyzer picked up from the background compared to when a live voltage connected to test object was measured. The shorted ends of the wires can be seen in Figure 11.

Figure 11: Shorted ends on the wires connecting to the antenna.

In tests 12 and 13, a piece of warning tape was used to insulate the insulator bells from one another, the piece was even thinner than the pieces of insulator tape used between the bells during the other tests. It was used in the same way that the insulator tape was and is illustrated in Figure 10, but was not folded over. This was done to observe the effects of an even thinner insulating layer.

In tests 14, 15 and 16, measurements of scenarios that could be argued to be closer to a corona situation were taken. The 3 tested scenarios can be seen in Figure 12.

Figure 12: Corona measurement setups, On the left side, a plastic board with needles connected to the high voltage side of the transformer. On the right side, two boards hold a metal wire which is connected to high-voltage.

In the remaining testing scenarios, one of the test setups presented above was used and modified by rotating the test object in question or the antenna. One example of this is test 7, where the opening in the insulator cap for the other insulator's pin presented in Figure 10 is facing away and possibly shielding the antenna from the interference source. These tests were performed to confirm that the interference was coming from the test object; they also helps to determine how much of the signal is reflected from the walls surrounding the test object.

4.2.5 Spectral analysis delimitations. One delimitation made during the recording of the background and spark electric field level measurements was to save the peak spectral values in a screenshot format from the spectrum analyzer. Saving the recorded peak values in a picture was required because when saving the recorded values in a numerical format, the spectral analyzer saved only the most recent frequency sweep, not the peak levels over all sweeps recorded during the duration of the test. This was the case even though the max peak values were recorded on the spectrum analyzer's display. By doing this, some measurement resolution is lost due to the limited screen resolution. To determine the magnitudes of each frequency component, a Matlab function was written to read the magnitude from the saved line in the screenshot. An example of a figure before the MATLAB processing stage can be seen in Figure 13.

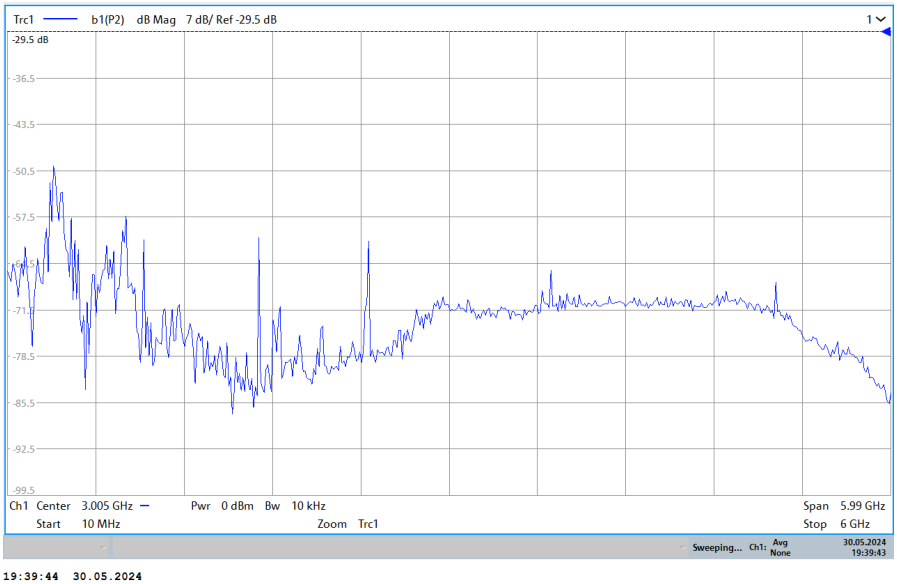

Figure 13: Screenshot from spectrum analyzer, an unprocessed image.

5 RESULTS

In this chapter, the results from the calculations, simulations, and measurements covered in sections 3 and 4 are presented.

If more results from any of the aforementioned sections are desired. These can be found in the appendix.

5.1 Calculation from the capacitive model

This calculation was based on a slinge charge accelerated in between the two plates, with respect to the delimitations covered in section 3.2.1. The electric field strength radiated from the charge experienced at the two measuring points can be seen in Figure 14.

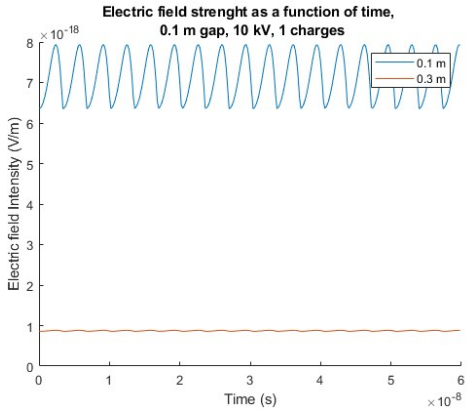

Figure 14: Radiated electric field as a function of time. 1 charge, a potential of 10 kV, distance between the two plates of 0.1 m. The figure shows a short window of the electric field as a function of time. The pattern seen in the window is repeating, up until the end of the sampling period, which is 1 µs.

The fast fourier transform is then applied to the sampled electric field levels at the measuring points to determine the frequency characteristics of the electric field levels experienced at each one of the points. The frequency spectra from the samples of Figure 14 can be seen in Figure 15 The linear values can be seen in the figure to the left, while the same spectra but with logarithmic axes can be seen the right figure.

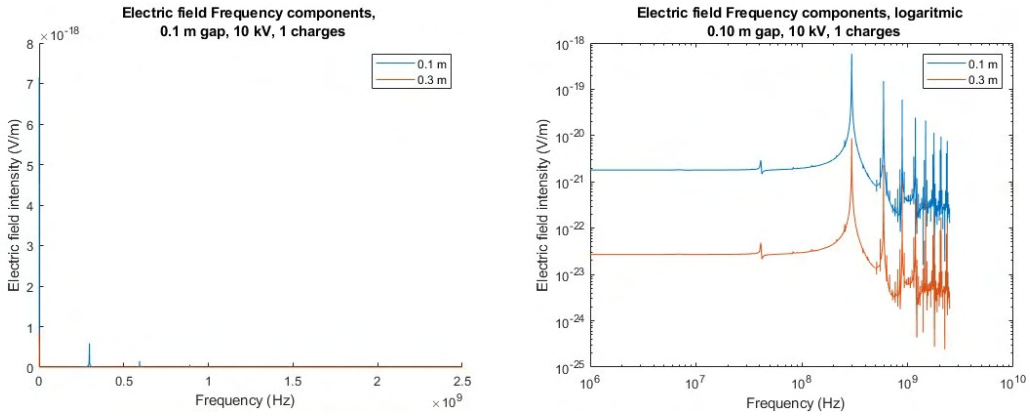

Figure 15: The frequency spectra of the electric field for 1 charge, a voltage of 10 kV is applied with a plate gap of 0.1 m. Normal spectrum on the left, same spectrum with logarithmic axes on the right.

As stated earlier, more scenarios were covered, if more results from other calculated scenarios are desired. For example, scenarios with higher or lower voltage levels, longer or shorter plate separation distances or scenarios with more or fewer charges can be found in the appendix.

5.2 COMSOL

In this section, the results of two simulated scenarios are presented. In the first subsection, the results of a DC voltage simulation are presented. In the second subsection, an AC voltage simulation is presented. In the third section, the results from the plasma simulation of the simple geometry will be covered. In the last section, the results from the plasma simulation of the improvised insulator bell that is used within an insulator chain will be presented

5.2.1 Capacitive model, DC. Measurement points were placed between the two plates at a distance according to Table 6 away from the current stream. The simulated electric field levels can be seen in Figure 16.

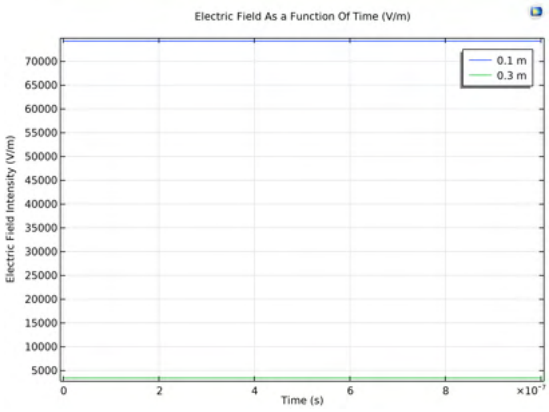

Figure 16: Electric field, 10 kV DC, 0.1 m gap, 6240 distinct releases of electrons.

Based on the sampled values, the FFT was applied to the measured field levels. This resulted in the frequency spectrum shown in Figure 17.

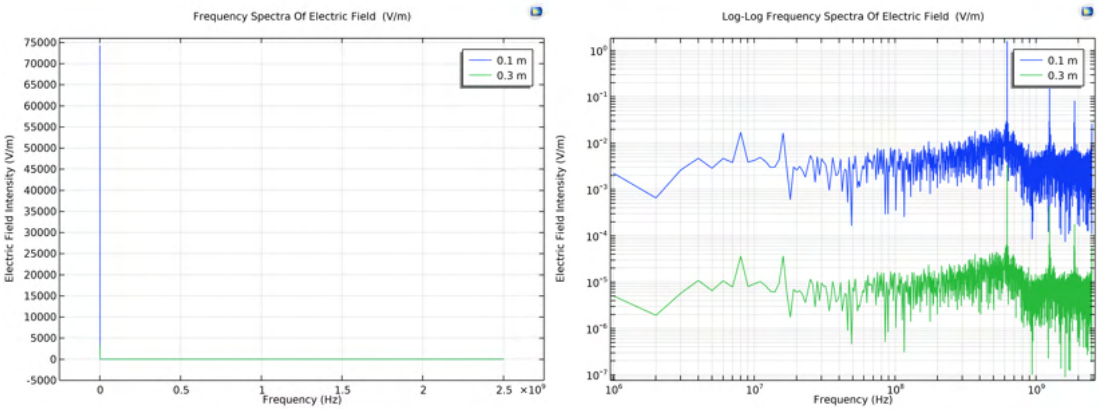

Figure 17: Electric field frequency components, 10 kV DC applied voltage, 0.1 m gap, 6240 distinct releases of electrons. Normal spectrum on the left, same spectrum with logarithmic axes on the right.

If more figures from other scenarios are desired, more figures from other tested scenarios with different voltage levels, electric field levels or different gap heights, these can be found in the appendix.

5.2.2 Capacitive model, AC. In this section the electric and the spectra for the tests conducted with an applied AC voltage are presented. In this model charge multiplication factor is alternating sinusoidally as well, to keep the current alternating in accordance to the applied voltage.

The electric field values at the two measurement points can be seen in Figure 65.

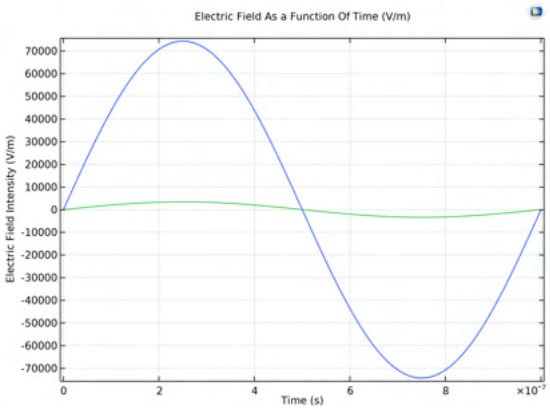

Figure 18: Electric field, 10 kV AC, 0.1 m gap, 6240 distinct releases of electrons.

If the FFT is applied to the sampled values seen in Figure 18. The spectra seen in Figure 19 are the results.

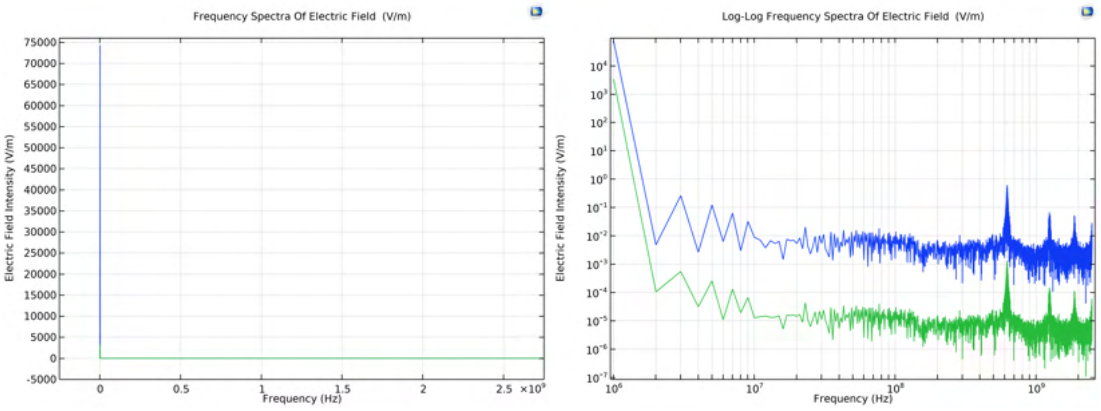

Figure 19: Electric field frequency components, 10 kV AC, 0.1 m gap, 6240 distinct releases of electrons. Normal spectrum on the left, same spectrum with logarithmic axes on the right.

If more figures for other tested setups are desired, these can be found in the appendix section .3.3, where other scenarios with alternating voltages were tested.

5.3 Plasma simulation

In this section, the results from the two plasma simulations that were carried out are presented.

5.3.1 Capacitive model. When the simulation was run under the conditions described under section 3.4, the electric field in this capacitive model were measured at a distance of 0.1 and 0.3 m away from the current stream. The capacitive model is shown in Figure 2, while the simulated electric field levels at the measuring points can be shown in Figure 20.

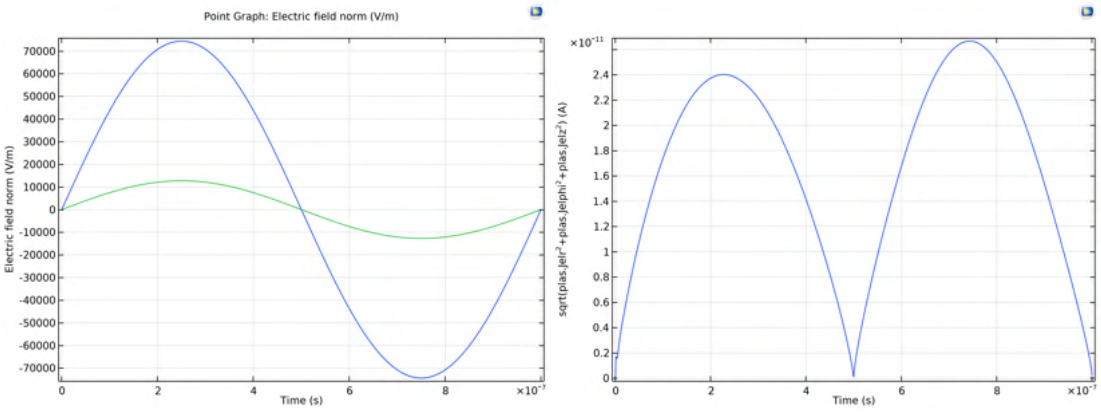

Figure 20: Electric field levels, plasma simulation. Figure on the left shows electric field levels while the figure on the right shows the current magnitude through the geometry.

If the FFT is applied to the electric field levels that were measured, the electric field frequency spectra resulting from this can be seen in figure(21).

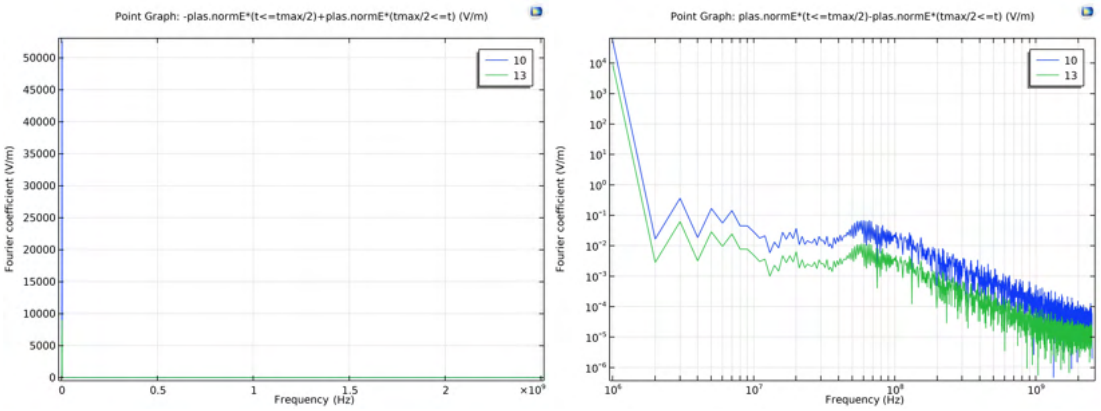

Figure 21: Electric field spectra, 10 kV AC. Normal spectrum on the left, same spectrum with logarithmic axes on the right.

5.3.2 Insulator bell. When an insulator bell was surrounded by a gas which was allowed to undergo plasma reactions, the electric field intensity was measured at a distance of 0.2 m away from the centre line of the bell. The electric field levels at this distance can be seen in Figure 22.

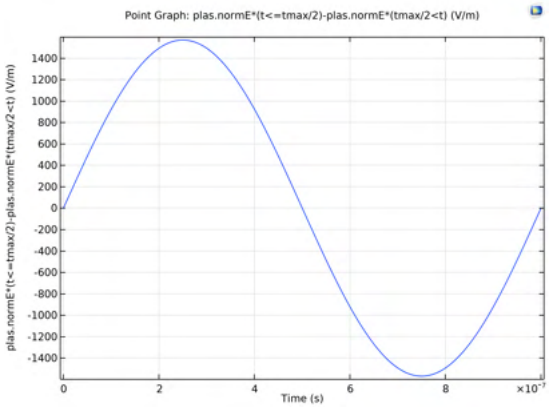

Figure 22: Electric field levels of plasma simulation, 10 kV AC.

If the FFT was applied to the sampled values at the measuring point, the frequency spectra can be seen in Figure 23 was the result.

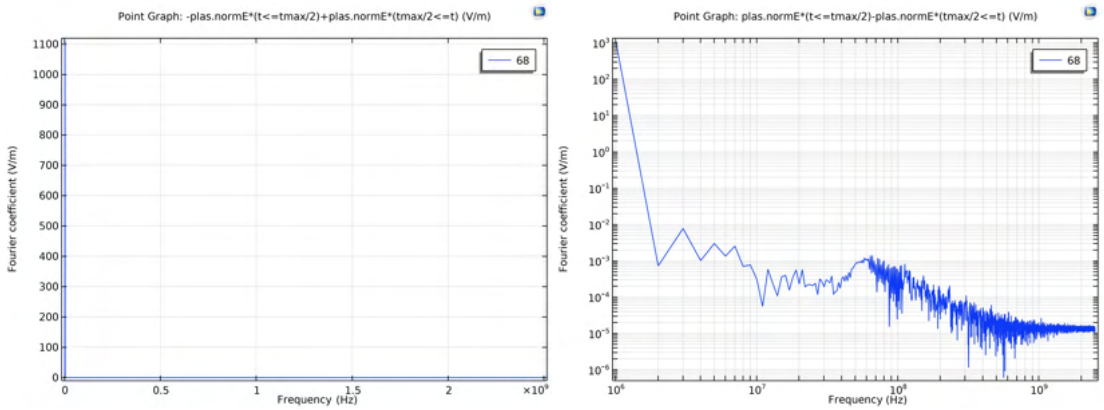

Figure 23: Electric field frequency components, plasma simulation. 10 kV AC. Normal spectrum on the left, same spectrum with logarithmic axes on the right.

5.4 Lab measurements

In this section, the results from the SNR and spectral analysis are presented. The results from the SNR measurements of incoming GNSS signals captured using a phone with an installed GNSS analysis application are first presented, following these results are the measured spectral emissions from each one of the test objects presented under section 4.2.4. These two tests were tested with and without an interfering spark.

5.4.1 SNR measurements with phone application. When the procedures under section 4.1.2 were followed, the following signal-to-noise ratios were measured during test number 1; interference from a spark between two crocodile clips connected to a set of series capacitors were tested. The test object can be seen in Figure 6.

The SNR values measured during the test are shown in Figure 24.

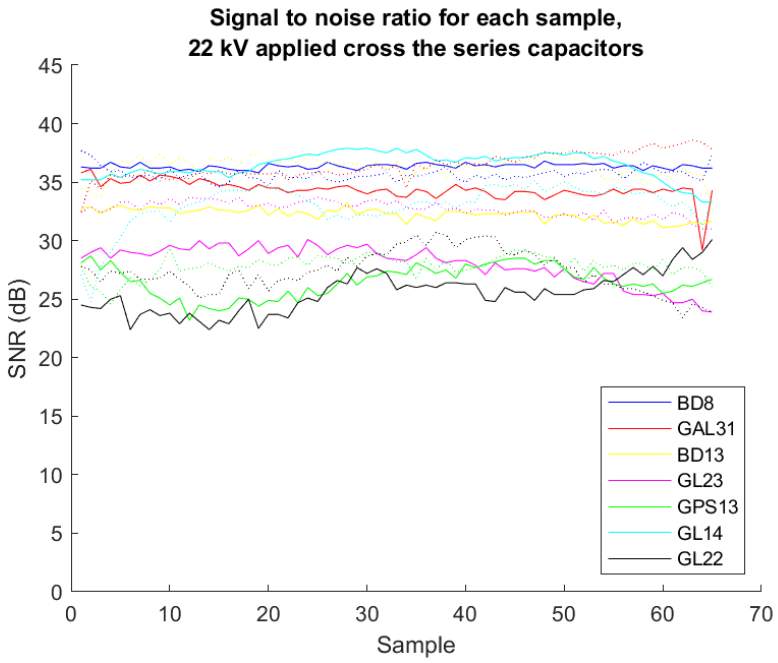

Figure 24: SNR measurements for each respective satellite signal when series capacitors were used as the test object, the different colours are the measured SNR from each respective satellite signal, the dotted lines represents the background values while the solid lines are the recorded SNR values while the interference of the spark was present.

The mean and standard deviations for each satellite signal during test number 1 are shown in Table 12.

Satellite	Background Average (dB)	Background Standard Deviation (dB)	Active Average (dB)	Active Standard Deviation (dB)
BD8	35.7	0.57	36.3	0.22
GAL31	36.4	1.13	34.4	0.85
BD13	36.3	0.92	32.2	0.51
GL23	32.7	0.66	28.0	1.61
GPS13	27.8	0.92	26.5	1.35
GL14	33.0	1.87	36.5	1.12
GL22	27.4	1.78	25.6	1.75

Table 12: Averages and standard deviations for each respective satellite signal during the background and interference measurements when a voltage of 22 kV was applied across the series capacitors.

The overall mean difference between SNR between the background measurement and the measurement with the voltage applied was $\Delta\text{SNR} = -1.4$ dB during the first test.

A second test was performed by following the same procedures as that of test 1, but with another test object. This time an insulator chain, with the bells being separated by a silicone rubber piece was used. The insulator chain can be seen in Figure 7, while the dimensions of the silicone rubber piece can be seen in Figure 8.

The background and interference measurements are shown in Figure 25.

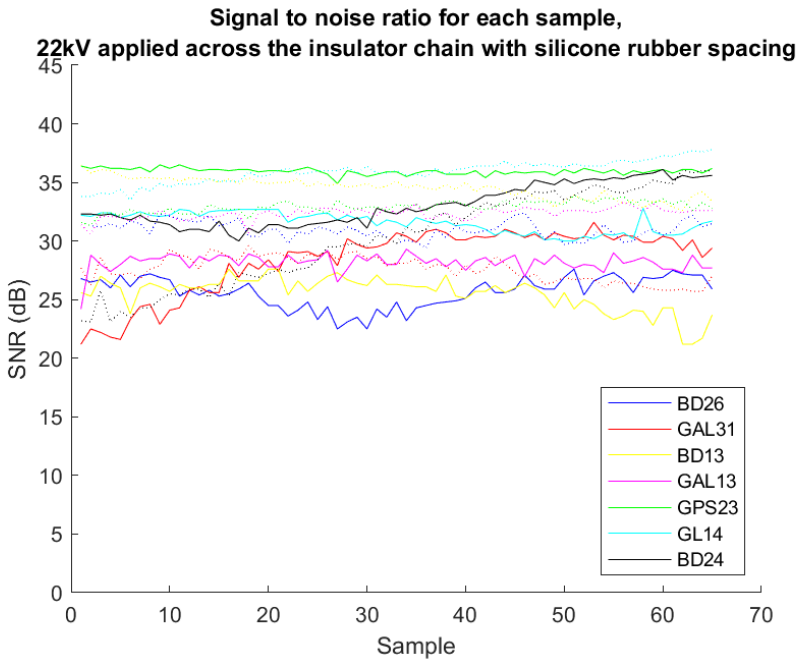

Figure 25: SNR measurements for each respective satellite signal, the different colours are the measured SNR for each respective satellite signal, the dotted lines represents the background values while the solid lines are the recorded SNR values while the interference of the spark was present.

The mean and standard deviations for each respective satellite signal during the background measurements and the measurements with the interfering spark in between two insulator bells are shown in Table 13.

Satellite	Background Average (dB)	Background Standard Deviation (dB)	Active Average (dB)	Active Standard Deviation (dB)
BD26	31.0	0.73	25.6	1.31
GAL31	27.6	1.10	28.4	2.82
BD13	34.5	0.86	25.5	1.43
GAL13	32.3	0.49	28.2	0.74
GPS23	32.9	0.51	36.0	0.27
GL14	35.9	0.99	31.6	0.86
BD24	30.2	4.03	33.0	1.76

Table 13: Averages and standard deviations for each respective satellite signal during the background and interference measurements when a voltage of 22 kV was applied across two insulator bells seperated by a silicone rubber piece.

The overall mean signal-to-noise level difference between the background and the applied voltage measurements of test 2; the test object being two insulator bells was $\Delta\text{SNR} = -2.3$ dB.

5.4.2 Spectral measurements. The testing procedures described under section 4.2.3 were followed, to measure the peak signal levels in a frequency band around the frequencies occupied by GNSS. In Figure 26, the emitted electric fields from a spark generated between the two insulator bells connected into a chain that were separated by a silicone rubber piece was investigated. In this figure, the background levels and the levels with the spark present are shown. The electric field levels in this figure are after the MATLAB processing had been performed, meaning the frequency-dependent amplification of the antenna, according to the antenna's product specification, had been subtracted from the measured values.

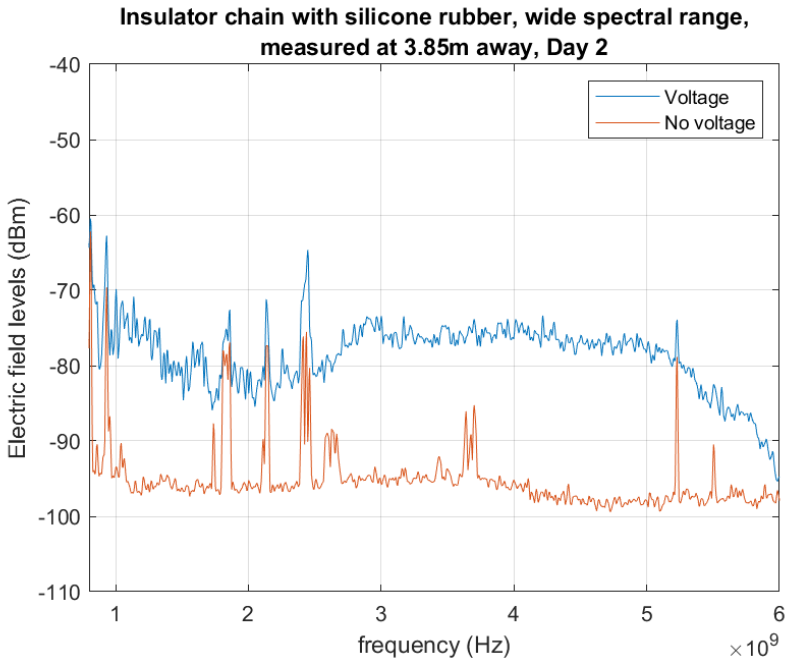

Figure 26: Electric field levels as a function of frequency. The bandwidth used when recording background and when a voltage was applied was 10 kHz.

More figures with different measuring distances, test objects, or antenna orientations are desired, 22 more tests that measure electric field levels from other objects, distances, antenna orientation, or confirmation measurements of already tested scenarios can be found in the appendix under section .4.

6 DISCUSSION

The phenomena that were mainly observed during the calculation stage were that the levels were very similar for the frequencies up until the 200 MHz region. The frequencies above this threshold were observed to drop off linearly when looking at a log-log axes graph. This was observed when using 1, 10 and even 100 accelerating charges. Another observation made was that when increasing the voltage to the applied geometry, the 200 MHz threshold shifted upward or downward in the frequency domain when the voltage was increased or decreased respectively. When the height of the gap was changed, so were the local peak levels. When the gap was smaller compared to the reference dimensions, the peaks became larger, while the peaks decreased in magnitude when the gap between the plates was larger than the reference dimensions.

If the COMSOL simulations are now considered, the most distinct phenomenon that was observed during the simulation stages of the accelerating charge scenarios was that as the height of the gap between the two plates decreased, the radiated electric field peak levels seemed to increase at a greater magnitude compared to if the voltage were increased to reach similar electric field levels experienced in between the two plates but at a greater distance apart. The increased radiated electric field peak levels due to the shorter gap is likely because the measurements were taken in the near field region. When the gap height increases, so will the near field region also do. What happens in the near field region is due to how the radiated fields from all accelerating charges interact with the fields of the other particles. In the near field region, the radiated fields of the charges might add destructively to the other fields at certain points in the geometry, compared to if the electric fields were measured in the far field region where the gap height is very short compared to the distance to the measuring point. In the far field region, the radiated fields will add constructively to one another due to them being in phase with one another. During these simulations, a few more observations were seen, one of these was that in the DC case, the observed peaks occupied a smaller bandwidth compared to AC. In the case of DC voltage, the peaks were very distinct, while taking up a very small part of the measured spectra. But in the case of AC voltage, the peaks were observed to take up larger bandwidths. During the simulations, a shift upward or downwards was observed when the more or fewer charges were included respectively.

The main observation made during the plasma simulations is that there was a peak in the 60 MHz region. Above and below this region the electric field levels decreased. This peak was seen in both simulations of the capacitive model as well as the model made of the insulator bell. This observed peak was slightly more distinguishable in the case of the insulator bell model.

One thing to consider when determining how valid the derived electric field spectra are for the different scenarios covered in this thesis is the phenomenon of aliasing, for example when comparing Figure 19 to Figures 60 and 62. One can see that in the Figure 60 when 3120 distinct electron releases were made in the geometry, had local peak frequencies compared to Figure 62 which have fewer resonant peaks. When the sampling frequency was increased to double the original sampling frequency in the model used to create the spectrum seen in Figure 19, more peaks were observed at higher frequencies. These new peaks were harmonics of the first peak, and they seemed to be repeating up to the peak frequency that could be determined by the amounts of samples used in the model, and if sampling rate was not a limiting factor, these peaks seemed like they would keep repeating for each harmonic that would be covered by the frequency spectra.

The validity of the plasma model can also be questioned, The plasma model that was considered in this paper will only be undergoing 4 different reactions, all of which will result in oxidization or reduction of the nitrogen molecule. This plasma does not contain any other reactions the nitrogen molecule might undergo during an arc, reactions in this category can include but are not limited to nitrogen gas breaking down and creating two individual nitrogen atoms. The plasma model also excludes other molecules present in the air normally. The inclusion of the remaining gases

present in normal air and some or all of their ionization reactions could result in a different electric field spectrum as a result of the discharge phenomenon.

During the two SNR tests performed by using a cellphone with a GNSS tracking and signal analysis application, a small decrease in the SNR could be observed during the two tests performed. But whether the SNR charge is mainly due to the spark being present at the test object is hard to say, since the satellites whose signals are measured are always in motion, their positioning will always be different between the background measurements and the test with the interference source due to the satellite's velocity. This will be something that cannot be kept constant between background and active tests unless two devices were used simultainously, one recording the signals SNR while being interfered by the spark while the other device records the background SNR and at the same time, but is shielded from the spark but not the GNSS signals. This would also require that the two devices being used are recording the same or similar SNR levels while one of the devices are being shielded. This is something that could be tested in future work. The tests performed in this thesis were recorded at two different times due to only having one device to record the SNR with. Other outside parameters will most likely also change. The weather conditions outside are one of these parameters. Although it was clear weather and sunny outside at the time the tests were performed, and the background tests were taken as close as possible in time to the tests with the spark present, this difference in time between the tests could result in slightly changed weather conditions. This change could have an impact on the strength of the received signal, both positive and negative, that could interfere with the tests that were performed.

An important aspect that is common between the SNR tests and the spectral analysis tests is that these measurements were not performed in an anechoic room. The tests were performed in a high-voltage lab, the walls of which were all plated with some kind of painted sheet metal. This will most likely create reflections from the walls which would result in constructive or destructive interference during the measurements. For this reason, during a couple of the tests performed in the spectral measurements section, the effects of rotating the antenna were investigated. When the antenna was rotated 90° away from the insulator chain with a silicone rubber spacer, the measured levels were similar to the background levels for frequencies above 2 GHz. Below 2 GHz, a small increase could be seen in the measured levels. When the antenna was rotated but the insulator bells were separated by insulator tape, a small increase across the entire measured spectra could be observed. Based on these measurements, it is hard to determine the effects that the room will exert on the measured values.

Some measurement anomalies were also detected, one example of which can be seen in Figure 80. The cause of this anomaly is hard to determine since only two of them were recorded, one of these anomalies was recorded during the background test for a measurement while the other was recorded during another measurement but when the voltage was applied.

Another thing to consider is that measurements taken during the spectral measurements of the gap contact in the test objects were taken by holding the max value measured for each bandwidth during the duration of the test. This will result in the worst-case levels being recorded during the background measurements and when the voltage was applied to the test object. But even though the worst case levels were recorded, during day 1, an increase of 5-15 dB could be observed in the recieved signal around the frequencies of GPS, when a measuring bandwidth of 50 kHz was used and a proper spark was created at the test object between the background and test measurements. During day 2 when a bandwidth of 10 kHz was used, an increase of up to 15-25 dB could be observed between the background measurements and the measurements with the voltage applied and a proper spark. These values were lower depending on the means of insulating the bells from each other. If a proper spark was achieved and insulator tape was used to separate the bells, an approximately 7-15 dB increase over the background levels was observed. If the insulator bells failed to be insulated from one another, resulting in no gap, a very small or no change was observed in the measured background and test spectrum, which is to be expected.

With the information from the tests performed, it is and is not so straightforward to determine if a sparking situation could act as an interference source. In "Study of Interference Effects on GPS Signal Acquisition" by Sameet Mangesh Deshpande [20], it is stated that a continuous wave interference (CWI) signal could interfere or jam the acquisition process could be achieved at levels of +10 dB and +15 dB respectively. It was also stated that when a relatively broad-band noise is considered, a +15 dB and a +20-25 dB compared to the desired signal are required to prevent and jam the acquisition process respectively. He also concluded that the power to interfere with the signals all depended on the characteristics of the interference signal. The levels measured in this thesis were observed to reach or even surpass the levels that Deshpande measured [20], with the assumption that the GNSS signals are close to the background levels. However, the frequency spectra measured in this thesis are a result of a CWI source but is a result of the hold max for each measured bandwidth of the spark present at the test object.

When taking the SNR measurements by using a cellphone and an associated signal analysis app, a small decrease in the measured SNR between the background and applied voltage measurements could be observed during the two tests that were performed.

7 CONCLUSION

In this thesis, a capacitive model was considered for most parts of the paper and a plasma simulation was performed on both the capacitive model and on an insulator bell model. Calculations and simulation were performed for charges present between two plates of this capacitive model. If a voltage was applied to one of the plates while having the other one being grounded, the charges would begin to accelerate towards the plate of higher potential. This in turn will result in electromagnetic radiation being emitted from the charges present in between the plates. The electric field levels were measured at a distance away from the electron current stream, and frequency spectra were created using the fast Fourier transform. When doing this, the main observations made were that each resonant peak measured that DC voltage resulted in more distinct peaks compared to AC. The peaks from the AC simulations were taking up a wider bandwidth compared to the peaks from the DC simulations. The inclusion of more charges shifted the peaks in the spectrum upwards while the inclusion of fewer charges shifted the peaks downwards in the frequency spectra. The peaks increased at a greater magnitude when the distance between the electrodes was shorter compared to a greater electrode gap with increased voltages to reach similar electric field levels. This could be seen in both AC and in DC calculations and simulations. In the later parts of the thesis, the same capacitive model and a model of an insulator bell were considered to be surrounded by a gas which could undergo plasma reactions, In this model, the electric fields were measured and a frequency spectrum was calculated for these models as well. In these models, the electric field was also measured, and the FFT were applied to the measured values to determine the spectral emissions from a spark. From the plasma simulations, one small main peak was observed close to 60 MHz.

With these observations and results in mind, the model which would be the closest to representing a normal discharge would be the plasma simulations. Concerning the results from these simulations, the electric fields from these are not affecting the bandwidths occupied by GNSS at a significant level compared to the other frequencies measured. However, to draw a more accurate conclusion, a more advanced model would be required, such as a model which would include the reactions of other particles and provide more reactions for the nitrogen gas.

When a voltage was applied to a series capacitor chain with crocodile clips connected across one of the capacitors, resulting in a spark being generated between the crocodile clips. The SNR was measured at a distance of 4 meters away from the capacitor chain, during the test a decrease of -1.4 dB in the average SNR was observed in the 7 satellites that were tracked during background measurements and measurements with a voltage of 22 kV was applied to the test object. In the second test object was an insulator chain containing two bells, the bells were separated by a piece of silicone rubber. This resulted in a spark occurring between the cap of the lower and the pin of the upper insulator bell. In this test decrease of -2.3 dB in the average SNR was observed between the background measurements and the measurements with a voltage of 22 kV was applied to the chain.

As the last part of this thesis, spectral measurements were taken with the main intent of possible interference originating from a spark occurring at the test object when a voltage was applied across it. When measuring with a bandwidth of 10 kHz, the peak value was recorded. When a spark was present at the test object, the measured electric field levels were up to 25 dB higher compared to the levels observed during the background measurements. When no spacing spacer was used, resulting in proper contact between the two insulator bells used during the measurements, then a voltage was applied across the insulator bells, no noticeable change in the electric field levels was observed.

8 FUTURE WORK

The plasma model can be improved by including more reactions of the nitrogen gas, which would allow nitrogen gas to ionize into two individual nitrogen atoms. It could also be improved by introducing other species, like oxygen, hydrogen, and other elements constituting normal air. The next gas to include would be oxygen gas, which makes up almost 21% of normal air. To implement this, the forward rate for the reactions of oxygen would be required. To take this model even further, the inclusion of reactions between different elements could also be one way to make the plasma model closer to what happens during a sparking situation.

The most appropriate way while being the easiest to implement would be to conduct current testing through the air for up to a desired voltage level, and implement the conductivity of air into a time-dependent study. This could shorten the testing procedure by getting the material characteristics of air in its entirety instead of trying to simulate each reaction that is occurring in the air while an arc is taking place.

Continuation of the measurements performed in this thesis can be done in many different ways. If one wishes to continue the SNR measurements of GNSS signals. If one figures out and constructs a test setup which allows recording of a satellite's background SNR levels and the SNR level with the interference present at the same time, this would remove the impact of the movement of the satellites. This could not be done in this thesis due to two phones of the same model were available, and no setup which allowed for background and interference values to be measured at the same time was constructed. Another solution that could be explored is to implement quicker solutions for switching between the background and interference measurements. The tests conducted in this thesis could also be improved by implementing a solution to record the signals of more satellites, and performing these measurements at other times. If one wishes to do a comparison between the tests performed in this thesis, one has to be careful since there is a potential of other noise sources locally, which could be different at other locations; so it would not be possible to have a strict comparison of "the signal without the HV-gap contribution".

If one is interested in the effects of a spark at frequencies higher than that measured in this thesis, one could extend the frequency ranges measured. The antenna used during these tests extended up to a frequency of 12 GHz, but the measurements were limited to 6 GHz by the spectrum analyzer that was used during the tests. By acquiring a spectrum analyzer which is able to measure higher frequencies, the emissions up to a frequency of 12 GHz could be measured by using a spectrum analyzer more appropriate for said frequencies.

Another measurement that could be performed and would be very useful in determining the potential of interference from a sparking situation could be to record each sweep. By doing this enough times, a mean and standard deviation of the power within a certain bandwidth could be determined. This would result in a better understanding of the characteristics a sparking situation could radiate when it occurs in loose contact or other situations when a spark could occur. It would also be easier to determine the amount of interference a spark can have on a signal within the targeted frequency range.

Another test that could be performed could be one where the materials creating the insulating layer between the insulator chain or other test objects are closer to a situation that could be occurring in an actual power line situation. This could be dirt, debris, the effects of salt which can be a problem when close to the sea, or corrosion. Tests like these would result in a deeper understanding of older equipment to tend to radiate interferences due to said corrosion, or other aging aspects of the equipment in question. This could be valuable since spacing insulator bells by using silicone rubber pieces could be argued to not be very close to a scenario that is encountered in a normal power line setting.

REFERENCES

[1] 2014. Satellite Navigation - GPS - Control Segment. *Federal Aviation Administration* (Nov. 2014). https://www.faa.gov/about/office_org/headquarters_offices/ato/service_units/techops/navservices/gnss/gps/controlsegments

[2] 2019. IEEE Guide on the Prediction,Measurement, and Analysis of AM Broadcast Reradiation by Power Lines. *IEEE Std 1260-2018 (Revision of IEEE Std 1260-1996)* (2019), 1–49. https://doi.org/10.1109/IEEESTD.2019.8649791

[3] 2019. Limits of Human Exposure to Radiofrequency Electromagnetic Energy in the Frequency Range from 3 kHz to 300 GHz. 1, 1 (Aug. 2019). https://www.canada.ca/en/health-canada/services/publications/health-risks-safety/limits-human-exposure-radiofrequency-electromagnetic-energy-range-3-300.html

[4] 2020. How Do Satellites Keep Track Of Their Own Position? *European Space Agency* (2020). https://gssc.esa.int/navipedia/index.php/GPS_Ground_Segment

[5] 2021. Time and Frequency from A to Z, G. *National Institute of Standards and Technology* (March 2021). https://www.nist.gov/pml/time-and-frequency-division/popular-links/time-frequency-z/time-and-frequency-z-g

[6] 2022. Space Segment. (June 2022). https://www.gps.gov/systems/gps/space/

[7] 2023. Gold Code. *Wikipedia* (March 2023). https://en.wikipedia.org/wiki/Gold_code

[8] 2023. GPS signals. *Wikipedia* (March 2023). https://en.wikipedia.org/wiki/GPS_signals

[9] 2023. Satellite Navigation - GPS - Space Segment. *Federal Aviation Administation* (March 2023). https://www.faa.gov/about/office_org/headquarters_offices/ato/service_units/techops/navservices/gnss/gps/spacesegments

[10] 2024. Infrared. 1, 1 (Feb. 2024). https://en.wikipedia.org/wiki/Infrared

[11] 2024. The Issue of Power-Line Noise. *The National Association for Amateur radio* (2024). https://www.arrl.org/power-line-noise

[12] 2024. Nyquist–Shannon sampling theorem. (March 2024). https://en.wikipedia.org/wiki/Nyquist%E2%80%93Shannon_sampling_theorem

[13] 2024. Satellite navigation. 1, 1 (July 2024). https://en.wikipedia.org/wiki/Satellite_navigation

[14] Felipe V. Lopes Amauri G. Martins-Britto, Caio M. Moraes. 2021. Transient electromagnetic interferences between a power line and a pipeline due to a lightning discharge: An EMTP-based approach. *Electric Power Systems Research* 197 (Aug. 2021). https://doi.org/10.1016/j.epsr.2021.107321.

[15] M. G. Backstrom and K. G. Lovstrand. 2004. Susceptibility of electronic systems to high-power microwaves: summary of test experience. *IEEE Transactions on Electromagnetic Compatibility* 46, 3 (2004), 396–403. https://doi.org/10.1109/TEMC.2004.831814

[16] Gérard J M Maystre D Tchelnokov A Bensity H, Berger V. 2005. Photonic Crystals, Towards Nanoscale Photonic Devices. *Springer* 1, 1 (2005). https://link.springer.com/book/10.1007/3-540-27701-3

[17] Tang Bo, Wen Yuanfang, Zhao Zhibin, and Zhang Xiaowu. 2011. Computation Model of the Reradiation Interference Protecting Distance Between Radio Station and UHV Power Lines. *IEEE Transactions on Power Delivery* 26, 2 (2011), 1092–1100. https://doi.org/10.1109/TPWRD.2010.2095043

[18] Jonny Österman Carl Nordling. 2020. Physics handbook for physics and engineering. *Studentlitteratur* 9:1, 9 (Jan. 2020), 220.

[19] V. L. Chartier, R. Sheridan, J. N. DiPlacido, and M. O. Loftness. 1986. Electromagnetic Interference Measurements at 900 MHZ on 230-KV and 500-KV Transmission Lines. *IEEE Transactions on Power Delivery* 1, 2 (1986), 140–149. https://doi.org/10.1109/TPWRD.1986.4307944

[20] Sameet Mangesh Deshpande. 2004. Study of Interference Effects on GPS Signal Acquisition. 1, 1 (July 2004), 187. https://www.ucalgary.ca/engo_webdocs/MEC/04.20199.SMDeshpande.pdf

[21] Petersson E. and Gilbertsson M. 2014. Mätningar för undersökning av kraftledningars påverkan på GPS inom jordbruket. 14:19 (April 2014), 1–26. https://energiforskmedia.blob.core.windows.net/media/21196/matningar-for-undersokning-av-kraftledningars-paverkan-pa-gps-inom-lantbruket-elforskrapport-2014-19.pdf

[22] Kil Gyung-Suk e.t. a.l. 2010. Frequency Spectrum Analysis of Series Arc and Corona Discharges. *Journal of the Korean Institute of Electrical and Electronic Material Engineers* 23, 7 (July 2010), 554–563. https://doi.org/10.4313/JKEM.2010.23.7.554

[23] Li Huang, Bo Tang, Xingfa Liu, and Jianben Liu. 2022. Study on Reradiation Interference Characteristics of Steel Towers in Transmission Lines. *Information* 13, 11 (Oct 2022), 521. https://doi.org/10.3390/info13110521

[24] Liu Jing, Zhao Zhibin, Cui Xiang, and Wang Qi. 2007. Analysis of Passive Interference on Radio Station from UHVDC Power Transmission Lines in Short-wave Frequency. In *2007 International Symposium on Electromagnetic Compatibility*. 71–74. https://doi.org/10.1109/ELMAGC.2007.4413434

[25] Sung-Geon Kim, Euibum Lee, Ic-Pyo Hong, and Jong-Gwan Yook. 2022. Review of Intentional Electromagnetic Interference on UAV Sensor Modules and Experimental Study. *Sensors* 22, 6 (Mar 2022), 2384. https://doi.org/10.3390/s22062384

[26] Michał Kozioł, Łukasz Nagi, Michał Kunicki, and Ireneusz Urbaniec. 2019. Radiation in the Optical and UHF Range Emitted by Partial Discharges. *Energies* 12, 22 (Nov 2019), 4334. https://doi.org/10.3390/en12224334

[27] Roberto Linares y Miranda Luis E. Martínez Santos and Fermín P. Espino-Cortés. 2021. Electromagnetic Spectrum of the Corona Discharge and Their Fundamental Frequency. *Interchopen* (Dec. 2021). https://doi.org/10.5772/intechopen.101550

[28] Ban M. Alameri. 2020. Electromagnetic Interference (EMI) Produced by High Voltage Transmission Lines. *EUREKA: Physics and Engineering* 1, 1 (Sept. 2020), 43–50. https://doi.org/10.21303/2461-4262.2020.001398

[29] Rabah Mostafa and Ahmed El-Hattab. 2011. Investigating the Impact of High Voltage Power Lines on GPS Signal. *Fachbeitrag* 1, 1 (June 2011), 338–343. https://geodaesie.info/images/zfv/136-jahrgang-2011/downloads/zfv_2011_6_Rabah_El-Hattab.pdf

[30] D. Månsson, R. Thottappillil, T. Nilsson, O. Lundén, and M. Bäckström. 2008. Susceptibility of Civilian GPS Receivers to Electromagnetic Radiation. *IEEE Transactions on Electromagnetic Compatibility* 50, 2 (2008), 434–437. https://doi.org/10.1109/TEMC.2008.921015

[31] Nasa. 2016. 10 interesting things about air. 1, 1 (Sept. 2016). https://climate.nasa.gov/news/2491/10-interesting-things-about-air/

[32] Wang Penrose. 2020. Introduction to GNSS II: GPS Signal Processing. *Medium* (Sept. 2020). https://medium.com/@penrosewang/introduction-to-gnss-ii-gps-signal-processing-dd9eae0bdade

[33] J.M. Silva and R.G. Olsen. 2002. Use of Global Positioning System (GPS) receivers under power-line conductors. *IEEE Transactions on Power Delivery* 17, 4 (2002), 938–944. https://doi.org/10.1109/TPWRD.2002.803791

[34] Martin Skriver, Anders Stengaard, Ulrik Pagh Schultz, and Emad Ebeid. 2022. Experimental Investigation of EMC Weaknesses in UAVs During Overhead Power Line Inspection. In *2022 International Conference on Unmanned Aircraft Systems (ICUAS)*. 626–635. https://doi.org/10.1109/ICUAS54217.2022.9836109

[35] Bo Tang, Haotian Jiang, Hongying Cao, Rui Sun, and Ren Liu. 2016. Resonant Frequency Evaluation on Reradiation Interference from Power Transmission Line Based on the Generalized Resonance. *IEEE Transactions on Applied Superconductivity* 26, 7 (2016), 1–5. https://doi.org/10.1109/TASC.2016.2594844

[36] Bo Tang, Haotian Jiang, Hongying Cao, Rui Sun, and Ren Liu. 2016. Resonant Frequency Evaluation on Reradiation Interference from Power Transmission Line Based on the Generalized Resonance. *IEEE Transactions on Applied Superconductivity* 26, 7 (2016), 1–5. https://doi.org/10.1109/TASC.2016.2594844

[37] C. W. Trueman and S. J. Kubina. 1981. Numerical Computation of the Reradiation from Power Lines at MF Frequencies. *IEEE Transactions on Broadcasting* BC-27, 2 (1981), 39–45. https://doi.org/10.1109/TBC.1981.266402

[38] Frank W. Warburton, Tseng-wu Liao, and Norman A. Hoglund. 1969. Power Line Radiations and Interference Above 15 MHz. *IEEE Transactions on Power Apparatus and Systems* PAS-88, 10 (1969), 1492–1501. https://doi.org/10.1109/TPAS.1969.292277

[39] Ira Wiesenfeld. 2021. Tower Shadowing. (Aug. 2021). https://www.braddye.com/tower_shadowing.html

.1 Discrete Fourier transform

In this section, the characteristics of the fourier transform as well as discrete/fast fourier transform will be covered.

.1.1 Fourier transform. Simply put, the fourer transform allows analysis of the different frequencies that would make up a signal. This means that if the function if a signal or function is known, if the fourier transform is applied to the signal in question, the result would be a sum of sine and cosine functions of a certain base frequency and its overtones, as well as a constant in order to replicate the original signal.

.1.2 Discrete/Fast fourier transform. There is one big difference between the normal fourier transform and the discrete/fast fourier transform. While the normal fourier transform requres a known function, the discrete fourier transform can take discrete samples from a signal and determine what frequencies of a cosine function are required in order to make up said signal. The fast fourier transform will do this with the different frequencies of cosine function instead of using both an sine and cosine. This is done by having a complex amplitude multiplier for each one of the harmonics. This complex amplitude will replace the sine part of the normal fourier transform. When the harmonics of the signal have been found, these values then have to be compensated for, due to the characteristics of the fourier transform. Firstly, All frequencies including the constant offset have to be divided by the number of samples, then all harmonics, excluding the offset have to be multiplied with by two in order to get the correct amplitudes for both the costant offset and for all harmonics. One thing to take note of when it comes to the discrete fourier transform, is that due to the symmetry in the x-axis, is that the number of overtones the transform can compute will be equal to the number of samples in the sample signal divided by two.

.2 More calculated scenarios

In this section, more tested scenarios that was not presented in the results section will be presented.

In this test, 10 charges were considered to be accelerating in between the plates. This resulted in the following electric field levels to be recorded at the measuring points.

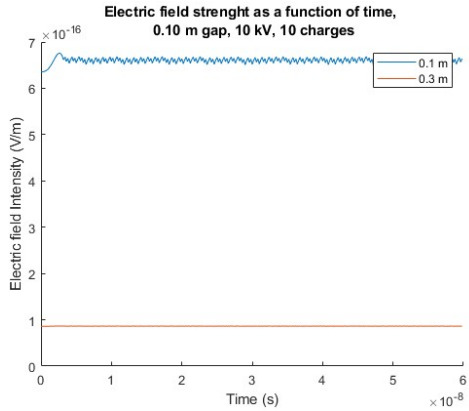

Figure 27: Electric field as a function of time, 10 charges, potential of 10 kV, and 0.1 m between the plates. This figure shows a small part of the measured time, the pattern is repeating up until the end of the sampling period, which is 1 µs.

As before, the fast Fourier transform were applied to the sampled electric field values, this resulted in the following frequency spectra experienced at the measuring points.

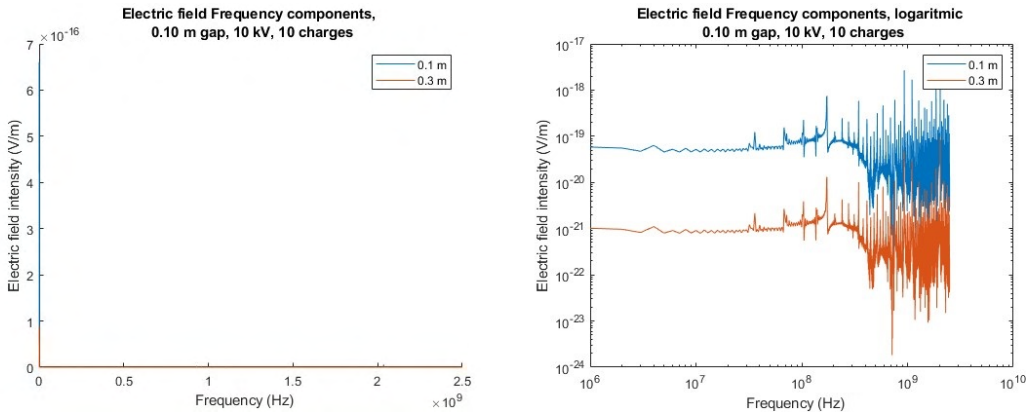

Figure 28: The frequency spectra of the electric field for 1 charge, a potential of 10 kV and a plate gap of 0.1 m. Normal spectra on the left, same spectra but logarithmic axes on the right.

For the last scenario presented here, a total of a 100 charges were considered. This resulted in the electric field levels which can be seen in figure(45).

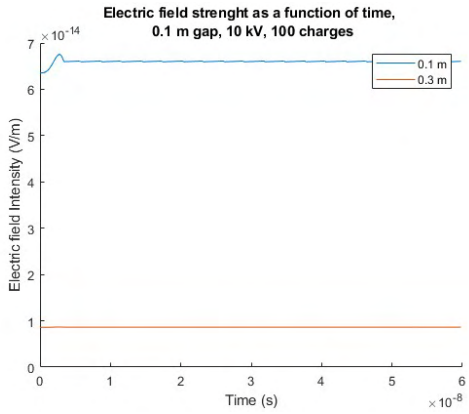

Figure 29: Electric field as a function of time, 100 charges, potential of 10 kV, and 0.1 m between the plates. This figure shows a small part of the measured time, the pattern is repeating up until the end of the sampling period, which is 1 µs.

These electric field levels will correspond to the frequency spectra that can be seen in figure(46).

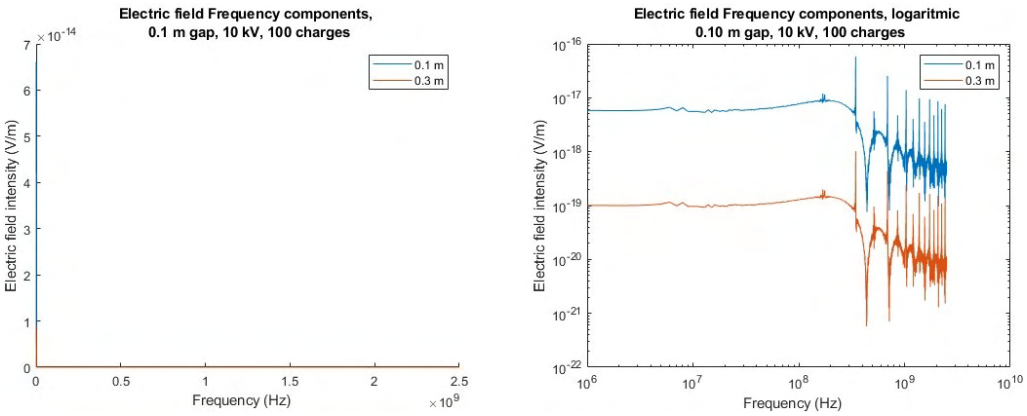

Figure 30: The frequency spectra of the electric field for 1 charge, a potential of 10 kV and a plate gap of 0.1 m. Normal spectra on the left, same spectra but logarithmic axes on the right.

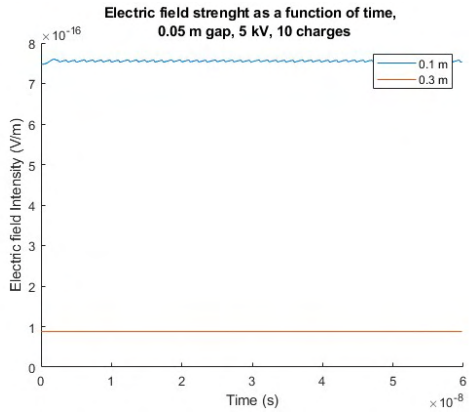

Figure 31: Electric field as a function of time, 10 charges, potential of 5 kV, and 0.05 m between the plates. This figure shows a small part of the measured time, the pattern is repeating up until the end of the sampling period, which is 1 µs.

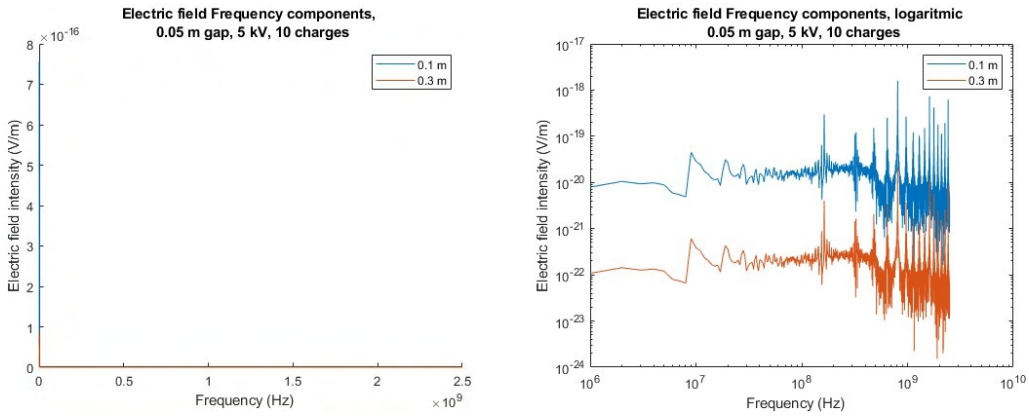

Figure 32: The frequency spectra of the electric field for 10 charge, a potential of 5 kV and a plate gap of 0.05 m. Normal spectra on the left, same spectra but logarithmic axes on the right

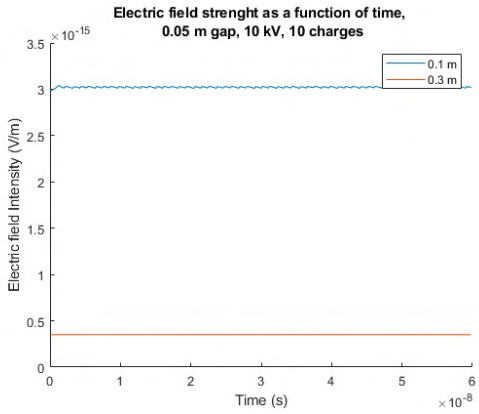

Figure 33: Electric field as a function of time, 10 charges, potential of 10 kV, and 0.05 m between the plates. This figure shows a small part of the measured time, the pattern is repeating up until the end of the sampling period, which is 1 µs.

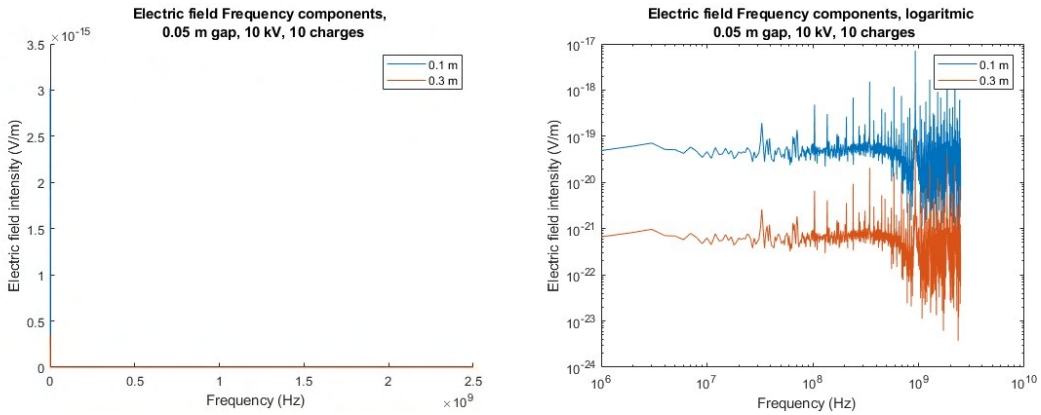

Figure 34: The frequency spectra of the electric field for 10 charge, a potential of 10 kV and a plate gap of 0.05 m. Normal spectra on the left, same spectra but logarithmic axes on the right.

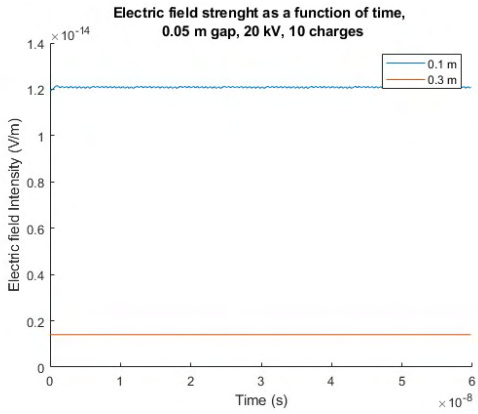

Figure 35: Electric field as a function of time, 10 charges, potential of 20 kV, and 0.05 m between the plates. This figure shows a small part of the measured time, the pattern is repeating up until the end of the sampling period, which is 1 µs.

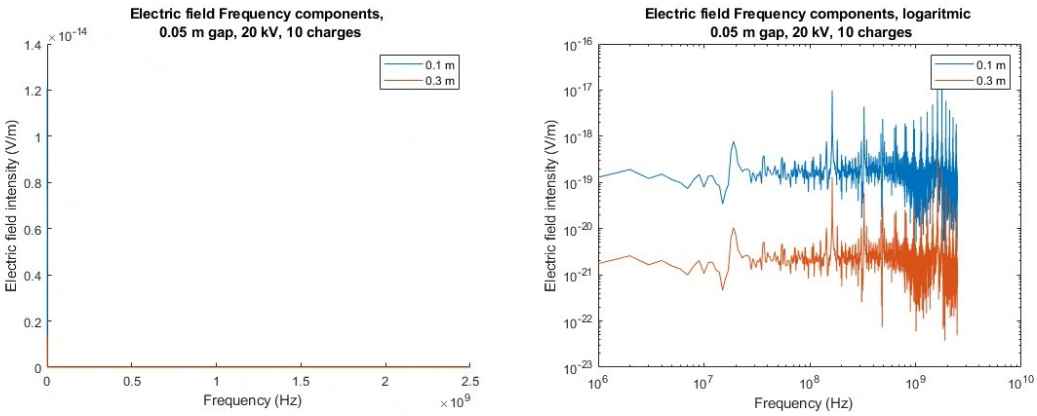

Figure 36: The frequency spectra of the electric field for 10 charge, a potential of 20 kV and a plate gap of 0.05 m. Normal spectra on the left, same spectra but logarithmic axes on the right.

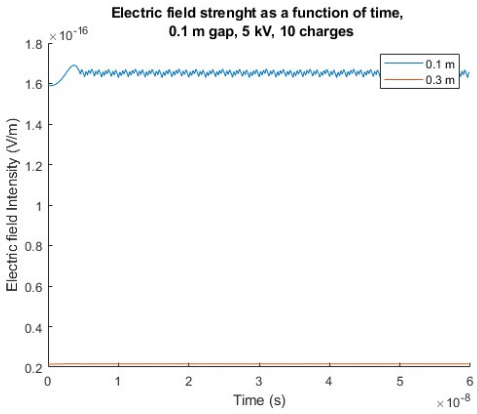

Figure 37: Electric field as a function of time, 10 charges, potential of 5 kV, and 0.1 m between the plates. This figure shows a small part of the measured time, the pattern is repeating up until the end of the sampling period, which is 1 µs.

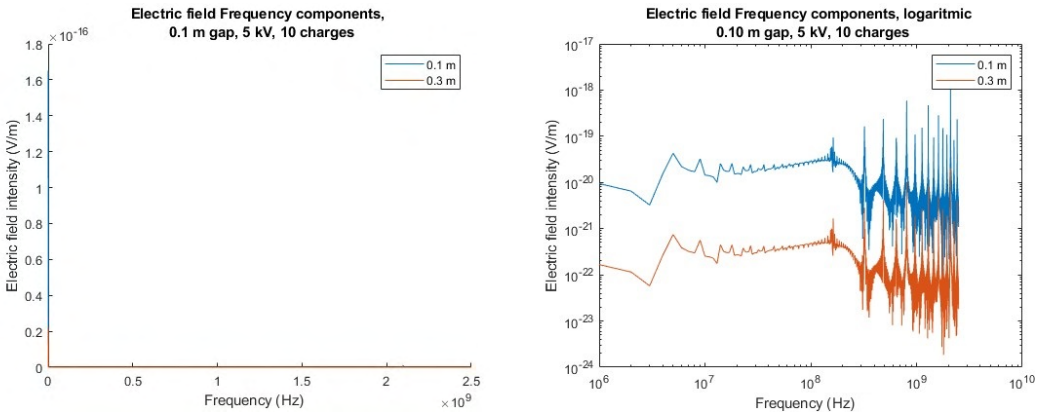

Figure 38: The frequency spectra of the electric field for 10 charge, a potential of 5 kV and a plate gap of 0.1 m. Normal spectra on the left, same spectra but logarithmic axes on the right.

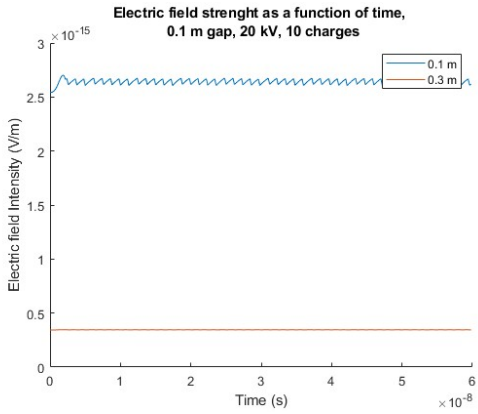

Figure 39: Electric field as a function of time, 10 charges, potential of 20 kV, and 0.1 m between the plates. This figure shows a small part of the measured time, the pattern is repeating up until the end of the sampling period, which is 1 µs.

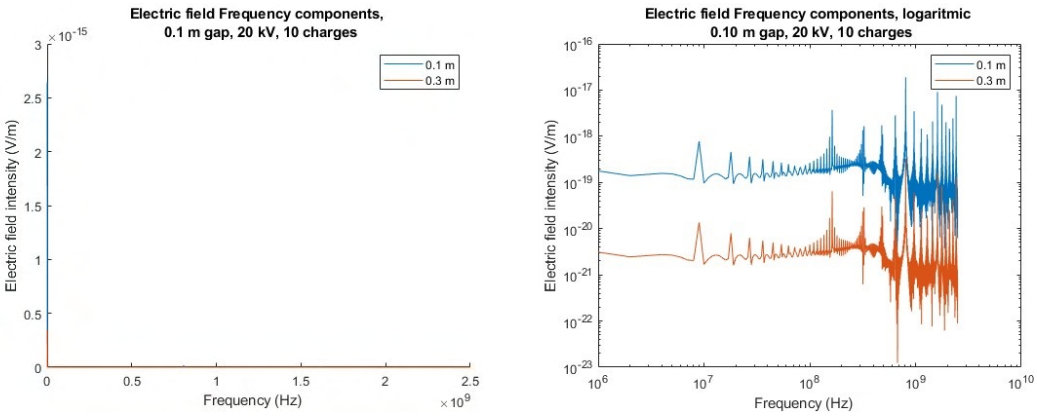

Figure 40: The frequency spectra of the electric field for 10 charge, a potential of 20 kV and a plate gap of 0.1 m. Normal spectra on the left, same spectra but logarithmic axes on the right.

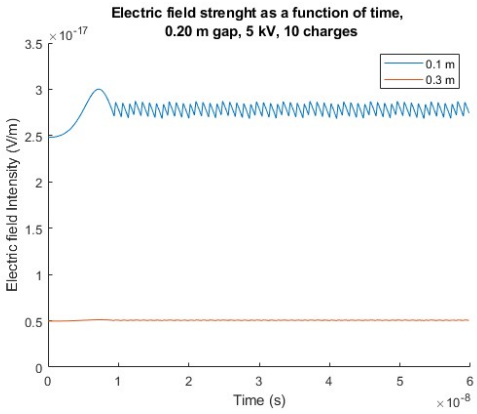

Figure 41: Electric field as a function of time, 10 charges, potential of 5 kV, and 0.2 m between the plates. This figure shows a small part of the measured time, the pattern is repeating up until the end of the sampling period, which is 1 µs.

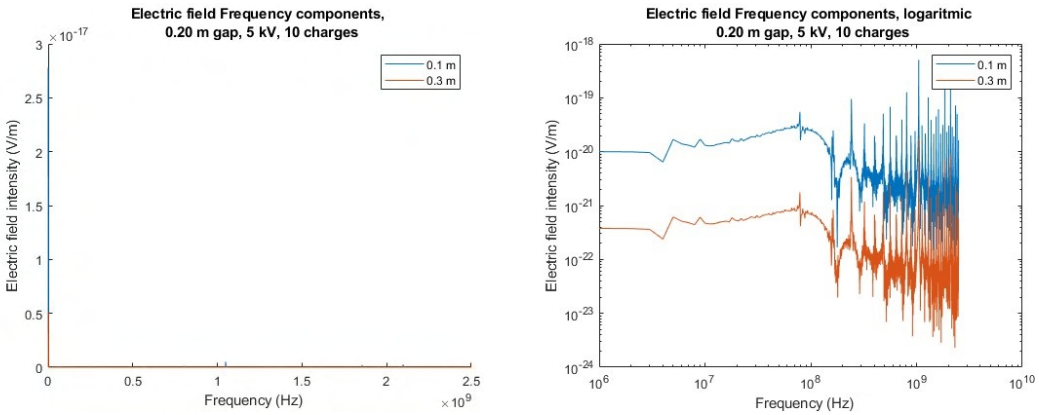

Figure 42: The frequency spectra of the electric field for 10 charge, a potential of 5 kV and a plate gap of 0.2 m. Normal spectra on the left, same spectra but logarithmic axes on the right.

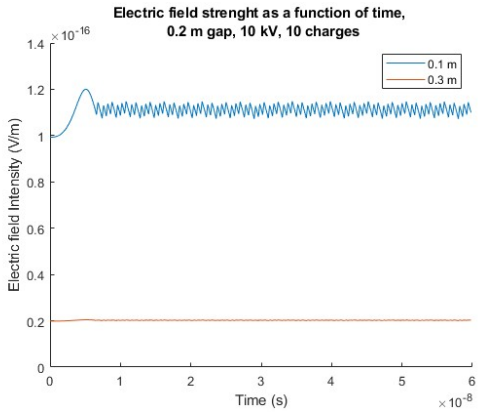

Figure 43: Electric field as a function of time, 10 charges, potential of 10 kV, and 0.2 m between the plates. This figure shows a small part of the measured time, the pattern is repeating up until the end of the sampling period, which is 1 µs.

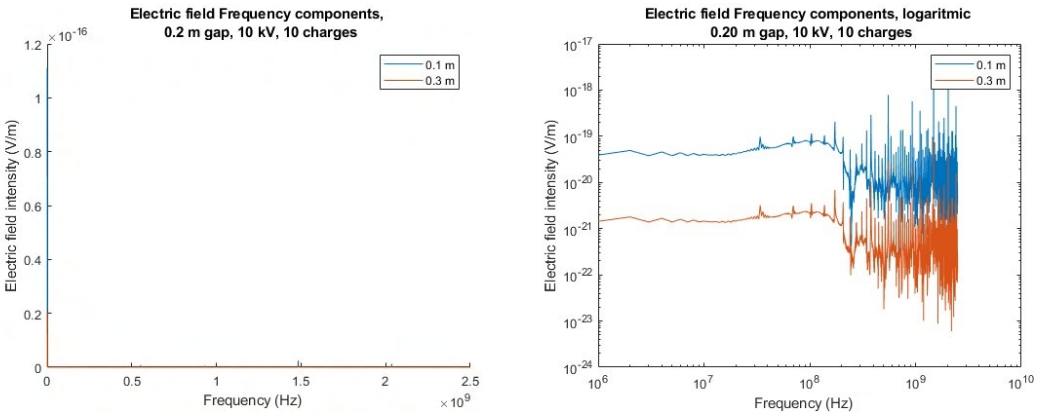

Figure 44: The frequency spectra of the electric field for 10 charge, a potential of 10 kV and a plate gap of 0.2 m. Normal spectra on the left, same spectra but logarithmic axes on the right.

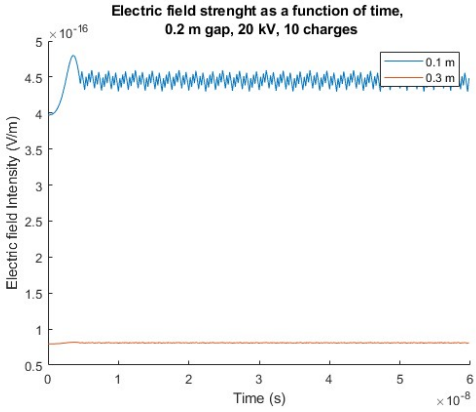

Figure 45: Electric field as a function of time, 10 charges, potential of 20 kV, and 0.2 m between the plates. This figure shows a small part of the measured time, the pattern is repeating up until the end of the sampling period, which is 1 µs.

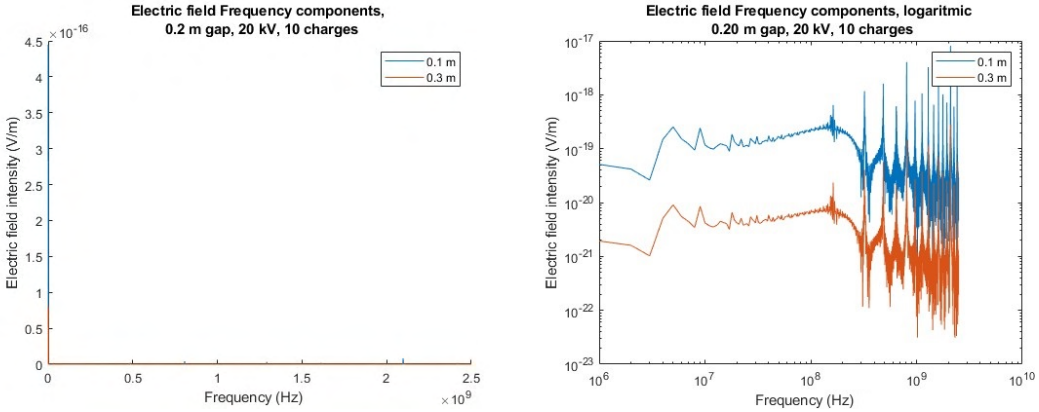

Figure 46: The frequency spectra of the electric field for 10 charge, a potential of 20 kV and a plate gap of 0.2 m. Normal spectra on the left, same spectra but logarithmic axes on the right.

.3 Other COMSOL scenarios

.3.1 More COMSOL figures. In these section, more scenarions with different model parameters other than the ones that were presented in the results section can be found. This include voltage levels, gap distances, distinct electron releases, or DC or AC voltage sources.

.3.2 DC simulations. In this section, more DC simulations are presented that was not presented in the results section.

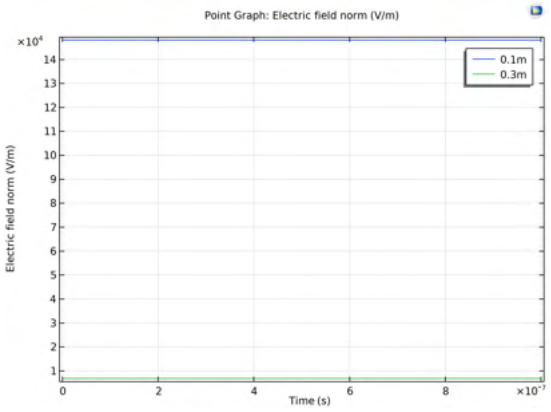

Figure 47: Electric field, 10 kV DC, 0.1 m gap, 3120 distinct releases of electrons.

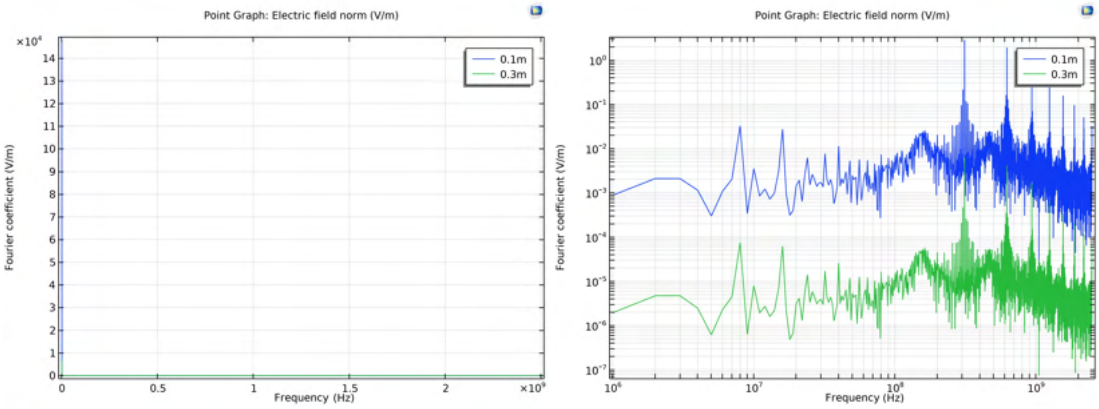

Figure 48: Electric field frequency components, 10 kV DC, 0.1 m gap, 3120 distinct releases of electrons. Normal spectra on the left, same spectra but logarithmic axes on the right.

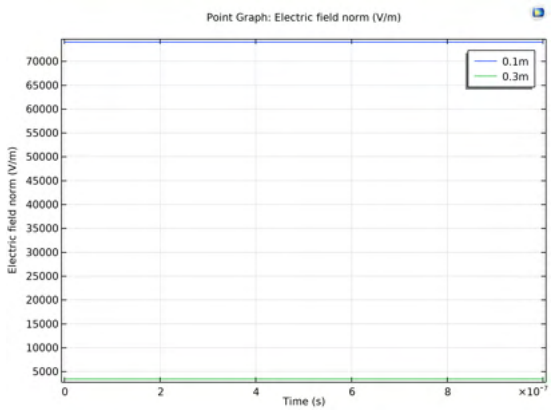

Figure 49: Electric field, 10 kV DC, 0.1 m gap, 12480 distinct releases of electrons.

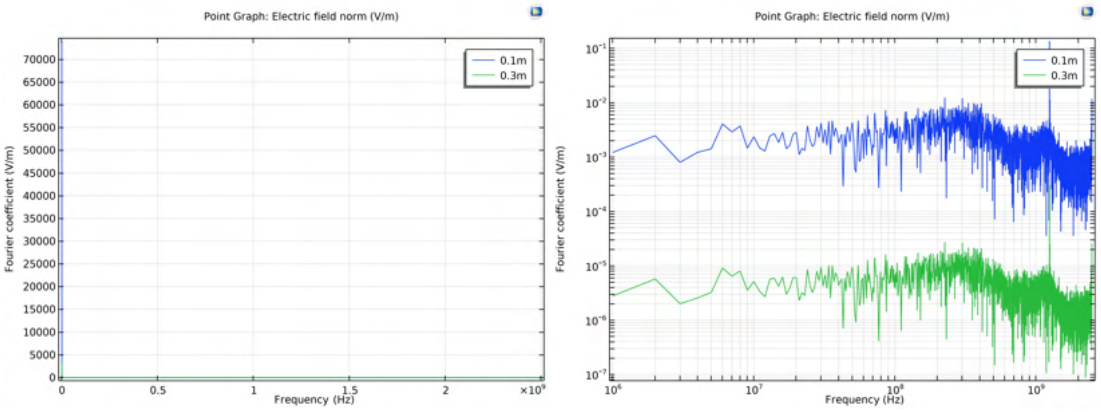

Figure 50: Electric field frequency components, 10 kV DC, 0.1 m gap, 12480 distinct releases of electrons. Normal spectra on the left, same spectra but logarithmic axes on the right.

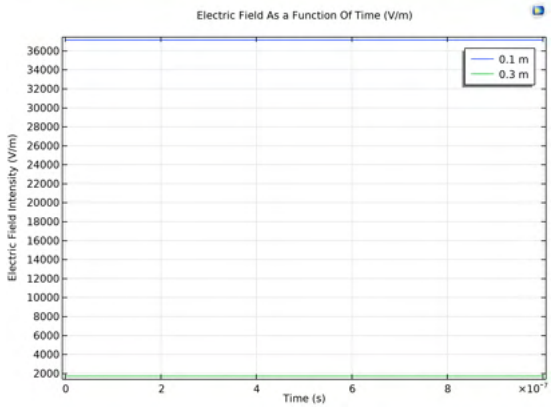

Figure 51: Electric field, 5 kV DC, 0.1 m gap, 6240 distinct releases of electrons.

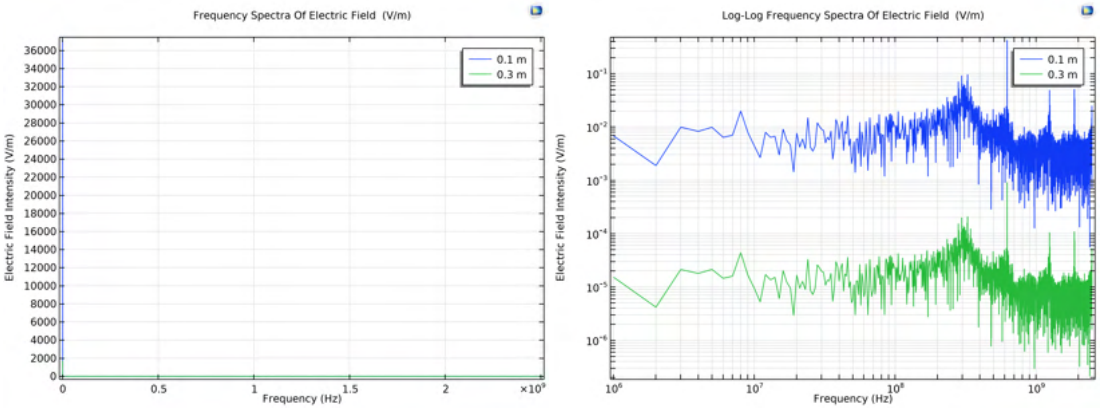

Figure 52: Electric field frequency components, 5 kV DC, 0.1 m gap, 6240 distinct releases of electrons. Normal spectra on the left, same spectra but logarithmic axes on the right.

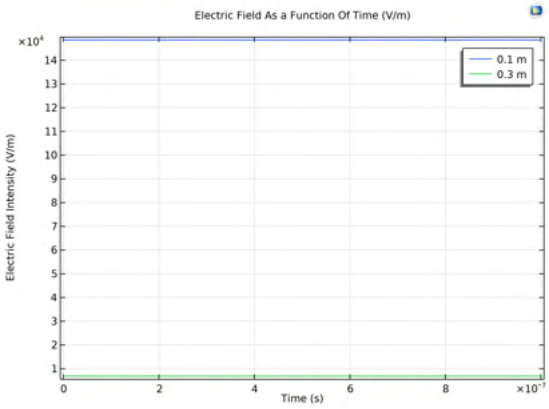

Figure 53: Electric field, 20 kV DC, 0.1 m gap, 6240 distinct releases of electrons.

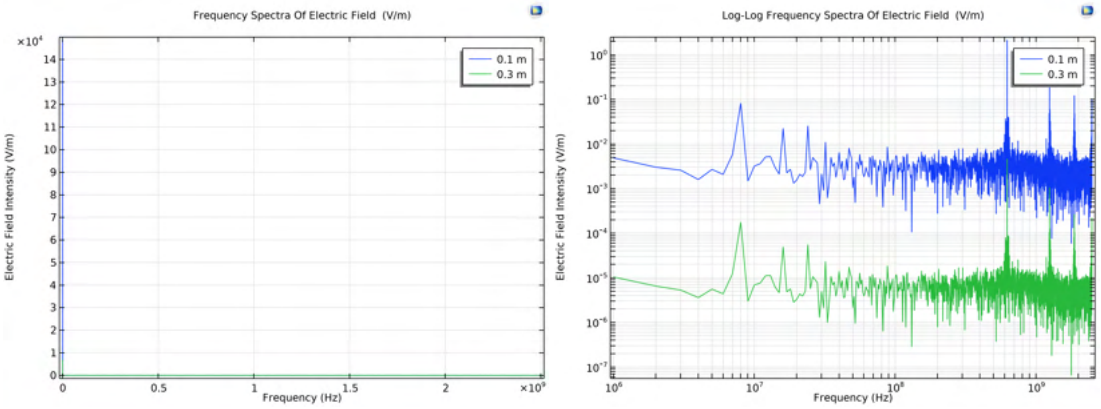

Figure 54: Electric field frequency components, 20 kV DC, 0.1 m gap, 6240 distinct releases of electrons. Normal spectra on the left, same spectra but logarithmic axes on the right.

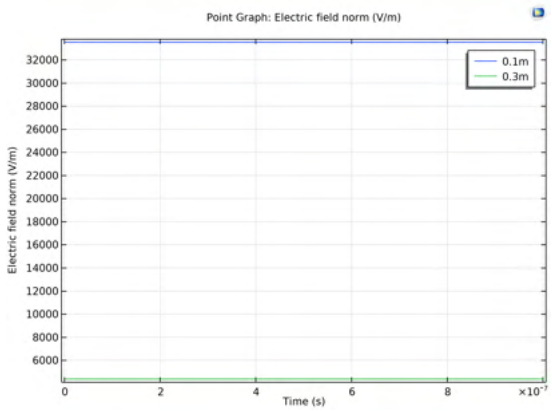

Figure 55: Electric field, 5 kV DC, 0.2 m gap, 6240 distinct releases of electrons.

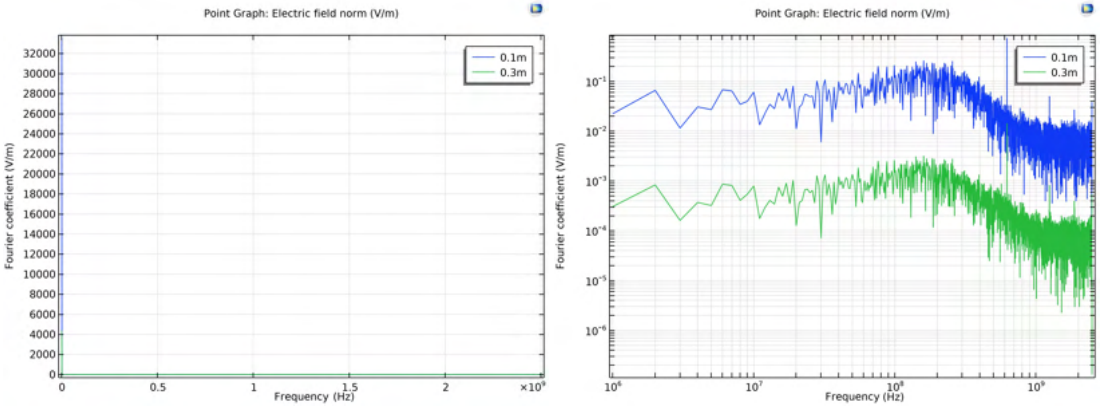

Figure 56: Electric field frequency components, 10 kV DC, 0.2 m gap, 6240 distinct releases of electrons. Normal spectra on the left, same spectra but logarithmic axes on the right.

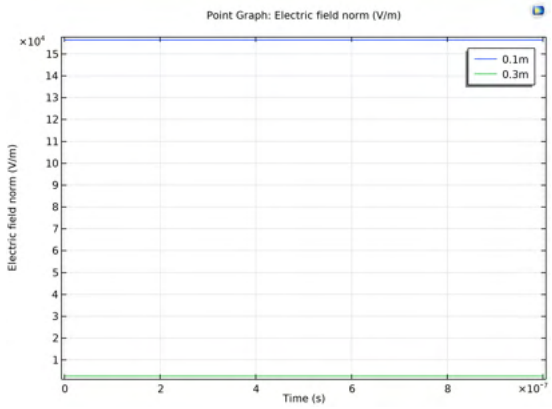

Figure 57: Electric field, 10 kV DC, 0.05 m gap, 6240 distinct releases of electrons.

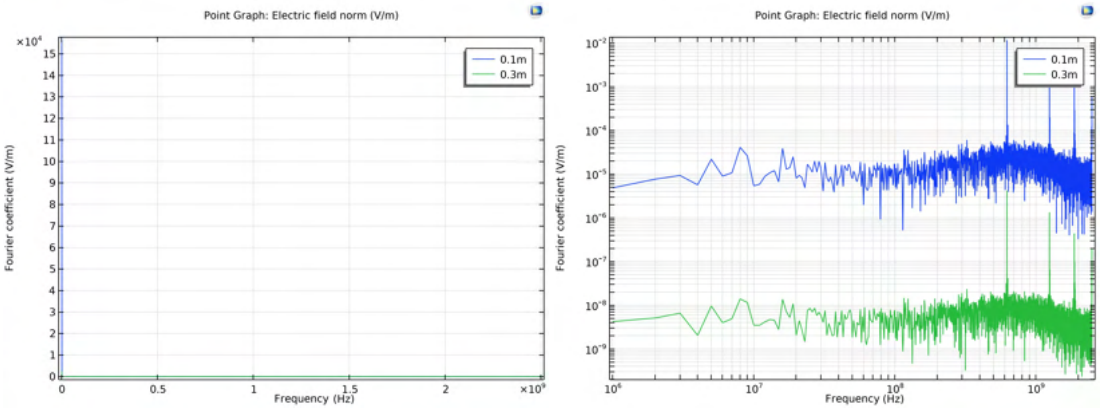

Figure 58: Electric field frequency components, 10 kV DC, 0.05 m gap, 6240 distinct releases of electrons. Normal spectra on the left, same spectra but logarithmic axes on the right.

.3.3 AC simulations. In this section, more AC senarios are presented, scenarios with different voltage levels, frequencies, releases, and gap distances that was not presented in the results section.

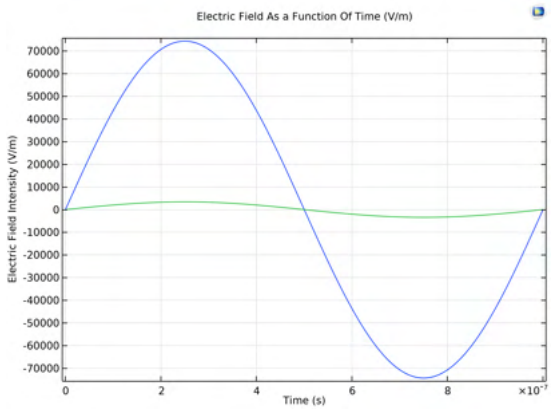

Figure 59: Electric field, 10 kV AC, 0.05 m gap, 3120 distinct releases of electrons.

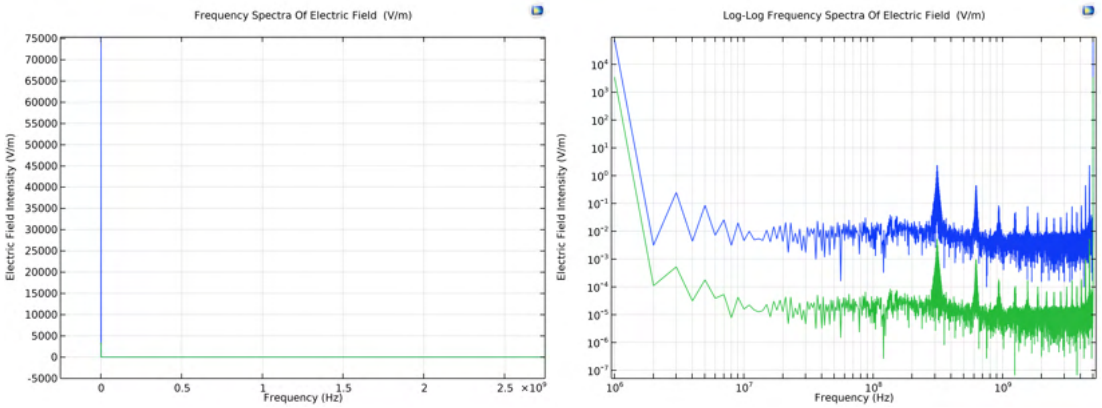

Figure 60: Electric field frequency components, 10 kV AC, 0.05 m gap, 3120 distinct releases of electrons. Normal spectra on the left, same spectra but logarithmic axes on the right.

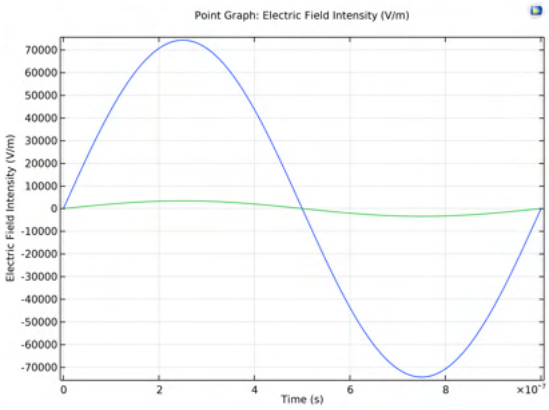

Figure 61: Electric field, 10 kV AC, 0.05 m gap, 12480 distinct releases of electrons.

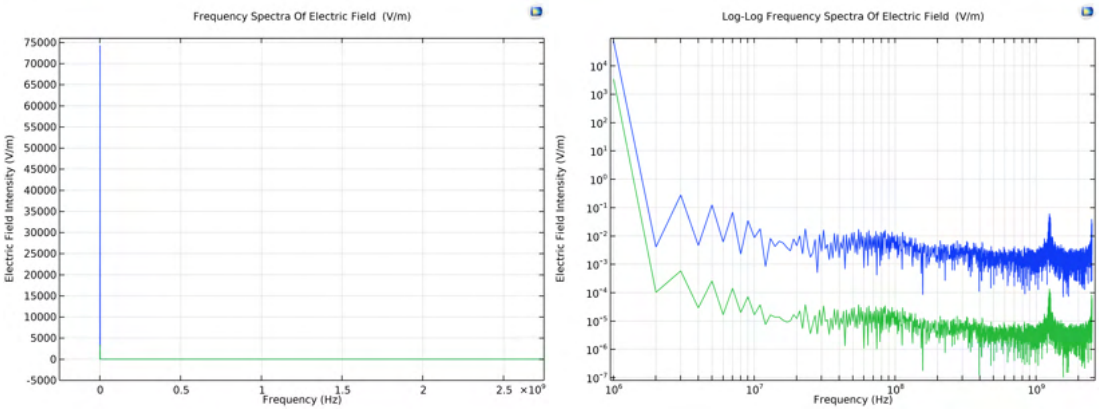

Figure 62: Electric field frequency components, 10 kV AC, 0.05 m gap, 12480 distinct releases of electrons. Normal spectra on the left, same spectra but logarithmic axes on the right.

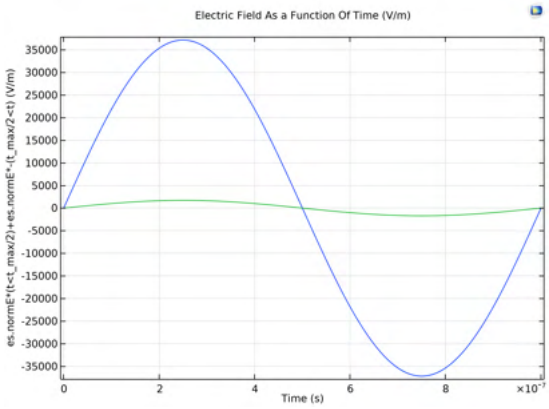

Figure 63: Electric field, 5 kV, 0.1 m gap, 6240 distinct releases of electrons.

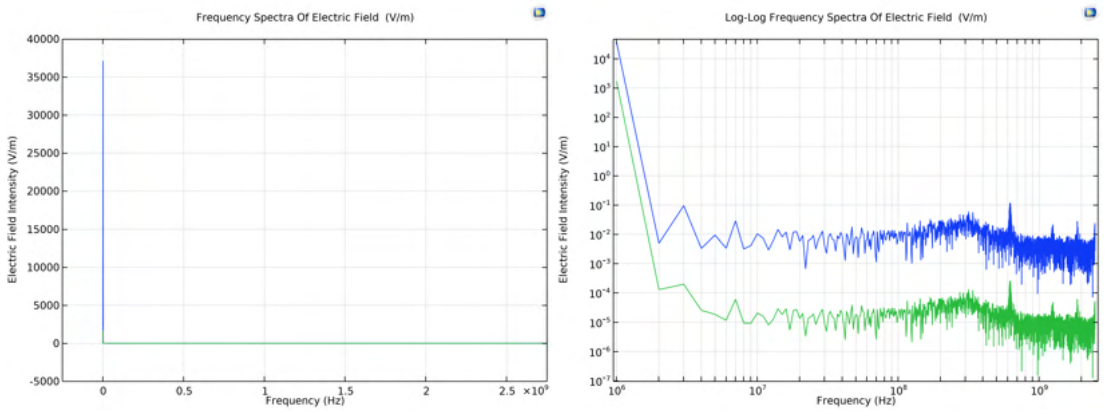

Figure 64: Electric field frequency components, 5 kV, 0.1 m gap, 6240 distinct releases of electrons. Normal spectra on the left, same spectra but logarithmic axes on the right.

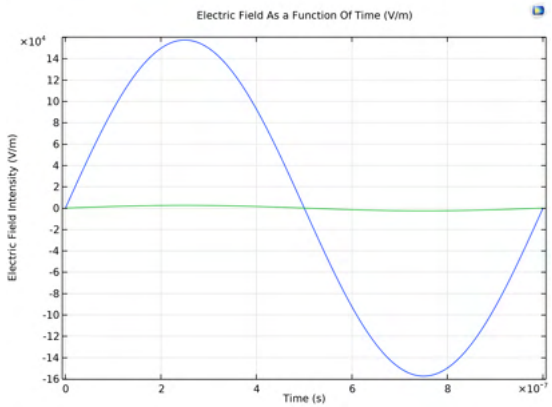

Figure 65: Electric field, 10 kV, 0.1 m gap, increased base frequency to 2 MHz, 6240 distinct releases of electrons.

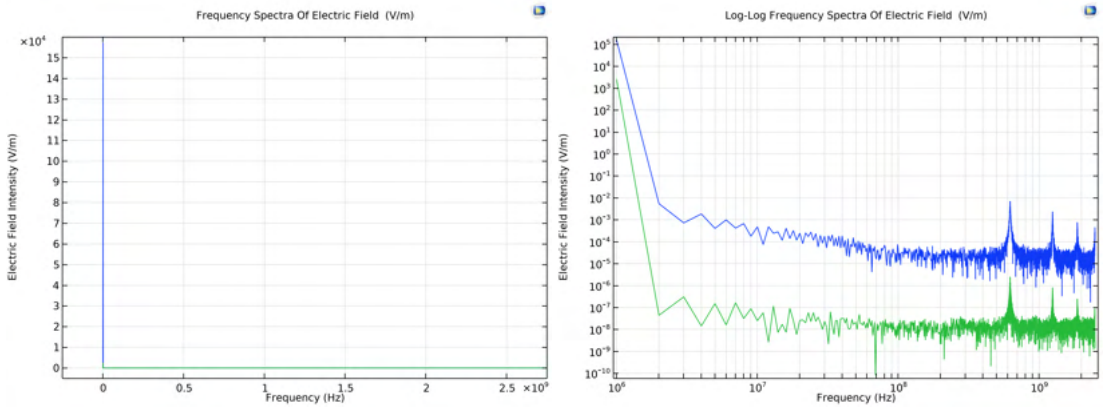

Figure 66: Electric field frequency components, increased base frequency to 2 MHz, 10 kV, 0.1 m gap, 6240 distinct releases of electrons. Normal spectra on the left, same spectra but logarithmic axes on the right.

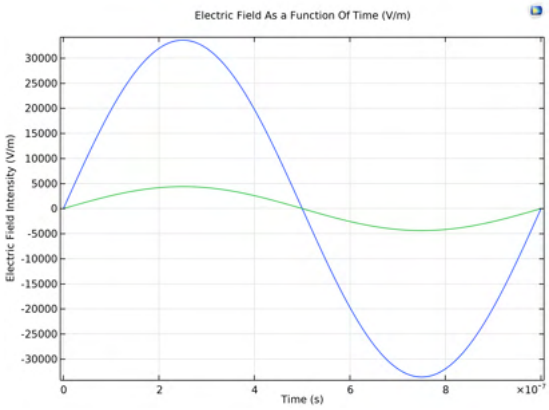

Figure 67: Electric field, 10 kV, 0.2 m gap, 6240 distinct releases of electrons.

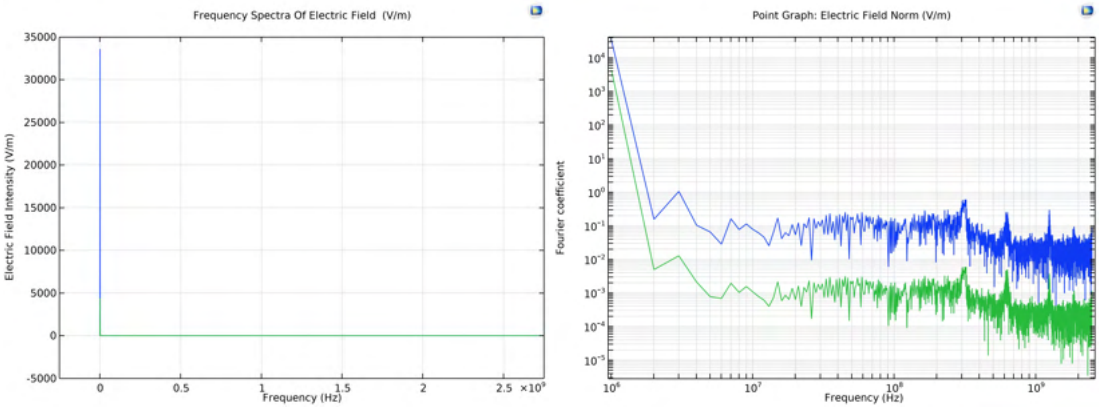

Figure 68: Electric field frequency components, 10 kV, 0.2 m gap, 6240 distinct releases of electrons. Normal spectra on the left, same spectra but logarithmic axes on the right.

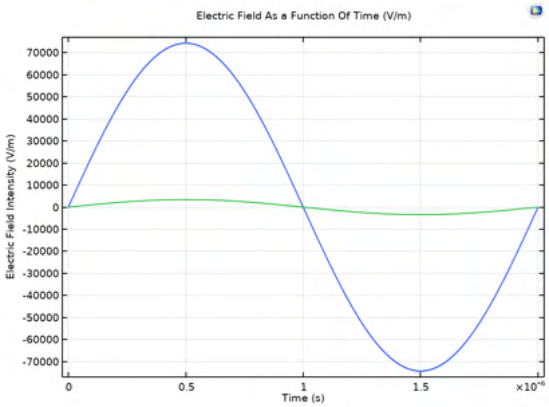

Figure 69: Electric field, 10 kV, 0.1 m gap, decreased base frequency to 500 kHz, 12480 distinct releases of electrons.

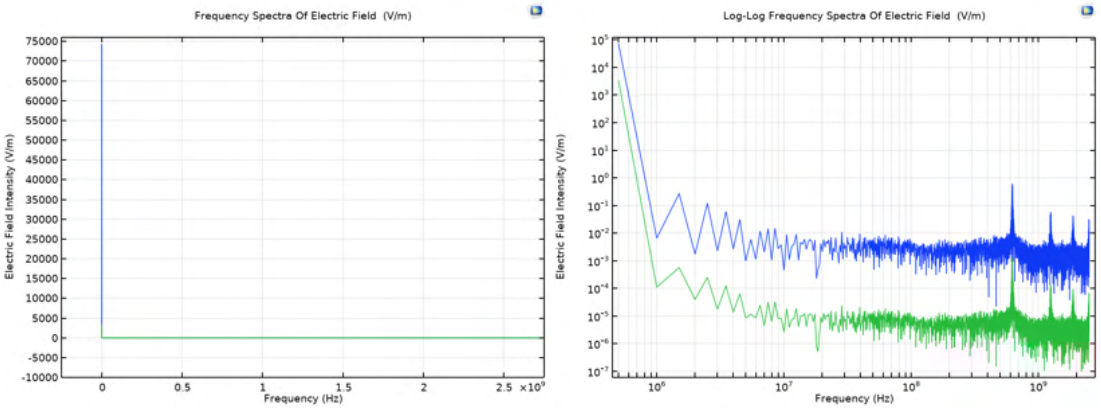

Figure 70: Electric field frequency components, decreased base frequency to 500 kHz, 10 kV, 0.1 m gap, 12480 distinct releases of electrons. Normal spectra on the left, same spectra but logarithmic axes on the right.

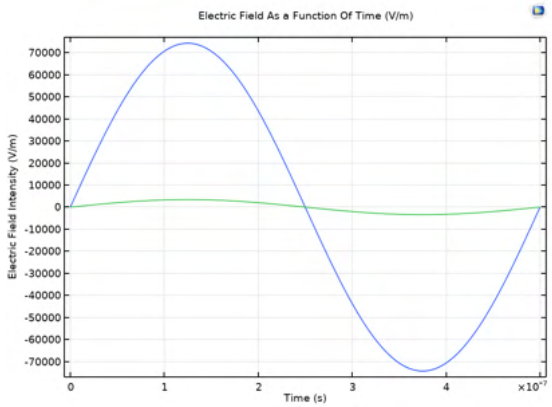

Figure 71: Electric field, 10 kV, 0.1 m gap, increased base frequency to 2 MHz, 6240 distinct releases of electrons.

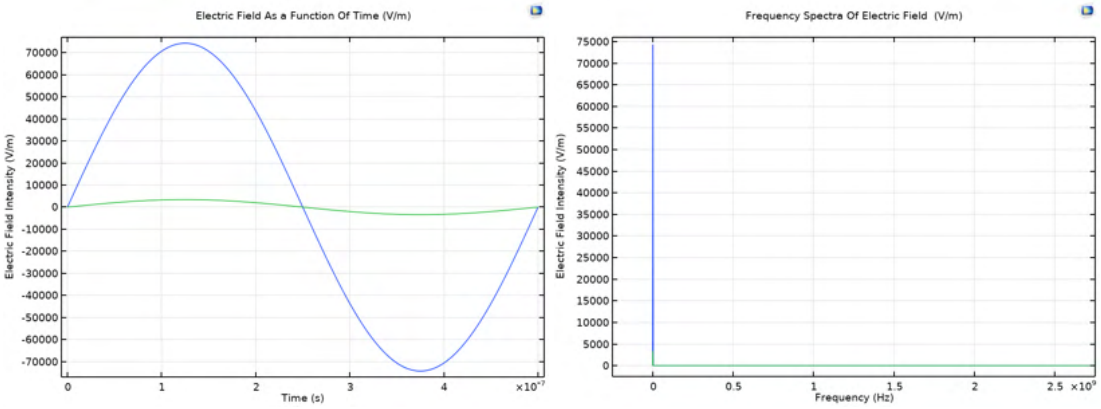

Figure 72: Electric field frequency components, increased base frequency to 2 MHz, 10 kV, 0.1 m gap, 6240 distinct releases of electrons. Normal spectra on the left, same spectra but logarithmic axes on the right.

.4 More lab test setups

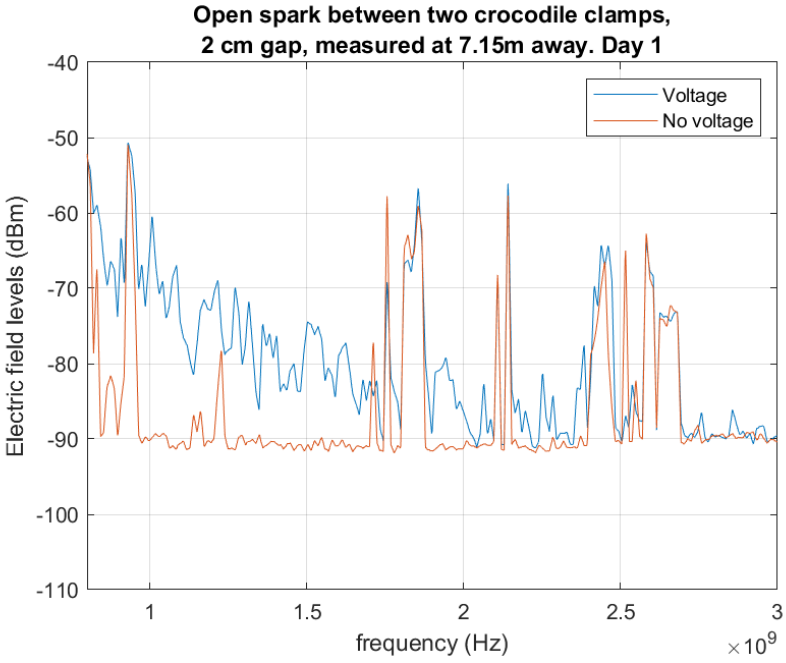

Figure 73: Electric field as a function of frequency. Bandwidth used when recording background levels and levels with the applied voltage was 50 kHz.

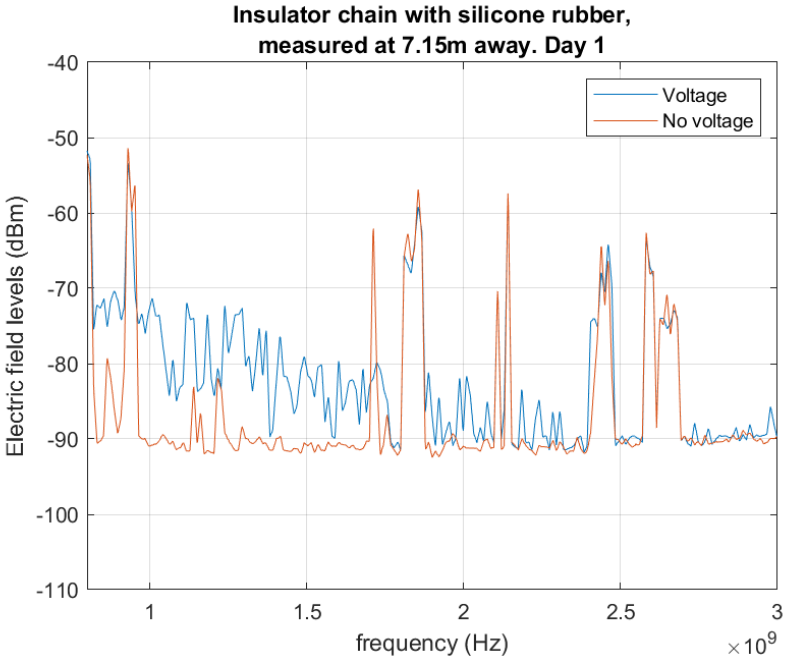

Figure 74: Electric field as a function of frequency. Bandwidth used when recording background levels and levels with the applied voltage was 50 kHz.

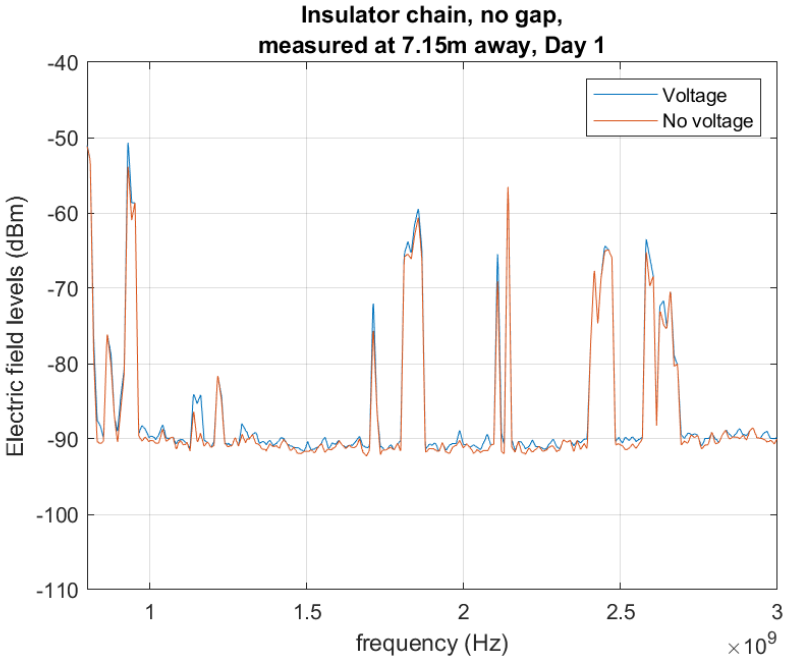

Figure 75: Electric field as a function of frequency. Bandwidth used when recording background levels and levels with the applied voltage was 50 kHz.

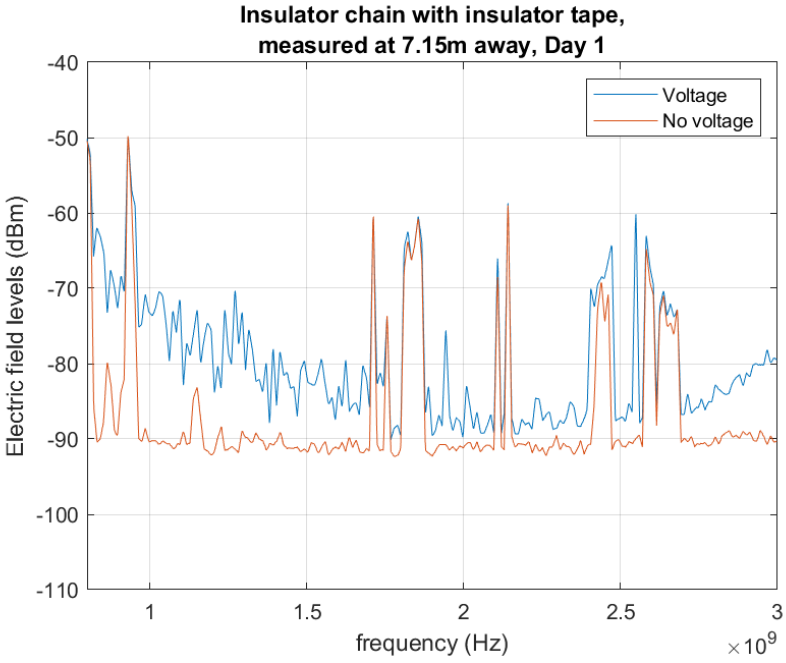

Figure 76: Electric field as a function of frequency. Bandwidth used when recording background levels and levels with the applied voltage was 50 kHz.

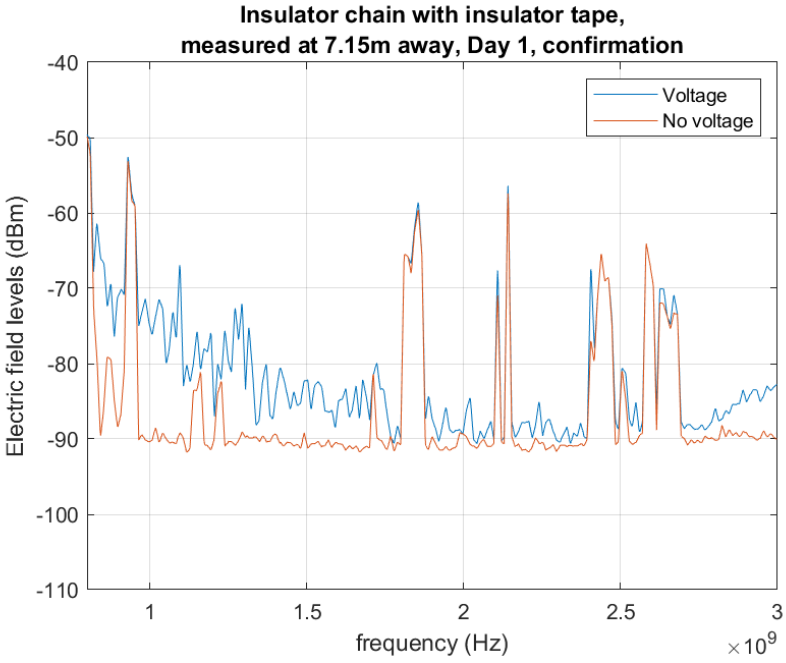

Figure 77: Electric field as a function of frequency. Bandwidth used when recording background levels and levels with the applied voltage was 50 kHz.

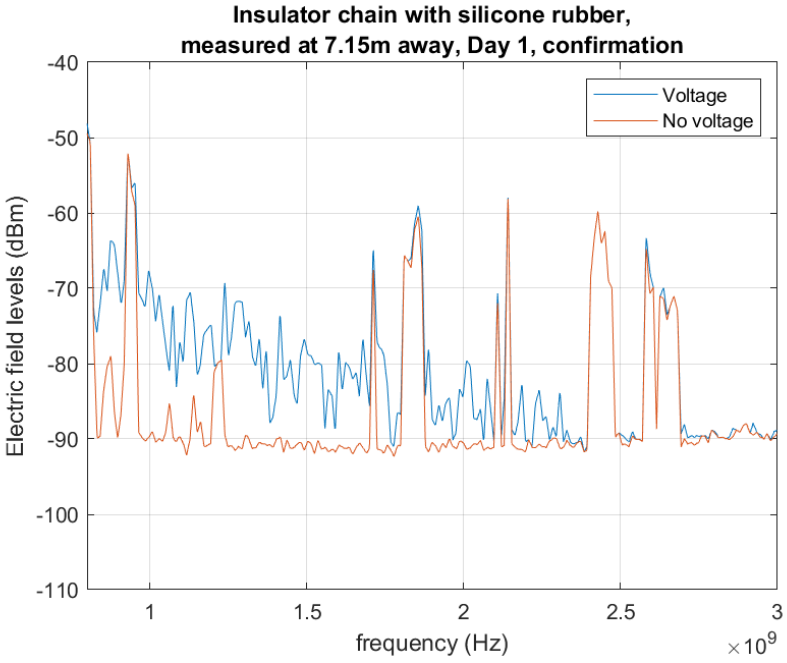

Figure 78: Electric field as a function of frequency. Bandwidth used when recording background levels and levels with the applied voltage was 50 kHz.

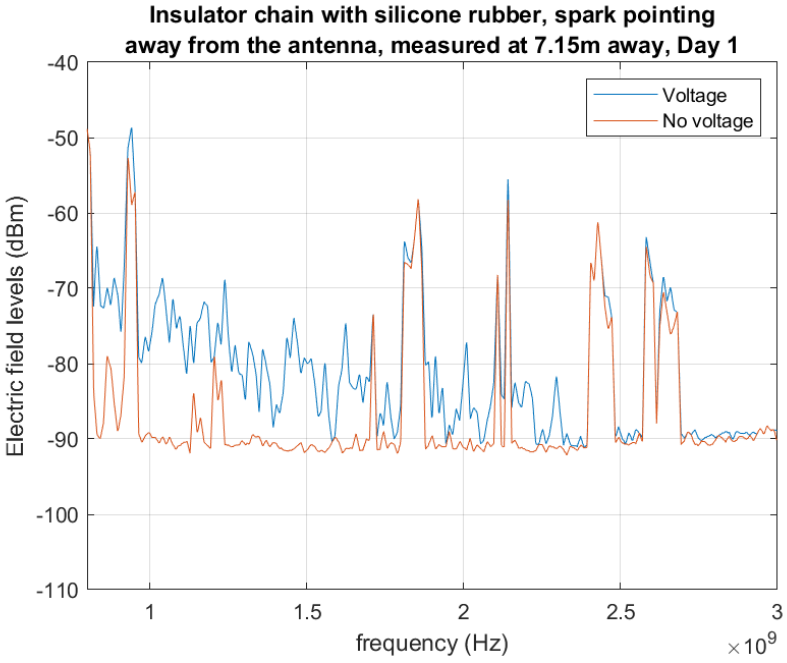

Figure 79: Electric field as a function of frequency. Bandwidth used when recording background levels and levels with the applied voltage was 50 kHz.

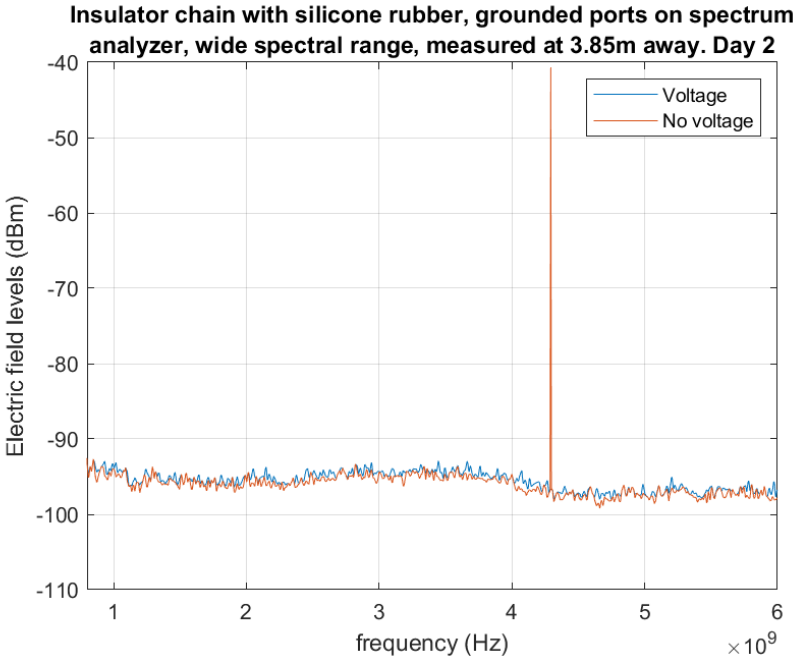

Figure 80: Electric field as a function of frequency. Bandwidth used when recording background levels and levels with the applied voltage was 10 kHz.

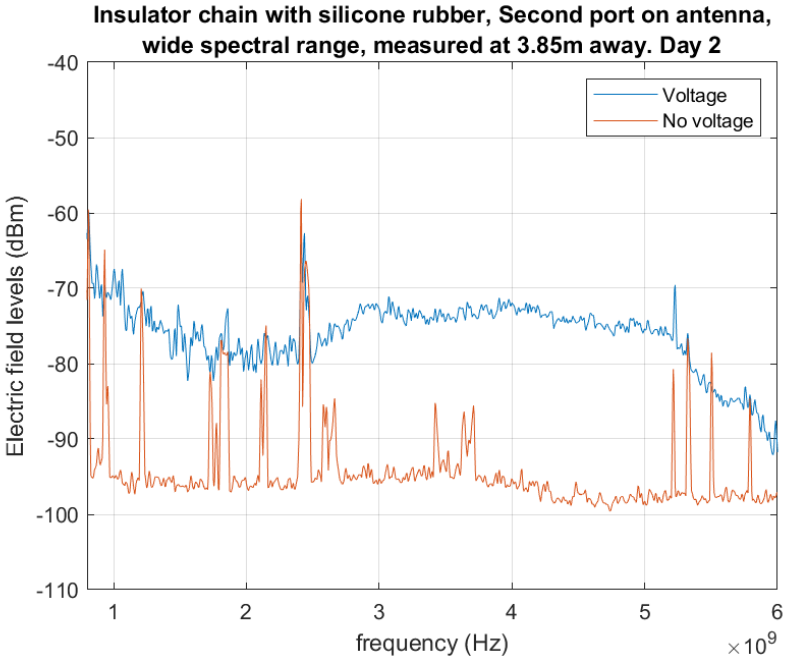

Figure 81: Electric field as a function of frequency. Bandwidth used when recording background levels and levels with the applied voltage was 10 kHz.

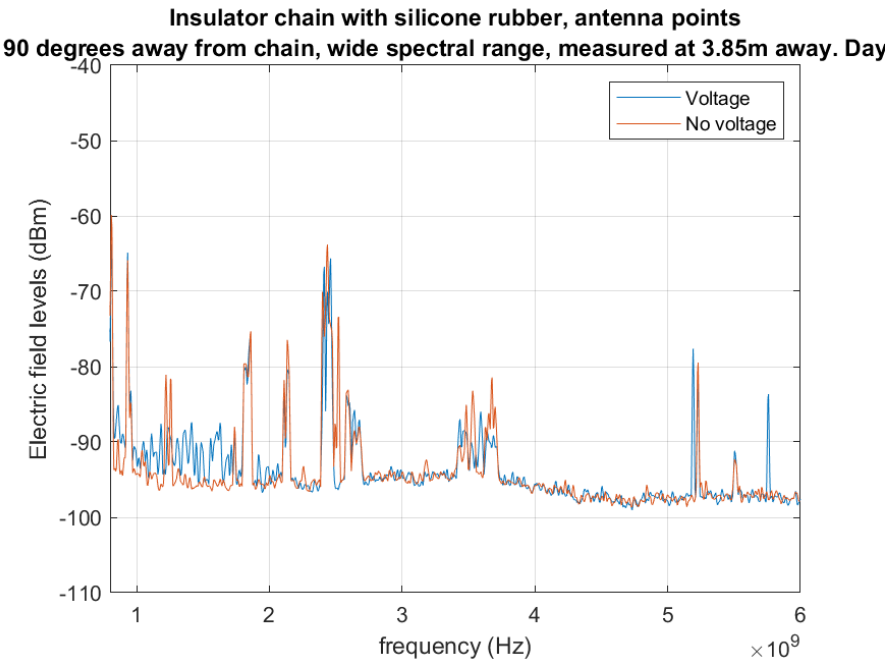

Figure 82: Electric field as a function of frequency. Bandwidth used when recording background levels and levels with the applied voltage was 10 kHz.

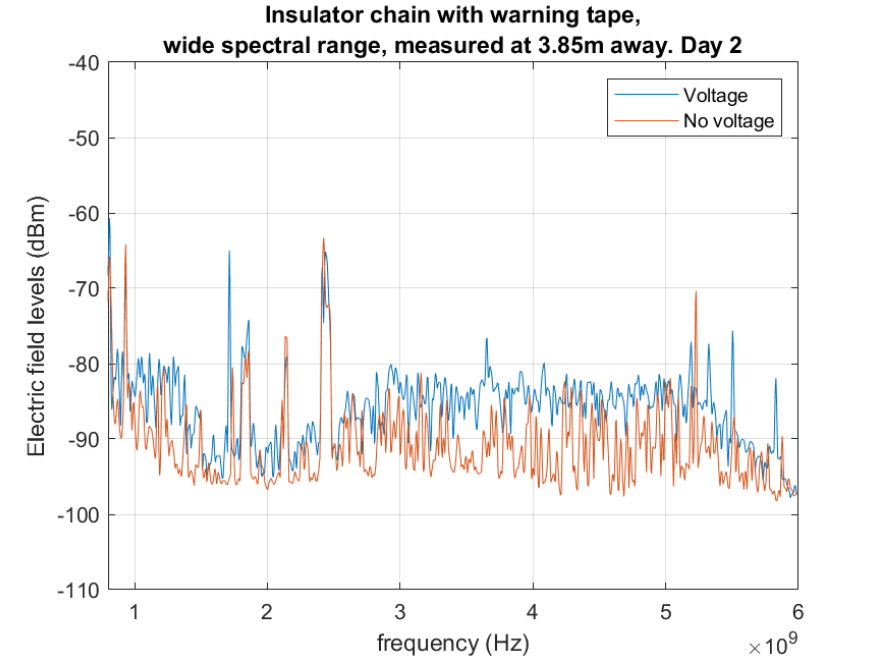

Figure 83: Electric field as a function of frequency. Bandwidth used when recording background levels and levels with the applied voltage was 10 kHz.

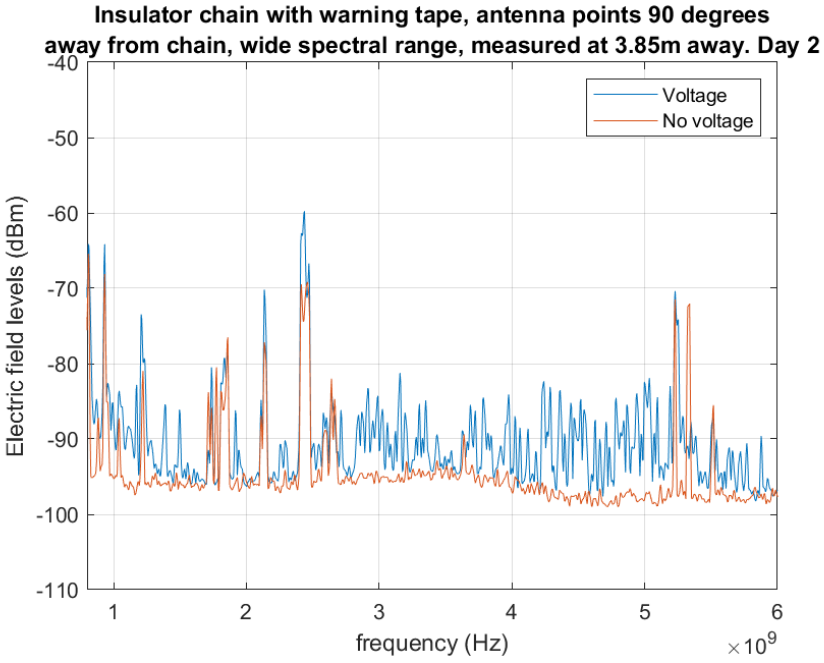

Figure 84: Electric field as a function of frequency. Bandwidth used when recording background levels and levels with the applied voltage was 10 kHz.

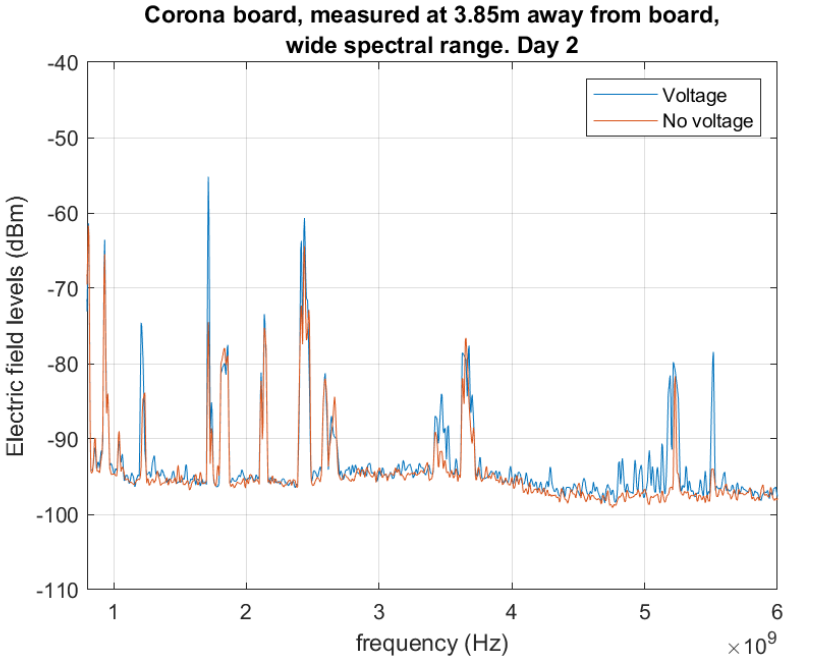

Figure 85: Electric field as a function of frequency. Bandwidth used when recording background levels and levels with the applied voltage was 10 kHz.

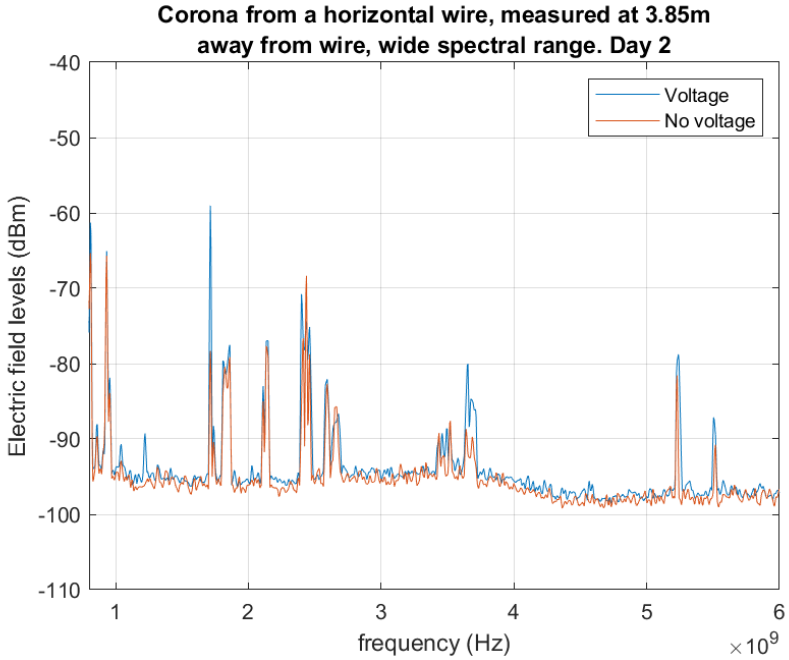

Figure 86: Electric field as a function of frequency. Bandwidth used when recording background levels and levels with the applied voltage was 10 kHz.

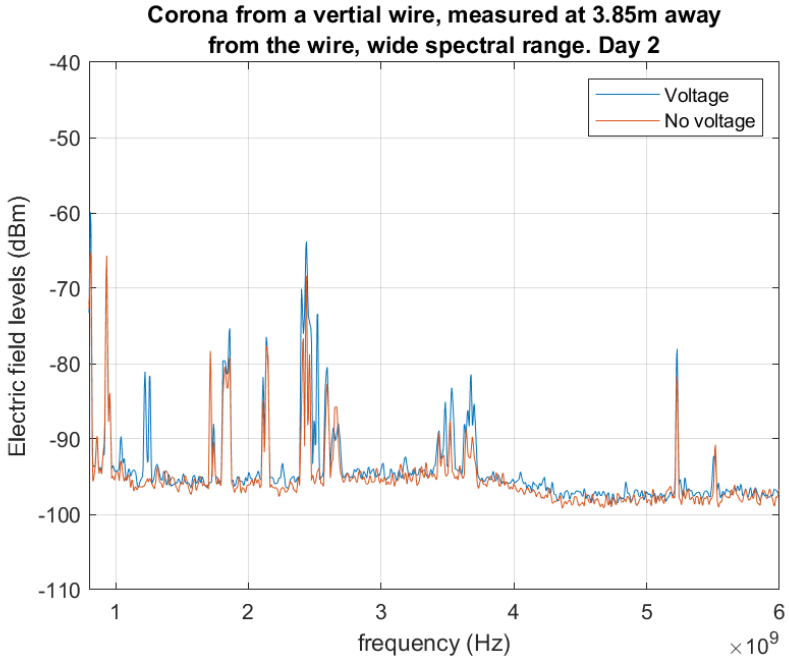

Figure 87: Electric field as a function of frequency. Bandwidth used when recording background levels and levels with the applied voltage was 10 kHz.

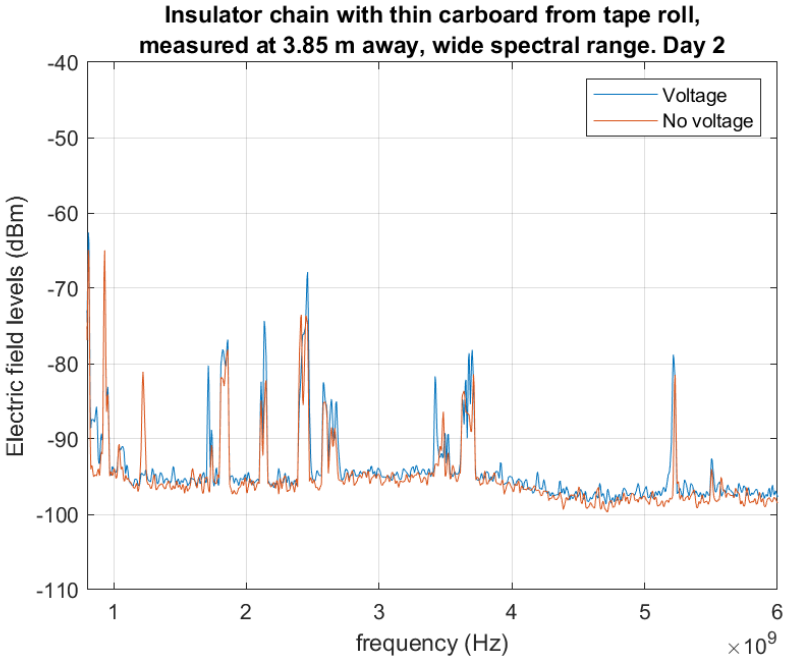

Figure 88: Electric field as a function of frequency. Bandwidth used when recording background levels and levels with the applied voltage was 10 kHz.

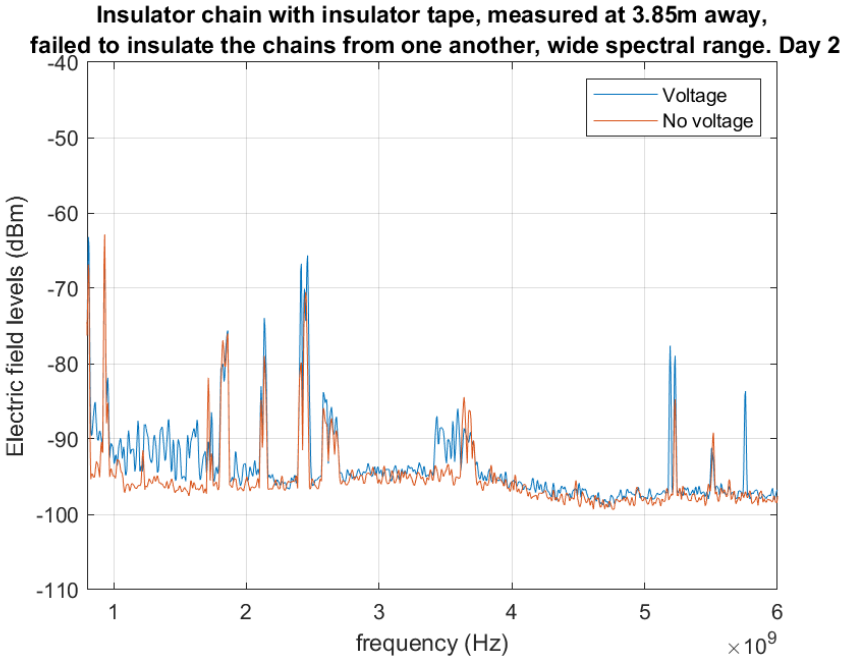

Figure 89: Electric field as a function of frequency. Bandwidth used when recording background levels and levels with the applied voltage was 10 kHz.

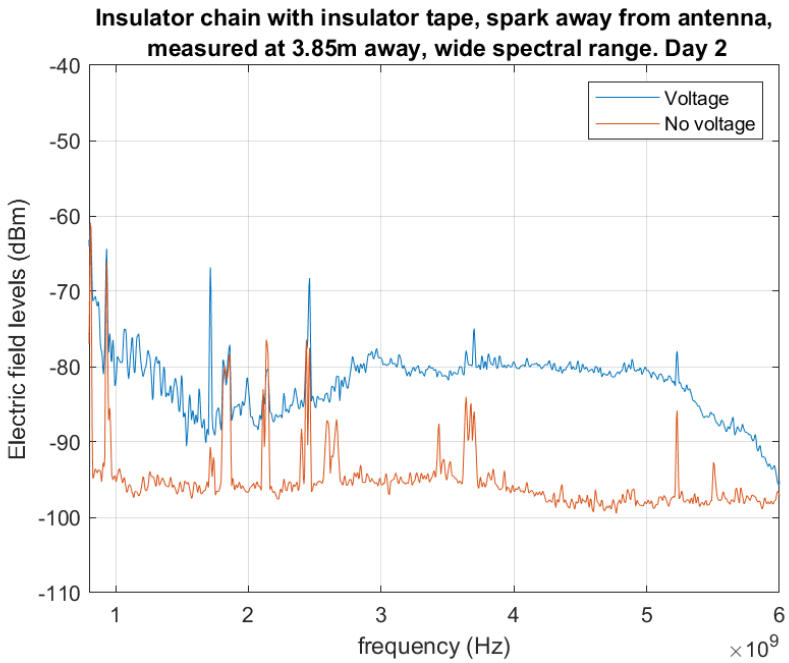

Figure 90: Electric field as a function of frequency. Bandwidth used when recording background levels and levels with the applied voltage was 10 kHz.

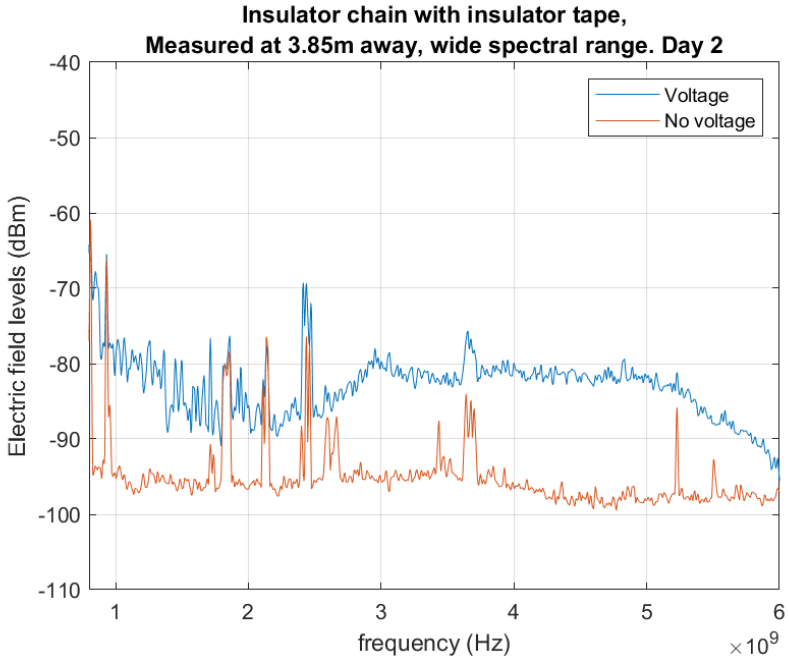

Figure 91: Electric field as a function of frequency. Bandwidth used when recording background levels and levels with the applied voltage was 10 kHz.

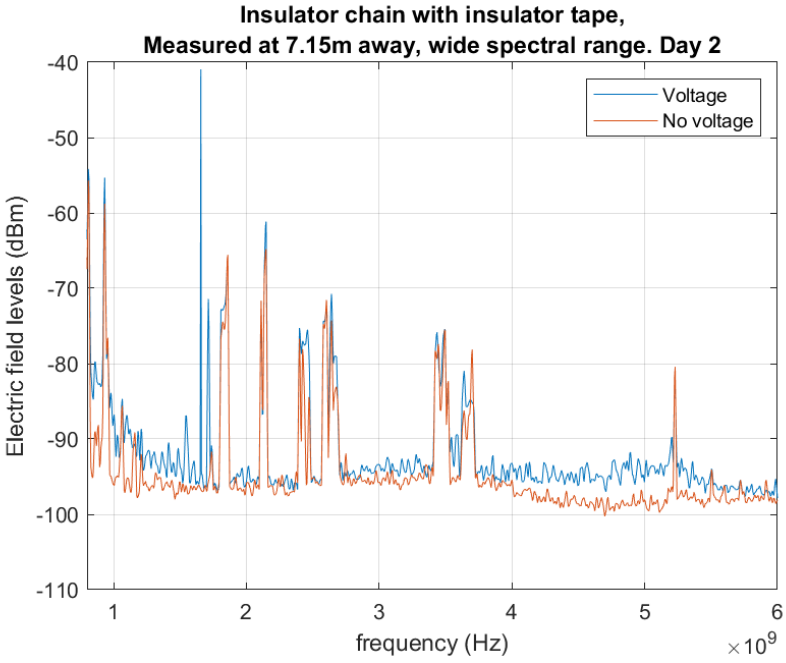

Figure 92: Electric field as a function of frequency. Bandwidth used when recording background levels and levels with the applied voltage was 10 kHz.

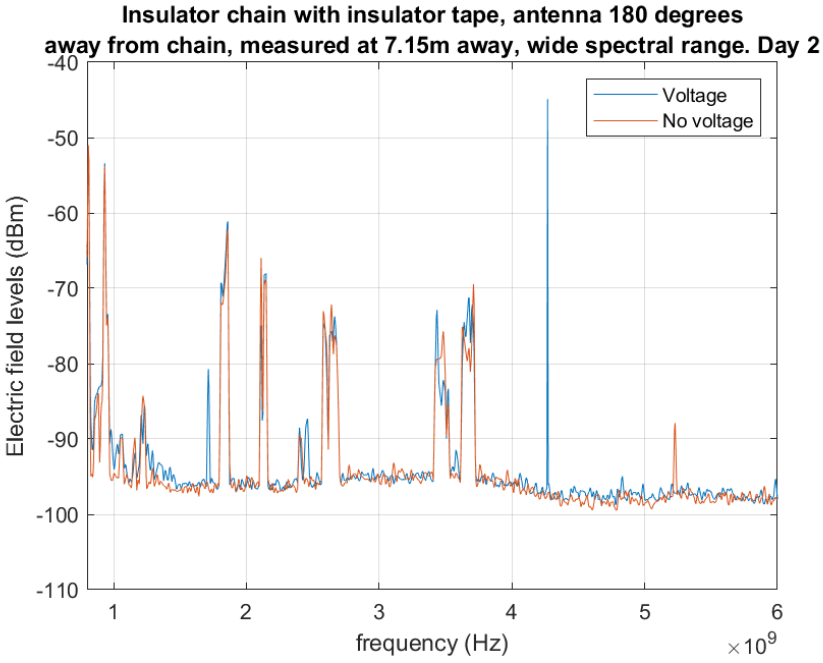

Figure 93: Electric field as a function of frequency. Bandwidth used when recording background levels and levels with the applied voltage was 10 kHz.

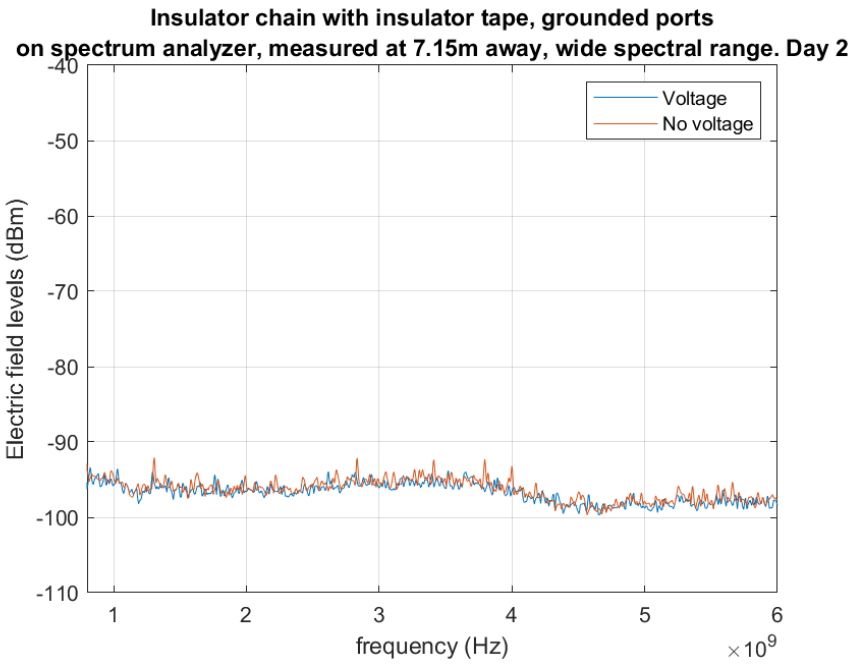

Figure 94: Electric field as a function of frequency. Bandwidth used when recording background levels and levels with the applied voltage was 10 kHz.

€€€€ FOR DIVA €€€€

{
"Author1": { "Last name": "Björklund",
"First name": "Johan Erik Magni",
"Local User Id": "u14vln3o",
"E-mail": "erbjorkl@kth.se",
"organisation": {"L1": "School of Electrical Engineering and Computer Science, KTH",
}
},
"Cycle": "2",
"Course code": "EA270X",
"Credits": "30.0",
"Degree1": {"Educational program": "
"
,"programcode": "TELPM"
,"Degree": "Masters programme in Electrical engineering"
},
"Title": {
"Main title": "Potential of interference to global-navigation systems from power-line discharges.",
"Subtitle": "A study based on laboratory measurements and plasma simulation.",
"Language": "eng" },
"Alternative title": {
"Main title": "Möjligheten för störningar av globala navigationssystem från kraftledningsurladdningar.",
"Subtitle": "En studie baserad på laborationsmätningar och plasmasimuleringar.",
"Language": "swe"
},
"Supervisor1": { "Last name": "Edin",
"First name": "Hans",
"Local User Id": "u100003",
"E-mail": "edin@kth.se",
"organisation": {"L1": "School of Electrical Engineering and Computer Science, KTH",
"L2": "Electrical Engineering" }
},
"Supervisor2": { "Last name": "Augustsson",
"First name": "Torsten",
"E-mail": "torsten.augustsson@svk.se",
"Other organisation": "Svenska kraftnät, Teknikspecialist, Jordning och EMF"
},
"Examiner1": { "Last name": "Taylor",
"First name": "Nathaniel",
"Local User Id": "u1d13i2c",
"E-mail": "taylor@kth.se",
"organisation": {"L1": "School of Electrical Engineering and Computer Science, KTH",
"L2": "Electrical engineering" }
},
"Cooperation": { "Partner_name": "Svenska kraftnät"},
"National Subject Categories": "202,202",
"Other information": {"Year": "2024", "Number of pages": "95"},
"Series": { "Title of series": "TRITA-EECS-EX" , "No. in series": "2022:00" },
"Opponents": { "Name": "S. Gopinath"},
"Presentation": { "Date": "2024-05-03 08:50"
,"Language":"eng"
,"Room": "via Zoom https:https://kth-se.zoom.us/my/hansedinzoomroom"
,"Address": "Teknikringen 31, floor 4, room 1424"
,"City": "Stockholm" },
"Number of lang instances": "2",
"Abstract[eng]": €€€€

```
\newpage
\section*{Abstract}
\input{textFolder/abstractEnglish}
\newpage
```

€€€,
"Keywords[eng]": €€€€
EMC, Electromagnetic Interferences, Charges, Discharges, Power Lines, Insulator bells, GPS, Drone, Radiation.
€€€,
"Abstract[swe]": €€€€

```
\input{textFolder/abstractSvenska}
```

€€€,
"Keywords[swe]": €€€€
EMC, Electromagnetiska Störningar, Laddningar, Urladdningar, Kraftledningar, Isolatorklockor GPS, Drönare, Utstrålning.
€€€,
}